THE ELECTROLUMINESCENCE AND SCANNING TUNNELING MICROSCOPY OF SINGLE MOLECULES

by

John William Buker
M. Sc, Simon Fraser University 2003

THESIS SUBMITTED IN PARTIAL FULFILLMENT
OF THE REQUIREMENTS FOR THE DEGREE OF
DOCTOR OF PHILOSOPHY
IN THE DEPARTMENT
OF
PHYSICS

SIMON FRASER UNIVERSITY
Spring 2009

APPROVAL

Name:	John William Buker
Degree:	Doctor of Philosophy
Title of Thesis:	The electroluminescence and scanning tunneling microscopy of single molecules
Examining Committee:	Dr. J. Steven Dodge (Chair)
	Dr. George Kirczenow (Senior Supervisor)
	Dr. Brad Johnson, Professor Department of Physics, Western Washington University
	Dr. Karen Kavanagh, Professor, SFU
	Dr. Eldon Emberly (Internal Examiner) Assistant Professor, SFU
	Dr. Sergio Ulloa (External Examiner) Professor, Department of Physics and Astronomy, Ohio University
Date Approved:	March 3, 2009

SIMON FRASER UNIVERSITY
LIBRARY

Declaration of Partial Copyright Licence

The author, whose copyright is declared on the title page of this work, has granted to Simon Fraser University the right to lend this thesis, project or extended essay to users of the Simon Fraser University Library, and to make partial or single copies only for such users or in response to a request from the library of any other university, or other educational institution, on its own behalf or for one of its users.

The author has further granted permission to Simon Fraser University to keep or make a digital copy for use in its circulating collection (currently available to the public at the "Institutional Repository" link of the SFU Library website <www.lib.sfu.ca> at: <http://ir.lib.sfu.ca/handle/1892/112>) and, without changing the content, to translate the thesis/project or extended essays, if technically possible, to any medium or format for the purpose of preservation of the digital work.

The author has further agreed that permission for multiple copying of this work for scholarly purposes may be granted by either the author or the Dean of Graduate Studies.

It is understood that copying or publication of this work for financial gain shall not be allowed without the author's written permission.

Permission for public performance, or limited permission for private scholarly use, of any multimedia materials forming part of this work, may have been granted by the author. This information may be found on the separately catalogued multimedia material and in the signed Partial Copyright Licence.

While licensing SFU to permit the above uses, the author retains copyright in the thesis, project or extended essays, including the right to change the work for subsequent purposes, including editing and publishing the work in whole or in part, and licensing other parties, as the author may desire.

The original Partial Copyright Licence attesting to these terms, and signed by this author, may be found in the original bound copy of this work, retained in the Simon Fraser University Archive.

Simon Fraser University Library
Burnaby, BC, Canada

Last revision: Spring 09

Abstract

The scanning tunneling microscopy (STM) of single molecules has become a prominent experimental method in the field of molecular electronics. It has been found that in STM experiments, when an electric current flows through a single molecule, the molecule may luminesce. This electroluminescence, in conjunction with traditional STM data, provides a potentially important additional degree of freedom for understanding nanoscale systems. This thesis describes exploratory theoretical work on the newly emerging phenomenon of molecular electroluminescence, and its relationship to the scanning tunneling microscopy of single molecules. A local electrode framework is progressively developed, in order to explain single-molecule electroluminescence data as well as simulating STM current-voltage characteristics and topographic maps for molecules on complex substrates. The molecule Zn(II)-etioporphyrin I is chosen for detailed analysis and comparison with experiment. Electron transport is studied using Landauer theory that relates electric current to the transmission probability for an electron to scatter through the molecule. The theoretical approach utilizes tight binding and extended Hückel approaches for the electrodes and molecule, a charge-conserving scheme to self-consistently model the influence of electric fields and electric currents on the molecular energy level structure, and Fermi's golden rule in calculating electroluminescence. A single coherent framework is ultimately achieved that explains for the first time both the electric current data and molecular electroluminescence in a molecular system and elucidates the physics underlying a rich and previously puzzling array of interlinked optical and transport phenomena.

To Elliott and Finnegann Jack, who I am sure will enjoy this book immensely. And of course to Malkovitch.

Acknowledgments

I would like to thank, first and foremost, my supervisor George Kirczenow, for all of the help and insights he provided in the eight years he was my supervisor, for his patience and attitude, his physics intuition, his sense of humour and his wisdom.

I also thank Brad Johnson and Ross Hill for their time on my supervisory committee all these years, and for always being able to offer me fresh ideas and insights for my work. Also, thank you to Karen Kavanagh for being willing to step into my committee on short notice.

Thank you also to all the office staff who helped me through the years with my questions, my deadlines, room bookings, and with the office equipment, for being cheerful, helpful and kind.

Thank you to my family and my friends... for indulging me in this "physics habit" of mine.

Finally, I thank Hilde Bootstrap-Festerling, for providing me with smiles, cats, and the best food in the world, as I worked to complete this thesis.

Contents

List of Tables

List of Figures

Chapter 1

Introduction

In these early years of the 21st century, we find ourselves able to explore deeper and deeper into our world, a quantum mechanical world that is not at all what it seems at our intuitive human length scales.

We may now probe length scales tens or hundreds of thousands of times smaller than the thickness of a human hair. When we do this, we do not literally "see" what is happening. At such a small length scale (the nanoscale), the wave-particle duality of quantum mechanics is paramount, and we must think of matter and light in terms of amplitudes in order to understand what is happening. Instead of simply observing a system under intense magnification, we must use our knowledge of quantum physics to perform and interpret experiments of the nanoscale.

The scanning tunneling microscope (STM) is one of the primary tools that has been developed in the last 30 years for this purpose. Operating under the principle of electron tunneling, the STM provides a measure of the local density of states (LDOS) for the system: A bias voltage is applied between the STM tip and sample, and electrons tunnel from the tip to available states in the sample (or from sample to tip at reversed bias). As the bias voltage is increased, new electronic states become available for transmission. The electric current at a given bias is measured for a certain position of the STM tip above the sample. The tip can then be moved laterally across the sample, as well as vertically. In this way, an electric current map of the surface, or a topographic map at a constant current, may be constructed. This map is related to the geometrical structure of the sample surface, but not in the direct visual way as we are accustomed to when we view things with our eyes or with optical microscopes. Interpreting the physics of these systems, where we have limited knowledge, is a vital, challenging issue in the field of theoretical nanophysics.

Experimentally, the STM has undergone a transformation from use mainly as a passive instrument measuring the LDOS of a sample, into an active component of experimental systems. One example of this is its use as one of the electrodes for a molecular wire: A molecular wire is a single molecule (or a few molecules) that forms an electrically conducting bridge between a pair of metallic electrodes. When an STM tip is placed above a single molecule on a metallic substrate, it acts as one of these electrodes, and the substrate as the other. The behaviour of the molecular wire is largely dependent on the interaction of the molecule with the electrodes. In the last 15 years, these types of STM experiments have flourished in the laboratory.

Theories of varying degrees of complexity have been used in order to try to understand the results of these experiments. While there has been significant success, there is a fundamental issue theorists are constantly coming up against when attempting to interpret experimental results. Since on the nanoscale we can not directly see our experimental systems, the detailed structure and composition of a system is often unknown. Hence, if theory does not agree with experiment, the theory may not be adequate, or it may be adequate but with improper assumptions for the experimental system. Similarly, if a theoretical result is in agreement with an experimental result, there is often still a question of whether the theoretical result is valid, or whether the theory is incorrect but includes assumptions for the system that have lead to a result that agrees with experiment.

Part of the solution to these issues is to do experiments to better determine the structure and composition of the system. In this way, we may more definitively determine which theoretical approaches are best able to describe the experimental system. Another necessity is to compare a whole range of different kinds of experimental data with theoretical calculations, as well as using the predictive power of theory, thereby determining which theoretical approaches and assumptions better describe and predict experimental results. However, until recently, for the STM study of systems of single molecules on substrates there have been few degrees of freedom for experimental and theoretical comparison: Scanning tunneling microscopy mainly involves studying current-voltage (I-V) characteristics and STM-generated topographic images of molecules. While much insight into the electronic properties of these systems has been obtained by directly studying electric current in these ways, the lack of additional degrees of freedom makes definitive theoretical and experimental comparisons very difficult.

Recently, however, a new phenomenon occurring in STM/molecule/substrate systems has been discovered. It has been observed that when an electric current flows between an STM tip and substrate through a single molecule, the molecular wire may give off light (photons) in the process.[1, 2, 3, 4, 5, 6] By studying the nature of this molecular electroluminescence, in parallel with more traditional STM I-V characteristics and topographic images, a crucial degree of freedom may be gained for theoretical and experimental comparison. As well, this area of study may help advance nanophysics toward an emerging field of single-molecule photonics.

The unique aspect of single-molecule electroluminescence is that it is fundamentally *molecular-based*, in contrast to the more well-understood phenomenon of plasmon-mediated photon emission: Plasmon-mediated emission occurs due to the decay of collective electron oscillations in the STM tip or the substrate surface (or both), called plasmons. It is seen in STM systems above bare metallic substrates,[7, 8] and may be amplified or weakened by the presence of molecules in the tip/substrate junction. Enhanced photon emission has been observed in STM tip/molecule/substrate experiments since the early 1990s, but it was unclear until recently whether the emission observed was limited to an amplification of the plasmon-based emission observed on bare metallic surfaces,[9, 10] or whether there was an intrinsically molecular-based photon emission mechanism at work. Recently, it has been definitively demonstrated that electric current flow through a molecule may indeed cause the molecule to luminesce, due to molecular orbital electronic transitions; that the photon emission process is not limited to the decay of plasmons.[11, 12]

Single-molecule electroluminescence is a new experimental phenomenon that has undergone an extremely small amount of theoretical investigation. The first theoretical study[13] (Buker and Kirczenow, 2002), predicted molecular electroluminescence to occur in cases where the tip-molecule and molecule-substrate couplings are reasonably symmetric in strength. Since then, it has been found experimentally that a thin insulating layer separating the molecule from the substrate (in order to reduce the molecule-substrate coupling), is usually necessary in order to successfully observe electroluminescence.[11, 12] A prime example of this condition was found in the STM study of the Zn-etioporphyrin molecule on a NiAl(110) substrate.[11] The molecule did not luminesce on the bare NiAl(110) surface, but if the surface was oxidized and formed a monolayer (a layer with a thickness of only one molecule) of aluminum oxide (Al_2O_3) on which Zn-etioporphyrin molecules were placed, photon emission was found to sometimes occur.

Theoretically, this system is extremely difficult to precisely model. The monolayer of Al_2O_3 has a large, complex unit cell and is non-commensurate with the underlying NiAl(110) lattice. The geometry of the molecule/substrate junction is unknown. This is a classic example of the fundamental issue theorists encounter when studying nanoscale systems: not understanding the atomic-scale details of the system, thus preventing sophisticated theoretical models from being developed.

In this system, however, there is a new degree of freedom for theoretical and experimental comparison: photon emission data. In the experiments, the observation of single-molecule electroluminescence was dependent on the location of the molecule on the surface. Some locations yielded electroluminescence, and some did not. Photon emission results were presented in conjunction with more traditional STM measurements (I-V characteristics and topographic images). Results from all three types of data depended on the location of the molecule above the substrate. This has opened up the intriguing possibility of investigating this system with little *a priori* understanding of the geometry of the molecule/substrate junction.

With no previous theoretical work modelling this type of experiment, and theories of single-molecule electroluminescence in their very infancy, this thesis aims to provide a new framework for studying such systems, investigating on the same theoretical level both the scanning tunneling microscopy and the electroluminescence of single molecules. A primary focus of the thesis is the development of a *local-electrode approach* for understanding single molecule STM and electroluminescence data, useful for cases today where there is a thin insulating layer with a complex atomic structure separating the molecule from the substrate, as well as for possible future cases where there may be multiple well-defined local electrodes to the molecule.

In Chapter 2, the experimental and theoretical background is presented. The chapter touches on some of the early experimental work that provided the initial motivation for the topic of this thesis. In addition, a simple model for single-molecule electroluminescence, that formed the basis of my M.Sc. thesis, is presented. Scattering theory is briefly reviewed, and the *minimal charging approximation*, used for a real system later in this thesis (Chapters

5-6), is introduced.

Chapters 3 and 4 focus on an investigation of single-molecule scanning tunneling microscopy. In Chapter 3, aspects of the simple model of the previous chapter are built upon in creating a model STM system. The model uses a *local electrode approach* to calculate current flow through the molecule, treating the STM tip-molecule coupling and the molecule-substrate coupling on the same theoretical footing, both as *local* electrodes coupled to the molecule. With this model, STM current maps may be constructed for comparison with experiment. Chapter 4 uses the model described in Chapter 3 to investigate the scanning tunneling microscopy of a real molecule - Zn-etioporphyrin. The geometric and electronic structure of the molecule is determined, and various different current maps are constructed for different possible couplings of the molecule with the substrate and energy level alignments. These maps are compared with experiment, and through this comparison we gain information about the experimental system, including the nature of the coupling of the molecule to the substrate.

Chapters 5 and 6 focus on the investigation of single-molecule electroluminescence. Using the techniques and conclusions of all of the previous chapters, these two chapters bring together into a single model the theoretical investigation of conventional STM I-V characteristics and electroluminescence data. Chapter 5 is a presentation of the general model approach that is implemented. Here, a more sophisticated version of the *minimal charging approximation* that is presented in Chapter 2 is implemented. Expanding on the technique presented in Chapter 3, multiple local electrodes are used in order to model STM I-V characteristics and photon emission. The thesis culminates in Chapter 6, with the implementation of this model for the Zn-etioporphyrin molecule. Various subtle challenges are worked through, and results using three classes of molecule-substrate couplings are compared with experimental data. Many experimental results that were previously not understood are explained. The success of the model in explaining *both* conventional STM data as well as electroluminescence data should serve as a benchmark for the development of more sophisticated theories. As well, it should help in the achievement of a better understanding of single-molecule electroluminescence, and more generally contribute to the development of the emerging field of single-molecule photonics.

The thesis is concluded by summarizing the important findings, and possible directions for future research in this area.

Chapter 2

Background

2.1 Experimental motivation

Since the 1990s, there have been experiments conducted on molecular monolayers, using a scanning tunneling microscope, that have hinted at the possibility of molecular electroluminescence.

By attaching a photon detector to the standard STM apparatus, photon emission from the system, in addition to electric current, may be detected as a function of bias voltage or tip position. Early experiments detected photon emission from bare metal[7, 8] or semiconducting[14, 15] surfaces, and theories explained this emission to be related to the decay of tip-surface plasmons[8, 16].

In later experiments, molecules were placed inside the tip-surface junction, and in various cases enhanced photon emission was observed[1, 2, 3, 4, 5, 6]. One of the early examples of this is seen in Figure 2.1. In this experiment, an STM tip scans across a monolayer of C_{60} fullerenes (buckyballs) on an Au(110) surface. Photons were detected with a lens and photomultiplier. Intense emission is observed when the STM tip is placed above an individual C_{60} molecule. Fig. 2.1 illustrates the potential of scanning tunneling microscopy to use photon emission properties of a system to gain extreme precision.

Another elegant example of molecule-dependent photon emission involves reduced and oxidized alkanethiol monolayers adsorbed on Au(111)[4]. In experiments by Poirier, a monolayer of reduced decanethiol is adsorbed on a Au(111) surface, after which the thiolate monolayer is partially oxidized, to form a mix of reduced and oxidized decanethiol.

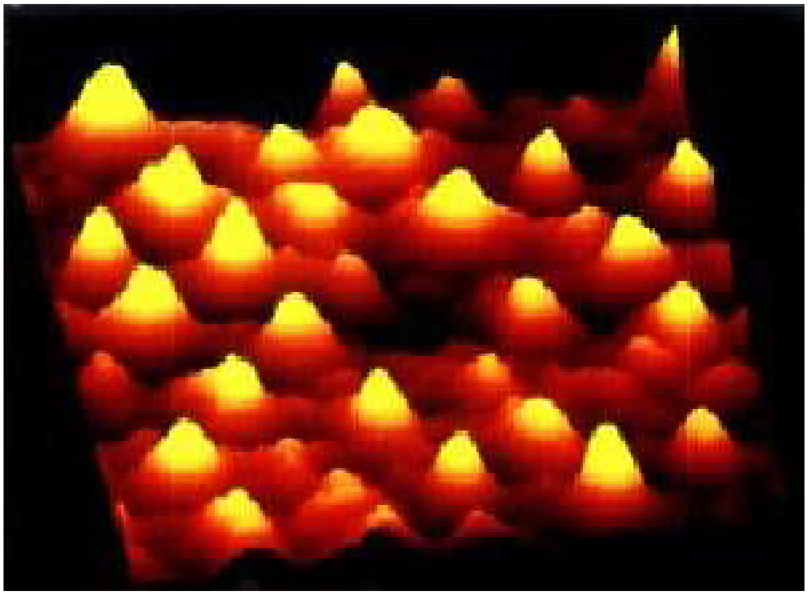

Figure 2.1: Photon intensity map of a C_{60} monolayer on an Au(110) surface. Individual molecules separated by about 10 Å are clearly resolved. Photon emission intensity is peaked when the STM tip is above a C_{60} molecule. (Reproduced from Ref. [17] with permission from the author.)

An STM constant-current topograph of the sample is generated, as well as a photon map, which measures the photon emission on the same region of the surface as the topograph. Comparing the photon map with the topograph, one notices that the reduced regions have about 35% greater photon emission than the oxidized regions (see Fig.2.2).

These and a few other similar experiments gave me the initial motivation for a theoretical investigation of single molecule electroluminescence. At the time (2001) there were only a small number of STM experiments providing evidence for this phenomenon, and it was an open question whether photon emission was always limited to an amplification of plasmon-mediated photon emission,[9, 10] or whether in some cases there could be an inherently molecular-based mechanism for photon emission.

In the years since, it has been definitively demonstrated through STM experiments that electric current flow through a molecule may indeed cause the molecule to luminsece[11, 12] due to molecular orbital electronic transitions. The experiments by Qiu, Nazin and Ho[11] yielded a particularly intriguing and rich set of results. In these experiments, single

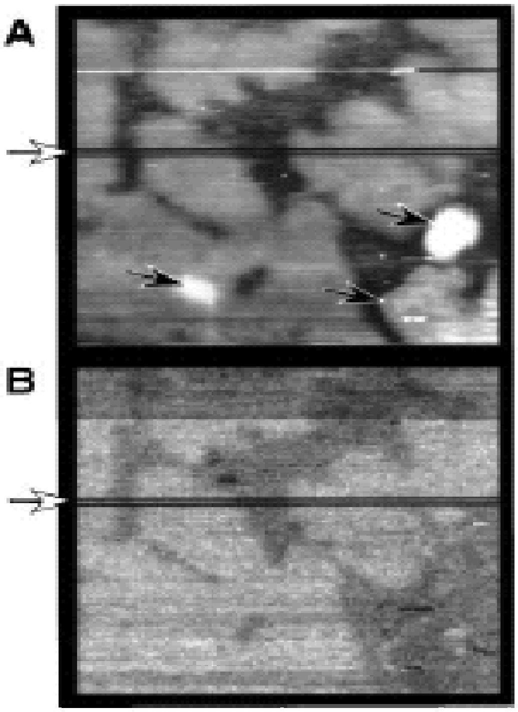

Figure 2.2: Simultaneously acquired STM topograph and photon map of a partially oxidized alkanethiol ($CH_3(CH_2)_9SH$) monolayer on Au(111). Maps are 1000 by 1000Å. (A) Constant current topograph. The light regions are reduced; the dark regions are oxidized. (B) Corresponding photon map. Light regions represent greater photon emission. Notice the similarities in the two pictures. Reduced regions produce about 35% greater photon emission than oxidized regions. (Reproduced from Ref. [4] with permission from the author.)

Zn-etioporphyrin molecules were studied with an STM, on a NiAl(110) surface that had been oxidized to form a 5 Å thick film of Al_2O_3 separating each molecule from the substrate. Fig. 2.3 shows a sample of interesting results. Depending on where the molecule is placed above the substrate, different STM topographs are produced and the molecule may or may not be found to luminesce. These experiments are discussed in detail in Chapters 4 and 6.

The experiments listed above have provided a continuing motivation for investigation into the electroluminescence and scanning tunneling microscopy of single molecules, and

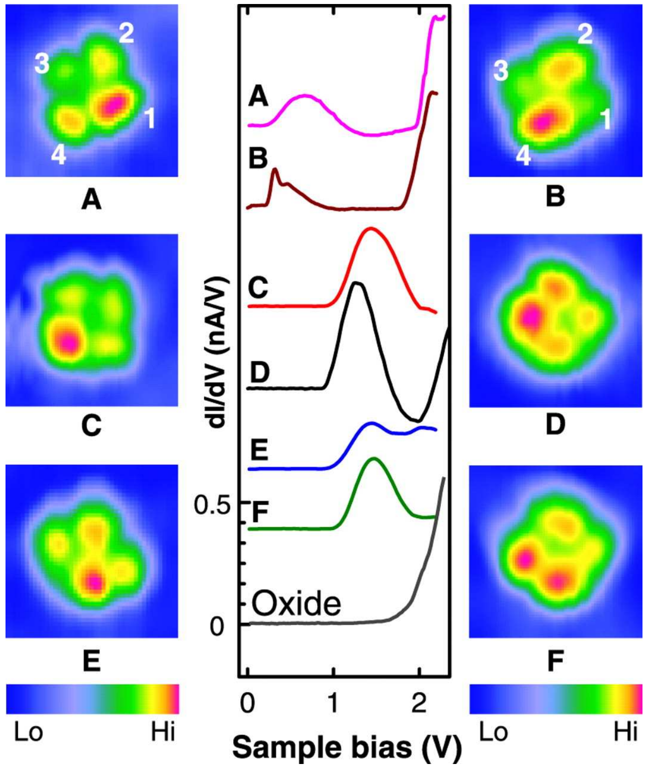

Figure 2.3: From Qiu *et al.*. (Ref. [11]). Reprinted with permission from AAAS. STM topographs and dI/dV curves for Zn-etioporphyrin/Al_2O_3/NiAl(110), for molecules at different locations on the substrate. (A-F) Topographs and dI/dV curves representative of the various molecular images observed. Topographs are 32 by 32Å. Case B was most commonly observed (30% of the time). Molecular electroluminescence was observed for cases A and B but not for C-F.

how the two phenomena are related and connected.

2.2 Modelling a simple molecular wire

A starting point for understanding single molecule electroluminescence lies in studying electron transport and photon emission from a simple molecular wire, work that in 2003 formed the basis of my Master's Thesis. The rest of this chapter contains a necessary presentation of this work, that this Doctoral Thesis greatly builds upon in following chapters.

In order to model electron transport through a molecular wire in a simple way, a methodology using Landauer theory for evaluating electronic current is presented. Landauer theory relates electronic current to the scattering of single electrons.[18, 19] For a one-dimensional wire connecting two reservoirs of electrons, the conductance at infinitesmal bias is related to the transmission probability for an electron to scatter from one reservoir to the other. The relation is

$$G = \frac{2e^2}{h} T(E_F) \tag{2.1}$$

where E_F is the Fermi energy of the reservoirs. Generalizing to finite bias V and finite temperature T, the following formula for current is obtained:

$$I(V) = \frac{2e}{h} \int_{-\infty}^{\infty} dE T(E,V) \left(\frac{1}{e^{(E-\mu_S)/kT} + 1} - \frac{1}{e^{(E-\mu_D)/kT} + 1} \right) \tag{2.2}$$

where $\mu_S = E_F + eV/2$ and $\mu_D = E_F - eV/2$ are the electro-chemical potentials of the source reservoir and drain reservoir respectively. The distribution of electrons incident from the source and drain reservoirs at finite temperature is given by the Fermi functions that appear in the above formula. For $T = 0$ K, this formula reduces to

$$I(V) = \frac{2e}{h} \int_{\mu_D}^{\mu_S} dE T(E,V) \tag{2.3}$$

Thus, if electron transmission probabilities for a molecular wire are known, Landauer theory can be utilized to calculate the electric current through the molecular wire.

For a simple molecular wire system, the transmission probability for an electron may be calculated using the generic model now presented. The ultimate purpose of this exercise is to develop a basic qualitative picture of the underlying *photon emission* mechanism, upon which to build.

Each metal electrode is modeled as a one-dimensional tight-binding chain. The molecular wire is modeled in the simplest possible way: as a pair of atoms placed next to the origin, forming a bridge between the two electrodes (see Fig. 2.4). The model Hamiltonian of this system may be thought of as having three parts: the source and drain electrodes, the molecule, and the interaction between the electrodes and the molecule. These parts may

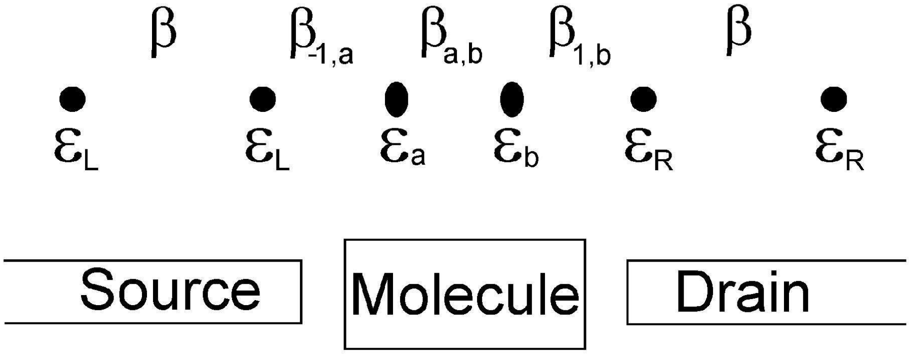

Figure 2.4: A schematic diagram of a simple molecular wire. The source and drain electrodes are semi-infinite. The two atoms in the center represent the molecule.

be written as $H = H_{\text{electrodes}} + H_{\text{molecule}} + W$, where W is the interaction term. To capture the physics in a simple way, in this model each atom of the source and drain electrodes is represented as a site consisting of one valence electronic orbital. The Hamiltonian for the source and drain electrodes may be written as

$$\begin{aligned} H_{\text{electrodes}} = &\sum_{n=-\infty}^{-1} \varepsilon_L |n\rangle\langle n| + \beta(|n\rangle\langle n-1| + |n-1\rangle\langle n|) \\ &+ \sum_{n=1}^{\infty} \varepsilon_R |n\rangle\langle n| + \beta(|n\rangle\langle n+1| + |n+1\rangle\langle n|), \end{aligned} \tag{2.4}$$

where ε_L and ε_R are the site energies of the source and drain electrodes, β is the hopping amplitude between nearest neighbour electrode atoms, and $|n\rangle$ represents the valence orbital at site n of one of the electrodes. The Hamiltonian for the molecule may be written in terms of its atomic basis as well:

$$H_{\text{molecule}} = \varepsilon_a |a\rangle\langle a| + \varepsilon_b |b\rangle\langle b| + \beta_{a,b}(|a\rangle\langle b| + |b\rangle\langle a|), \tag{2.5}$$

where ε_a and ε_b are the site energies of atoms a and b of the molecule, and $\beta_{a,b}$ is the hopping amplitude between the atomic orbitals $|a\rangle$ and $|b\rangle$ of the molecule. The site energies ε_a and ε_b of the molecule are affected when a bias is applied. This effect is important and is discussed in Sec. 2.4. The Hamiltonian for the interaction W between the electrodes and the molecule is

$$W = \beta_{-1,a}(|-1\rangle\langle a| + |a\rangle\langle -1|) + \beta_{1,b}(|1\rangle\langle b| + |b\rangle\langle 1|), \tag{2.6}$$

where $\beta_{-1,a}$ and $\beta_{1,b}$ are the hopping amlitudes between atom a of the molecule and the source electrode, and between atom b and the drain electrode, respectively. In this simple first model, all of the orbitals of the different atoms are considered to be orthogonal. In Chapters 3-6, this model will be extended to include nonorthogonality of atomic orbitals in the molecule and of electrode orbitals coupled to the molecule.

When a bias is applied, the site energies ε_L and ε_R of the electrodes are affected such that $\varepsilon_L = \varepsilon_{\text{electrodes}} + eV_{\text{bias}}/2$ and $\varepsilon_R = \varepsilon_{\text{electrodes}} - eV_{\text{bias}}/2$, where $\varepsilon_{\text{electrodes}}$ is the common zero-bias Fermi energy.

Since the molecule is attached to semi-infinite electrodes with periodic potentials, electrons exist in the electrodes in the form of Bloch waves, and undergo reflection or transmission when they encounter the two-atom molecule. Their wave functions are of the form

$$|\psi\rangle = \sum_{n<0}(e^{iknd} + re^{-iknd})|n\rangle + \sum_{n>0} te^{ik'nd}|n\rangle + c_a|a\rangle + c_b|b\rangle, \tag{2.7}$$

where d is the lattice spacing, and t and r are the transmission and reflection coefficients. By performing the simple calculation $\langle n|H|\psi\rangle = E\langle n|\psi\rangle$, a simple expression for the electron energy band may be obtained: $E = \varepsilon_i + 2\beta cos(kd)$. This equation holds for both $\varepsilon_i = \varepsilon_L$ and $\varepsilon_i = \varepsilon_R$, so when an electron with initial wave vector k undergoes transmission, its wave vector changes (to k') due to the difference between ε_L and ε_R. Similarly, by applying $\langle -1|$, $\langle a|$, $\langle b|$, and $\langle 1|$ to $H|\psi\rangle$, expressions for the transmission and reflection coefficients t and r may be obtained,[13] as well as expressions for the coefficents c_a and c_b, representing the amplitude for the electron on the molecule. The transmission probability is given by

$$T = |t|^2 \frac{v(k')}{v(k)} = |t|^2 \frac{sin(k'd)}{sin(kd)} \tag{2.8}$$

where $v(k)$ is the velocity of an electron at wave vector k. Once we know t for the relevant electron energies, the total electric current in the molecular wire may be calculated using

Eq. 2.3. (The temperature is assumed to be 0 K.)

2.3 Photon emission from a molecular wire

To calculate photon emission from a molecular wire, we may use the expression for the spontaneous emission rate of a system emitting photons into empty space,[20] derived using Fermi's Golden Rule. The emission rate is given by

$$\frac{4e^2\omega^3}{3\hbar c^3}|\langle\psi_f|\mathbf{x}|\psi_i\rangle|^2, \tag{2.9}$$

where ψ_i and ψ_f represent initial and final states, and $\hbar\omega$ is their difference in energy. *In this thesis, the words $state$ and $wave function$ are considered to be interchangable.*

For the case of the simple two-atom molecular wire that is considered in this chapter, with photon emission only considered from the molecular sites a and b, the emission rate is calculated to be approximately

$$R = \frac{4e^2\omega^3}{3\hbar c^3}|c^*_{a,f}c_{a,i}\langle a|\mathbf{x}|a\rangle + c^*_{b,f}c_{b,i}\langle b|\mathbf{x}|b\rangle|^2, \tag{2.10}$$

where i and f label initial and final states. The overlap terms $\langle a|\mathbf{x}|b\rangle$ and $\langle b|\mathbf{x}|a\rangle$ are neglected since they should be small compared to $\langle a|\mathbf{x}|a\rangle$ and $\langle b|\mathbf{x}|b\rangle$. Approximating $\langle a|\mathbf{x}|a\rangle$ and $\langle b|\mathbf{x}|b\rangle$ by the locations of their atomic centers, $\langle a|\mathbf{x}|a\rangle = -b/2$ and $\langle b|\mathbf{x}|b\rangle = b/2$ (b being the molecular bond length). Thus, in this system the rate for an electron in initial state i to undergo a transition to a final state f, lower in energy by $\hbar\omega$, and emit a photon is given by

$$R(k_i,\omega) = \frac{e^2\omega^3 b^2}{3\hbar c^3}|c^*_{b,f}c_{b,i} - c^*_{a,f}c_{a,i}|^2. \tag{2.11}$$

To calculate the emission rate as a function of photon energy, all electron states of the system, incoming from both the source and drain electrodes, must be considered. Since the temperature is assumed to be $0K$, all states up to the electrochemical potential of the appropriate electrode are occupied. ψ_f must be initially unoccupied, and it must be of lower energy than ψ_i. Therefore, it is appropriate to consider transitions from occupied initial states that are *incoming from the source,* to final states *within the electrochemical potential*

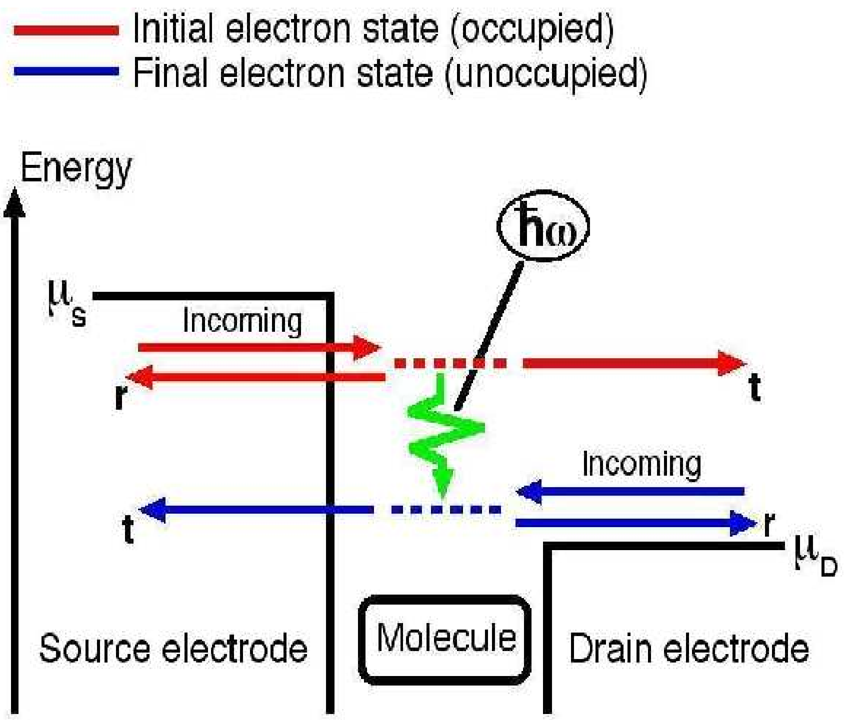

Figure 2.5: A schematic energy level diagram of a molecular wire transition.

window that are incoming from the drain, as shown in Fig. 2.5. This is an important but subtle point: The coefficients expressed in Eq. 2.11 are amplitudes for the molecular part of the *delocalized electron state* (wave function) expressed in Eq. 2.7. Thus, when a final (delocalized) state for a transition is considered, for it to be an unoccupied state it must be a state incoming from the drain electrode, that is above the electrochemical potential of the drain electrode.

After normalizing the wave functions and converting the sum over k states (and spin) into an integral over energy, an expression for the photon emission spectrum (for a given bias voltage) is obtained:

$$f(\omega) = \frac{1}{2\pi} \int_{\mu_D + \hbar\omega}^{\mu_S} \frac{R(k_i, \omega)}{-\beta sin(k_i d)} dE_i. \tag{2.12}$$

2.4 Minimal charging approximation

As a bias is applied to a molecular wire system, the energies of the molecular orbitals will be affected. For instance, whenever the electrochemical potential of one of the electrodes of a molecular wire crosses a molecular orbital energy level as a result of an applied bias, a new channel for electron transmission through the molecule is created. This may result in a change in the total charge of the molecule. This change in the molecular charge affects the electrostatic component of the energy of each of the orbitals, causing the energy levels to shift such that the actual charging that takes place is severely limited.[21]

For the model presented in this section, the shift of the molecular orbital energy levels in response to the applied bias is approximated by adjusting ε_a and ε_b equally *so as to maintain the net charge that the molecule has at zero bias.* This approximation of the molecular levels with bias is physically reasonable and remarkably similar to that obtained from *ab initio* calculations for some molecular wire systems.[22]

To calculate the total molecular charge, all of the eigenstates of the system, given by Eq. 2.7, are projected onto the bonding (O) and antibonding ($O*$) orbitals of the isolated molecule. Once the total charge is determined, the parameters ε_a and ε_b are adjusted until the charge reaches the level of the net charge at zero bias.

For further details of the model, one may wish to read [13].

2.5 Model Results

Here is a summary of a few of the interesting results that came out of this model. For a comprehensive presentation of model results, one should read [13].

2.5.1 Symmetric molecule-electrode couplings

The simplest case for this model is that of equal molecule-source and molecule-drain couplings, with the HOMO-LUMO gap centred at E_F. Fig. 2.6(a) shows how the source and drain electrochemical potentials μ_S and μ_D, and the energies of the bonding (O) and antibonding ($O*$) orbitals behave when a bias is applied to the electrodes. Fig. 2.6(b) shows the electron transmission probability through the molecule at zero bias obtained from Eq. 2.8.

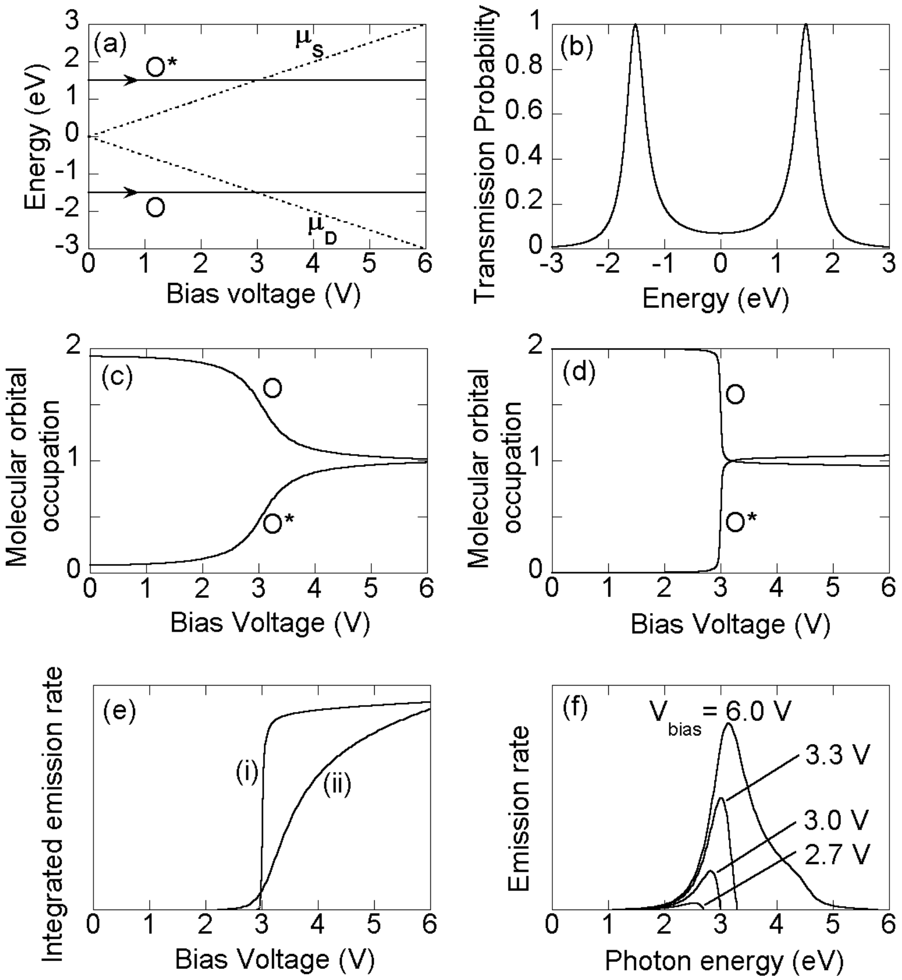

Figure 2.6: Symmetrically coupled molecular wires for which at zero bias the HOMO-LUMO gap is centered at the Fermi level of the contacts and $\varepsilon_{\text{contacts}} = \varepsilon_a = \varepsilon_b$. $\beta_{a,b} = -1.5$ eV in all cases. (a) Source and drain electrochemical potentials μ_S and μ_D and energies of the bonding (O) and antibonding ($O*$) orbitals as a function of bias voltage, for $\beta_{-1,a} = \beta_{1,b} = -1.0$ eV. (b) Probability for the transmission of an electron through the molecular wire as a function of electron energy, for $V_{\text{bias}} = 0$ and $\beta_{-1,a} = \beta_{1,b} = -1.0$ eV. (c) Occupations of the molecular bonding and antibonding orbitals, for $\beta_{-1,a} = \beta_{1,b} = -1.0$ eV, (d) for $\beta_{-1,a} = \beta_{1,b} = -0.2$ eV. (e) Total integrated photon emission, as a function of bias voltage, for (i) $\beta_{-1,a} = \beta_{1,b} = -0.2$ eV and (ii) $\beta_{-1,a} = \beta_{1,b} = -1.0$ eV. (f) Emission spectra for various different bias voltages ($\beta_{-1,a} = \beta_{1,b} = -1.0$ eV).

The bonding and antibonding orbitals provide channels for electron transmission. The transmission peaks undergo broadening. This is due to the coupling of the molecule to the electrodes, which causes the discrete molecular orbitals (O and $O*$) to hybridize with the continuum of states in the electrodes. The stronger the coupling between the molecule and the electrodes, the broader the transmission peaks. Looking at Fig. 2.6(a), as V_{bias} increases, the electrochemical potentials of the source (μ_S) and drain (μ_D) separate. At $V_{\text{bias}} = 3$ V, μ_S moves above $O*$ and μ_D moves below O. In this symmetric case, this does not result in any change in the energies of O and $O*$. Fig. 2.6(c) shows the electron occupation of the bonding (O) and antibonding ($O*$) orbitals of the molecular wire. As the electrochemical potentials of the source and drain electrodes cross the energies of O and $O*$, O empties, and $O*$ fills by an equal amount. The total occupation remains constant (two electrons). Therefore, in this symmetric case there is no tendency for the molecule to charge, and the orbital energies remain constant [Fig. 2.6(a)]. At high bias, both O and $O*$ are about half-filled, because only the source electrode contributes to the charge of the orbitals (and not the drain electrode).

Fig. 2.6(d) shows the orbital occupation for the case of weaker molecule-electrode coupling. The weak coupling leads to weaker hybridization of molecular orbitals with states in the electrodes, and results in a more sharply peaked molecular density of states. Therefore, O and $O*$ empty and fill much more abruptly.

Fig. 2.6(e) shows the resulting total emission rate for the stronger and weaker coupling cases. Emission is strong when the energies of O and $O*$ are inside the electrochemical potential window. Fig. 2.6(f) shows how, for this simple model, the emission spectrum for case (ii) changes with bias. As expected, emission is peaked at the transition energy of the molecule (3 eV) at higher bias. Since photons can not be emitted at energies higher than eV_{bias}, the spectra cut off at this energy. This contributes to the noticeable shift of the emission peak upwards in energy with increasing V_{bias}.

2.5.2 Asymmetric molecule-electrode couplings

By examining the effects of asymmetric molecule-electrode couplings, the behaviour of photon emission from systems such as STM/molecule/substrate may be explored. Fig. 2.7(a,b) shows a case of asymmetric couplings. The model predicts O and $O*$ to change in energy

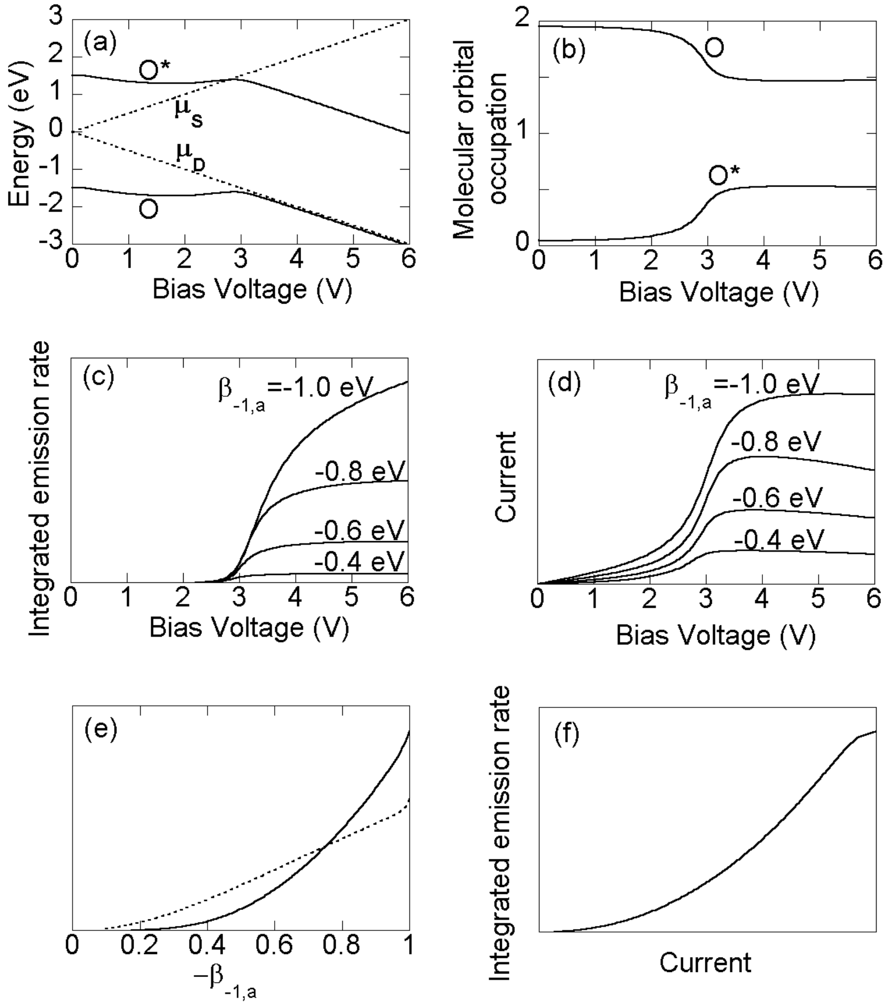

Figure 2.7: Asymmetrically coupled molecular wires: various asymmetric electrode couplings. (a)$\beta_{-1,a} = -0.6$ eV, $\beta_{1,b} = -1.0$ eV. Energies of the bonding (O) and antibonding ($O*$) orbitals as a function of bias voltage. (b) Occupations of O and $O*$, corresponding to the situation in (a). (c) Total photon emission rates, for various values of $\beta{-}1,a$. $\beta_{1,b} = -1.0$ eV in all cases. (d) Current for various values of $\beta_{-1,a}$. $\beta_{1,b} = -1.0$ eV in all cases. (e) Photon emission (solid line) and current (dotted line) as a function of source electrode coupling $\beta_{-1,a}$, for $\beta_{1,b} = -1.0$ eV, $V_{\text{bias}} = 6$ V. Vertical scales are arbitrary. (f) Total photon emission vs. current, for $\beta_{1,b} = -1.0$ V, $V_{\text{bias}} = 6$ V.

as a function of bias. Above $V_{bias} = 3$ V, both O and $O*$ descend in energy with μ_D. $O*$ partially fills as it is crossed by μ_S, but the drain is coupled more strongly to the molecule, and therefore affects the occupation of O to a greater degree. If μ_D entirely crossed O, it would significantly lower the total charge on the molecule. Therefore, the energy of the orbitals changes such that the net charge remains at the zero bias level. For this reason, above $V_{\text{bias}} = 3$ V, the orbital energies follow μ_D.

Fig. 2.7(c) shows photon emission for this case, and other degrees of coupling asymmetry. The degree of electrode coupling asymmetry clearly plays a key role in determining the strength of photon emission. The stronger the asymmetry, the weaker the photon emission. These results indicate that in order for an STM experiment to detect molecular-based photon emission, the STM tip must be relatively strongly coupled with the molecule, or else the substrate must have some sort of a ‘spacer’ layer that reduces the molecule-substrate coupling. Since coupling strength varies exponentially with coupling distance, any molecular-based photon emission observed in an STM experiment will be very sensitive to the tip-sample distance. If the tip is too far from the sample, emission will be negligible.

In order to more easily compare this prediction with potential experiments, it is useful to relate electrode coupling asymmetry to the amount of current flowing through a molecular wire as well, because, unlike coupling strength, current is a directly measurable quantity. Fig. 2.7(d) shows how the current [obtained from Eq. 2.2] changes with V_{bias} for various electrode asymmetries, analogous to Fig. 2.7(c) for photon emission. Asymmetric contact couplings result in reduced current flow. Notice, however, that the current flow is not affected by strongly asymmetric couplings as much as is the photon emission rate. Fig. 2.7(e) compares how photon emission and current depend on contact coupling asymmetry. Fig. 2.7(f) shows the calculated photon emission vs. current (at a constant bias of 6 V, with the electrode coupling asymmetry being varied). At weak currents, the photon emission rapidly becomes negligible.

The idea of needing reasonably symmetric tip-molecule and molecule-substrate coupling strengths in order to achieve significant photon emission is an important consideration to keep in mind when attempting to observe molecular photon emission experimentally. It should be noted that after this work was published,[13] experiments exploiting this principle were carried out, and produced for the first time convincing evidence of molecular-based electroluminescence.[11, 12]

The two cases presented in this section convey only a small fraction of the results that were achieved within this model - I believe surprisingly rich physics for such a simple model.

2.6 Conclusions

In this background section, various experiments were touched upon, which provide strong evidence for single molecule electroluminescence, and thus the motivation for an in-depth theoretical study of this phenomenon. As well, a simple first model of molecular electroluminescence that formed the basis of my Master's thesis is outlined, and a few of the interesting results of that model are included. Many of the concepts discussed in the subsequent sections of this thesis have their root in this elegant first model of photon emission.

It is hoped that, from reading this section, the reader will have a better idea of the experimental background, as well as the theoretical starting point, for the investigation of electroluminescence and scanning tunneling microscopy of single molecules that forms the rest of this thesis.

Chapter 3

A two-electrode approach to single molecule scanning tunneling microscopy

3.1 Introduction

In recent years, single molecule electroluminescence has moved from being a theoretical hypothesis with some experimental evidence,[13, 23] to being definitively demonstrated in STM experiments.[11, 12] In particular, STM experiments by Qiu, Nazin and Ho [11] on the molecule Zn-etioporphyrin have provided a rich set of data to which results of theoretical models may be compared. This data includes both standard STM topographs and current-voltage characteristics, as well as electroluminescence data including photon emission spectra *for the same system*. Thus, the experiment is unique in that it requires a theoretical approach that satisfies a larger number of observational degrees of freedom than are the norm for this field of physics.

As a first step to developing such a theory, a theoretical framework must be developed that gives us a basic understanding of the geometrical and electronic properties of the experimental system, while keeping in mind an electroluminescence analysis as a natural extension of such a framework.

As is explained in Sec. 3.2, the simple model outlined in Chapter 2 provides us with the ideal starting point for this investigation. In this chapter, scanning tunneling microscopy will be studied using a much more sophisticated version of the two-electrode approach, that allows for the study of a real molecule, and the creation of a corresponding STM current map.

3.2 A local electrode approach to scanning tunneling microscopy

Theoretical approaches to modelling STM-based electron flow commonly treat the tip as a probe of the molecule-substrate system. For example, the Bardeen[24] approximation considers the tip and sample to be two distinct systems that are perturbed by an interaction Hamiltonian. The Tersoff-Hamann formalism[25] calculates a tunneling current based on the local density of states (LDOS) of the tip and of the sample. Such approaches are widely used and have been very productive for the understanding of these systems. There has correspondingly been much interest in studying the tip-molecule interaction and the details of the coupling. However, details of the molecule-substrate coupling may also affect the electric current and the image of the molecule.

A number of different theoretical approaches[26, 27, 28, 29, 30, 31] have been developed that predict effects of molecule-substrate coupling,[32, 33, 34, 35, 36] in experimental situations where the substrate can be regarded as being effectively homogeneous. In many of these experimental situations, a molecule is placed directly on a metal substrate, resulting in strong coupling along the entire molecule-metal interface. While these types of experiments may be readily analyzed with known theoretical techniques, they are not conducive to observing molecular electroluminescence. As was first predicted theoretically[13, 23] and is discussed in Chapter 1 and in Sec. 2.5, molecular electroluminescence in STM systems is observed only if the molecule is not too strongly coupled to the underlying substrate; in practice, an insulating 'spacer' layer is usually found to be necessary to observe molecular-based photon emission.

For systems with such a 'spacer' layer, the theoretical approach that should be used to model STM current flow through the molecule is often not well-understood. Some of these systems do involve relatively simple substrates, including an insulating layer that behaves qualitatively like a uniform tunnel barrier[12, 37] and considerable progress has been made in understanding their STM images. However, for other systems showcasing impressive

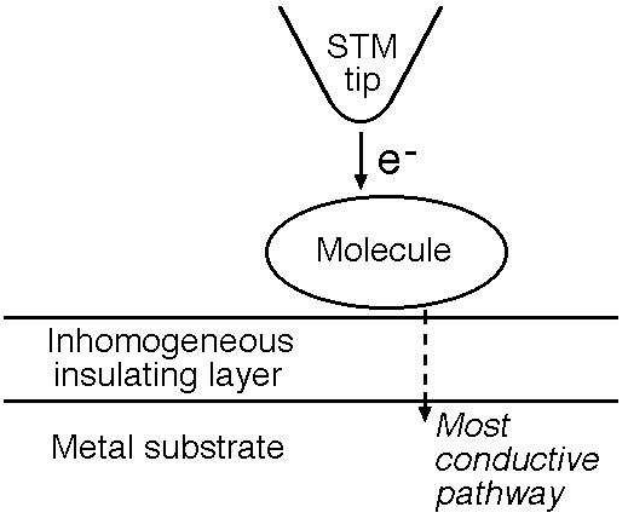

Figure 3.1: Illustrative diagram for an STM-molecule-substrate experiment, showing a possible pathway for electron transmission when the molecule is weakly bound to the substrate due to the presence of a complex insulating layer that transmits electrons non-uniformly. A region of dominant molecule-substrate coupling causes electron transmission to occur primarily through a single pathway.

arrays of experimental data, specifically systems with planar molecules on a 'spacer' layer of aluminum oxide (alumina) above a metal substrate,[11] *complex STM images are seen that depend on the precise location of the molecule on the substrate and are much less well understood.* For such systems, there is strong evidence[38] that the alumina film behaves (on the atomic scale) as a *nonuniform* tunnel barrier between the molecule on its surface and the metal substrate beneath it, and that electrons are transmitted between the molecule and substrate primarily at the more conductive spots of the alumina film.

For the case of the Zn(II)-etioporphyrin I molecules studied experimentally in Ref. [11], a *single* conductive spot of the film can dominate the electronic coupling between a suitably placed molecule and the underlying metal substrate. Thus, as shown schematically in Fig. 3.1, in an STM experiment on such a system, not only the STM tip but also the substrate should be regarded as a highly local electrode making direct electrical contact with a small part of the molecule. Therefore, conventional STM experiments on such systems can

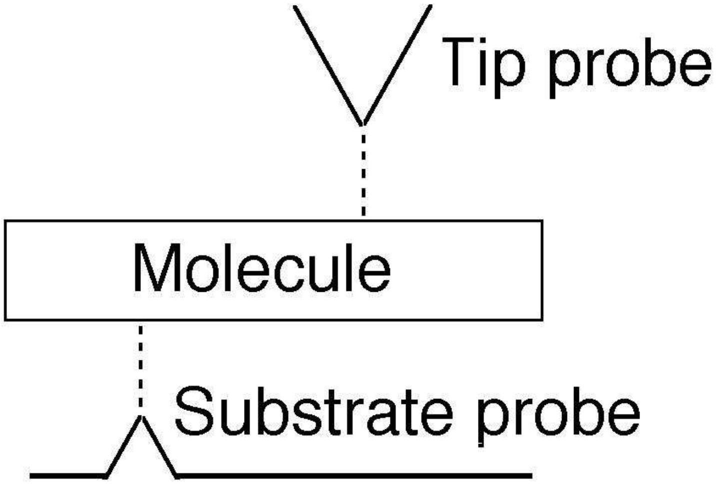

Figure 3.2: Illustration of a two-electrode theory of scanning tunneling microscopy. Tip and substrate are both considered to be local electrodes coupled to the molecule.

in principle yield information similar to that from experiments probing a single molecule simultaneously with two separate atomic STM tips, which are beyond the reach of present day technology. In Sec. 3.2-3.4, a model that builds on the simple approach of Chapter 2 is presented for modelling such systems. In Chapter 4, this approach is used to explain STM results of recent experiments.[11]

In the model, scanning tunneling microscopy of molecules is re-examined, treating the tip-molecule and molecule-substrate coupling on the same footing, both as *local* electrodes in contact with the molecule, as is shown schematically in Fig. 3.2. In this two-electrode model, the electrodes are represented, as in Chapter 2, using a one-dimensional tight-binding model, and electron flow is modelled using the Lippmann-Schwinger Green-function scattering technique, discussed in Sec. 3.3.1. An ‘extended molecule’ technique that simplifies calculations considerably is discussed in Sec. 3.3.2. In Sec. 3.3.3, the issue of non-orthogonality of atomic orbitals is discussed and dealt with elegantly. Sec. 3.4 addresses how to create a simulated STM topograph with this local electrode approach, so that model results may be compared with experimental data including actual STM topographs.

3.3 Electric current flow through a molecule

3.3.1 Electron transmission through a molecule

The electric current that flows through a molecule is related to the transmission probability for an electron to pass through the molecule, by way of the Landauer formalism,[18, 19] discussed for a simple system consisting of two electrodes and a simple two-orbital molecule in Chapter 2. In the present chapter, where the focus is on realistically modelling actual scanning tunneling microscopy experiments, the general approach of Chapter 2 is built upon, for current flow through a general molecule, with one of the two electrodes reperesenting the STM tip and the other electrode the region of dominant molecule-substrate coupling. A more sophisticated Lippmann-Schwinger approach to the scattering problem for this system is implemented.

In the present model, each electrode (representing the tip and the substrate) is modelled as a one-dimensional tight-binding chain, as is depicted in Fig. 3.3. In order to solve the scattering problem for this system in an elegant way using the Lippmann-Schwinger approach (discussed later in this section), the model Hamiltonian must be divided into three parts, $H = H_{\text{electrodes}} + H_{\text{molecule}} + W$, where W is the interaction Hamiltonian between the electrodes and the molecule. The Hamiltonian for the electrodes, similar to that presented in Sec. 2.2 but with one electrode representing the tip and the other the substrate, is given by

$$\begin{aligned} H_{\text{electrodes}} = & \sum_{n=-\infty}^{-1} \varepsilon_T |n\rangle\langle n| + \beta(|n\rangle\langle n-1| + |n-1\rangle\langle n|) \\ & + \sum_{n=1}^{\infty} \varepsilon_S |n\rangle\langle n| + \beta(|n\rangle\langle n+1| + |n+1\rangle\langle n|), \end{aligned} \tag{3.1}$$

where ε_T and ε_S are the site energies of the tip and substrate electrodes, β is the hopping amplitude between nearest-neighbour sites, and $|n\rangle$ represents the valence orbital at site n of one of the electrodes.

When a bias voltage is applied, the electrochemical potentials of the tip and substrate shift. In this model, it is assumed that any potential drop that occurs within the molecule can be neglected, because the experimental molecule that our model results will be compared

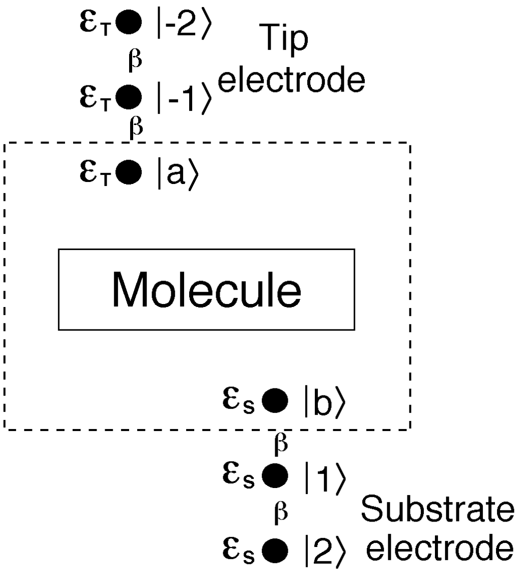

Figure 3.3: A schematic diagram of the model STM-molecule-substrate system. The tip and substrate electrodes are semi-infinite. Nearest-neighbour atoms to the molecule (with atomic orbitals labeled $|a\rangle$ and $|b\rangle$) are considered to be part of the *extended molecule*, discussed in Sec. 3.3.2, which is bounded by the dashed rectangle.

with in Chapter 4, Zn(II)-etioporphyrin I, is a thin and mainly planar molecule. Therefore, the electrochemical potentials of the tip and substrate electrodes are taken to be $\mu_T = E_F + eV_{\text{bias}}/2$ and $\mu_S = E_F - eV_{\text{bias}}/2$, where E_F is their common Fermi level at zero applied bias. The applied bias also affects the site energies ε_T and ε_S so that $\varepsilon_T = \varepsilon_{0,\text{tip}} + eV_{\text{bias}}/2$ and $\varepsilon_S = \varepsilon_{0,\text{substrate}} - eV_{\text{bias}}/2$, where $\varepsilon_{0,\text{tip}}$ and $\varepsilon_{0,\text{substrate}}$ are the site energies of the tip and substrate at zero bias.

The Hamiltonian of the molecule may be expressed as

$$H_{\text{molecule}} = \sum_j \varepsilon_j |\phi_j\rangle\langle\phi_j|, \tag{3.2}$$

where ε_j is the energy of the jth molecular orbital ($|\phi_j\rangle$).

The electronic coupling between the electrodes and molecule is described by a term in the Hamiltonian given by

$$W = \sum_j W_{-1,j}|-1\rangle\langle\phi_j| + W_{j,-1}|\phi_j\rangle\langle -1| + W_{j,1}|\phi_j\rangle\langle 1| + W_{1,j}|1\rangle\langle\phi_j|, \tag{3.3}$$

where $W_{-1,j}$, $W_{j,-1}$, $W_{j,1}$ and $W_{1,j}$ are the hopping amplitude matrix elements between the electrodes and the various molecular orbitals $|\phi_j\rangle$.

Electrons initially propagate through one of the electrodes (which we will assume to be the tip electrode) toward the molecule in the form of Bloch waves, and may undergo either reflection or transmission when they encounter the molecule. Their wavefunctions are of the form

$$|\psi\rangle = \sum_{n=-\infty}^{-1} (e^{iknd} + re^{-iknd})|n\rangle + \sum_{n=1}^{\infty} te^{ik'nd}|n\rangle + \sum_j c_j|\phi_j\rangle \tag{3.4}$$

where d is the lattice spacing, and t and r are the transmission and reflection coefficients. As in Sec. 2.2, the energy band for this system may be obtained by by performing the simple calculation $\langle n|H|\psi\rangle = E\langle n|\psi\rangle$, with the result obtained being $E = \varepsilon_{\text{electrode}} + 2\beta cos(kd)$, where k is the wavevector of an electron on the electrode, and $\varepsilon_{\text{electrode}}$ represents either the tip or substrate. Upon transmission, the wavevector k changes to k' due to the difference in site energies ε_T and ε_S of the tip and substrate electrodes. The transmission probability is given by

$$T = |t|^2 \left|\frac{v(k')}{v(k)}\right| = |t|^2 \frac{sin(k'd)}{sin(kd)} \tag{3.5}$$

where $v(k)$ and $v(k')$ are the respective velocities of the incoming and transmitted waves. Notice that in this case, the transmitted electron velocity is not the same as the initial velocity, due to its well-known relation to its energy and wavevector, $v(k) = \frac{1}{\hbar}\frac{dE}{dk}$, and the fact that the transmitted electron wave has a different wavevector from the initial wavevector.

The transmission amplitude t may be evaluated by solving a Lippmann-Schwinger equation for this system. The Lippmann-Schwinger approach to scattering involves separating the part of the Hamiltonian that couples with the scattering centre from the rest of the Hamiltonian. In the case of this model, H has been split into $H_0 = H_{\text{electrodes}} + H_{\text{molecule}}$ (the decoupled Hamiltonian) and the interaction term W. It has been shown, in general, that the following equation form satisfies the scattering condition:

$$|\psi\rangle = |\phi_0\rangle + G_0(E)W|\psi\rangle, \tag{3.6}$$

where $G_0(E) = (E - H_0 + i\delta)^{-1}$ is the Green function for the decoupled system (without W), and $|\phi_0\rangle$ is the eigenstate of an electron in the decoupled system.[41]

In this model, $G_0(E)$ may be separated into three decoupled components: the tip and substrate electrodes, and the molecule. For the tip/substrate electrodes,

$$G_0^{\text{Tip/Substrate}} = \sum_k \frac{|\phi_0(k_{T/S})\rangle\langle\phi_0(k_{T/S})|}{E - (\varepsilon_{T/S} + 2\beta cos(k_{T/S}d))} \tag{3.7}$$

where d is the lattice spacing and $\varepsilon_{T/S} + 2\beta cos(k_{T/S}d)$ is the energy of a tip/substrate electron with wavevector $k_{T/S}$. For the molecule,

$$G_0^M = \sum_j \frac{|\phi_j\rangle\langle\phi_j|}{E - \varepsilon_j} = \sum_j (G_0^M)_j |\phi_j\rangle\langle\phi_j|. \tag{3.8}$$

The transmission probability for such a system using this formalism has been previously solved[42], and found to be equal to

$$T(E) = |\frac{A(\phi_0)_{-1})}{[(1-B)(1-C) - AD]}|^2 \frac{sin(k_0'd)}{sin(k_0 d)} \tag{3.9}$$

where $(\phi_0)_{-1} = \langle -1|\phi_0\rangle$, and

$$\begin{aligned}
A &= (e^{ik_0'd}/\beta)\sum_j W_{1,j}(G_0^M)_j W_{j,-1} \\
B &= (e^{ik_0'd}/\beta)\sum_j (W_{1,j})^2 (G_0^M)_j \\
C &= (e^{ik_0 d}/\beta)\sum_j (W_{-1,j})^2 (G_0^M)_j \\
D &= (e^{ik_0 d}/\beta)\sum_j W_{-1,j}(G_0^M)_j W_{j,1}.
\end{aligned} \tag{3.10}$$

Here, k_0 is the wavevector of an electron in the tip electrode with energy E, and k_0' is the wavevector of an electron in the substrate electrode, of the same energy E.

The transmission probability may then be integrated through the window of energy that is located between the electrochemical potentials of the tip (μ_T) and substrate (μ_S) when a bias voltage is applied, following Eq. 2.3. This assumes the tip to be the source electrode and the substrate to be the drain electrode. The electric current through the molecule is obtained.

3.3.2 The ‘extended molecule’

By using the Lippmann-Schwinger approach to scattering, we are free to choose convenient boundaries for the central scattering region, not necessarily restricted to the actual molecule. The Lippmann-Schwinger formalism that has been developed is mathematically rigorous, and does not depend on any approximate physical boundary between the electrodes and the scattering region. In order to model the coupling between the electrodes and the molecule in a realistic way, the electrode atoms that are closest to the molecule are considered to be part of an *extended molecule* (see Fig. 3.3), ie. in the formalism they are treated as parts of the scattering centre (molecule).

Looking at Fig. 3.3, since the electrode orbital $|-1\rangle$ is coupled to the extended molecule only through orbital $|a\rangle$, the term $W_{-1,j}$ between the electrode orbital $|-1\rangle$ and the jth molecular orbital may be expressed as

$$W_{-1,j} = W_{j,-1} = \langle -1|H|a\rangle\langle a|\phi_j\rangle = \beta c_{a,j}, \tag{3.11}$$

where $\langle -1|H|a\rangle = \beta$, and $c_{a,j} = \langle a|\phi_j\rangle$ by definition.

Thus, the connection term between the electrodes and molecule is greatly simplified, at the expense of the introduction of a slightly more complex ‘extended molecule.’

3.3.3 The molecular Hamiltonian: Extended Hückel Theory

In order to solve the scattering problem, all of the molecular orbital energy levels ε_j, as well as the coefficients $c_{a,j} = \langle a|\phi_j\rangle$ and $c_{b,j} = \langle b|\phi_j\rangle$ must be obtained.

The molecule is a complicated quantum mechanical system with many interacting electrons. Approximations must be made in order to try to reflect the most important aspects of the physics involved. A relatively simple technique - the extended Hückel approach - has proven to be a highly effective tool in quantum chemistry. It is widely used to obtain simple first estimates for the energy level structures of various molecules.

Extended Hückel (EH) theory builds on the tight-binding approach that has been used to describe electron flow in the tip and substrate electrodes, in order to describe electron behaviour in the molecule itself. While the tight-binding approach is restricted to nearest-neighbour electron hopping and assumes atomic orbitals to be orthogonal, in EH the molecular system is described using a non-orthogonal set of atomic orbitals $|\phi_m\rangle$, and there is no such restriction of hopping to nearest neighbours.

The non-orthogonality of the orbitals generates an overlap matrix $S_{m,n}$ that is defined as $S_{m,n} = \langle\phi_m|\phi_n\rangle$. In the EH theory, the site energies ε_m of the atomic orbitals are given by the negatives of the corresponding orbital ionization energies that have been determined experimentally.

Within EH, there are many different approximate forms for determining hopping amplitudes between atomic orbitals. One common, simple form known as the Wolfsberg-Helmholz form of EH,[43] defines the hopping amplitude as follows:

$$\langle\phi_m|H|\phi_n\rangle = H_{m,n} = K\frac{S_{m,n}}{2}(\varepsilon_m + \varepsilon_n) \tag{3.12}$$

where K is usually chosen to be 1.75. This goes beyond nearest neighbour hopping and allows for a non-orthogonal basis.

In order to perform the extended Hückel calculations for results in this thesis, a computer program implementation known as Yaehmop[44] (Yet Another extended Hückel Molecular Orbital Package) has been used. Yaehmop uses a somewhat more complex and more accurate form of EH to calculate hopping amplitudes than the Wolfsberg-Helmholz form, but the idea is the same.

There are other competing, more sophisticated approaches than extended Hückel for calculating the necessary energy levels and hopping amplitudes, such as density functional theory (DFT). However, as will be discussed in Sec. 4.3, DFT has problems when attempting to calculate molecular orbital energy levels and hopping amplitudes for many molecular systems,[45, 46, 47, 48, 49, 50, 51, 52, 53, 54, 55, 56] including the primary experimental system of interest for this thesis.

3.3.4 Non-orthogonal atomic orbitals

The extended Hückel method requires the use of a non-orthogonal basis, in which orbitals on differing atomic sites may overlap. However, the approach to scattering outlined in this chapter assumes all orbitals are orthogonal to each other.

For the model presented in this chapter, the Hamiltonian for the molecule is expressed as $H_{\text{molecule}} = \sum_j \varepsilon_j |\phi_j\rangle\langle\phi_j|$ (from Eq. 3.2), ie. it is expressed in an orthogonal molecular orbital basis, with orbital energies ε_j being the eigenvalues, and not in an atomic orbital basis. (Orbital energies ε_j are computed in an earlier step, using the Yaehmop implementation of extended Hückel theory.) Therefore, for the specific model presented here, all orbitals (including tip and substrate electrodes, as well as orbitals $|\phi_j\rangle$ on the molecule, are in fact orthogonal to each other.

Enhanced models, however, may incorporate nonorthogonality of tip and substrate electrode orbitals, including overlap terms between nearest neighbour electrode orbitals as well as between electrode orbitals and molecular orbitals, in a rather elegant way.

The standard technique for dealing with non-orthogonal bases is to use a transformation which changes the non-orthogonal basis into an orthogonal one, such as Gram-Schmidt orthogonalization[57]. By doing this, however, one changes the basis from the original physically simple atomic orbital basis, to a new basis lacking this simplicity. Instead, summarizing the results of Emberly and Kirczenow,[42], one can change the Hilbert space in such a way that the basis becomes orthogonal, without the use of any basis set transformation.

This is done simply by replacing the Hamiltonian H of a non-orthogonal basis, with a new energy-dependent Hamiltonian H^E. The matrix elements of H^E are related to H in the following way:

$$H^E_{m,n} = H_{m,n} - E(S_{m,n} - \delta_{m,n}) \tag{3.13}$$

To change a non-orthogonal scattering problem into an orthogonal one, one simply replaces the original Hamiltonian matrix elements with new elements as shown in Eq. 3.13.

For the Lippmann-Schwinger methodology, the result is a new energy-dependent Green function $G_0(E) = (E - H^E + i\delta)^{-1}$. The coupling matrix elements are also transformed: $W^E_{i,j} = W_{i,j} - ES_{i,j}$.

Results presented in Chapter 4 are based on orthogonal orbitals. However, it is important for completeness to understand how it is also possible, in an elegant way, to achieve the orthogonal basis necessary to solve a scattering problem of the form presented in this chapter, from the starting point of a nonorthogonal basis.

3.4 Creating an STM current map

Having obtained the electric current through integration of electron transmission probability through the appropriate energy range, an STM current map may now be simulated.

Holding the position of the substrate electrode below the molecule fixed, the lateral location of the tip electrode above the molecule may be varied in order to construct a simulated STM current map. A current map obtained in this way is equivalent to an experimental constant height STM image of a molecule (where the STM tip is fixed at a certain height, and moves laterally across the molecule).

Experimentally, STMs are frequently operated in constant current mode, rather than constant height mode. In constant current mode, the electric current for one lateral position of the tip is first measured. Then, the tip is moved laterally across the molecule. If the current at the new location is higher (or lower), the tip is moved away from (or closer to) the molecule, until the current matches the current measurement at the initial lateral position. This is done partly to protect the STM tip from surface defects which the tip may run into, if in constant height mode.

In the experiment of interest,[11] STM topographs are generated in constant current mode. However, in order to model STM results in this way, an extra self-consistent calculation would have to be performed, with the tip electrode moving not only laterally but also vertically. This would be very time-consuming and computer-intensive: Generating a single simulated STM current map in constant height mode takes about 2 days, using 8 nodes of SFU's Bugaboo high-performance computing cluster. Since this is the first model to use the local electrode approach in this way, and since generally it is found in experiment that constant current topographs usually give qualitatively similar images to constant height topographs (because being a tunnelling current, the STM tip current at constant bias is normally a monotonically (exponentially) decreasing function of tip height), constant height mode simulation was considered to be satisfactory.

Once a current map for a fixed location of the substrate electrode is generated, it may be compared with current maps for other locations of the substrate electrode. The substrate electrode represents the region of dominant molecule-substrate coupling. For many experimental systems, particularly those with a complex ‘spacer’ layer, the details of the molecule-substrate coupling are not known. The beauty of the local electrode approach is that it allows insight into how the details of the molecule-substrate coupling may affect the STM image of the molecule. We may therefore study in a simple way, using the local electrode approach presented in this chapter, the interplay between tip-molecule coupling and molecule-substrate coupling and how it affects the STM image of the molecule.

In the next chapter, a molecule of current experimental interest,[11] Zn(II)-etioporphyrin I will be considered. Various simulated constant-height STM current maps of the molecule obtained using different substrate electrode locations, corresponding to different possible locations of dominant molecule-substrate coupling, will be compared. It will be demonstrated how the properties of an STM current image may display a remarkable *qualitative* dependence on the location of this dominant molecule-substrate coupling. The simulated maps are then compared to experimental data, with interesting results.

Chapter 4

Investigating the scanning tunneling microscopy of Zn-etioporphyrin

4.1 Introduction

As touched upon in Sec. 2.1, STM experiments performed on the molecule Zn(II)-etioporphyrin I, above a 'spacer' layer of Al_2O_3 on a NiAl(110) substrate[11] have yielded an intriguing array of results. From definitive molecular electroluminescence data, to current-voltage characteristics, to STM topographs, that all depend on the location of the molecule on the surface and are all correlated with each other, there is truly an abundance of data to be understood. Understanding the data, however, is not a straightforward process. Because the molecule lies above a complex 'spacer' layer, the details of the molecule-substrate coupling are unknown and variable, dependent on the location of the molecule on the surface.

The focus of this chapter is to investigate the scanning tunneling microscopy of Zn-etioporphyrin using the model developed in Chapter 3, with a particular focus on explaining the variations in STM topographic images that are seen experimentally. The first step to understanding the data is to, as best we can, understand the system itself; particularly, how the molecule may be coupled to the substrate, and the interplay of this coupling with the tip-molecule coupling, that results in differences in STM topographs.

The model that I have developed[58] is ideally suited to this task, because, unlike many others models, it does not use as a starting point a precisely pre-determined molecule-substrate junction geometry with which to commence sophisticated calculations. The assumption, rather, is that through the complex Al_2O_3 ‘spacer’ layer there may be one or more regions of dominant molecule-substrate coupling, and the location of these regions relative to the molecule may vary depending on the position of the molecule on the substrate. Modelling a complex, precisely pre-defined junction geometry is neither necessary nor advisable, as the the junction geometry is experimentally variable. Rather, the two electrode approach presented in Chapter 3 is ideal as a first approximation, since electrode locations may easily be varied and results compared.

The geometrical structure of Zn-etioporphyrin is studied in Sec. 4.2. In Sec. 4.3 the electronic structure of the system is calculated, and there is a comparison of two common approaches for this type of calculation: the extended Hückel approach, and density functional theory (DFT). In Sec. 4.4 and Sec. 4.5, model results, in the form of transmission curves and simulated STM current maps, are presented and carefully analyzed for two possible electronic configurations of the system. These results are compared with experiment in Sec. 4.6, and the chapter is concluded in Sec. 4.7.

4.2 Geometrical structure of Zn-etioporphyrin

Zn(II)-etioporphyrin I is a mainly planar molecule, consisting of four pyrrole-like rings (C_4N), a central zinc atom and an outer region composed of carbon and hydrogen (see Fig. 4.1). The molecule contains four out-of-plane ethyl groups (C_2H_5).

Density functional theory (DFT) was used in obtaining the molecule’s geometrical structure.[59]. To do this, an approximate geometry is first estimated, by considering known bond lengths and bond angles for similar types of molecules. Once a reasonable estimate of the molecular geometry is obtained, DFT is invoked and the molecule’s precise geometry is obtained by ‘relaxing’ the molecule. This geometrical relaxation is performed by slightly altering the geometry of the molecule until the state of lowest total energy is reached. (It should be noted that DFT is considered to be a fundamentally sound approach for determining the total energy of a molecule, as distinct from determining specific properties of the individual molecular orbitals.)

The relaxed geometry of Zn-etioporphyrin is listed in Appendix A.

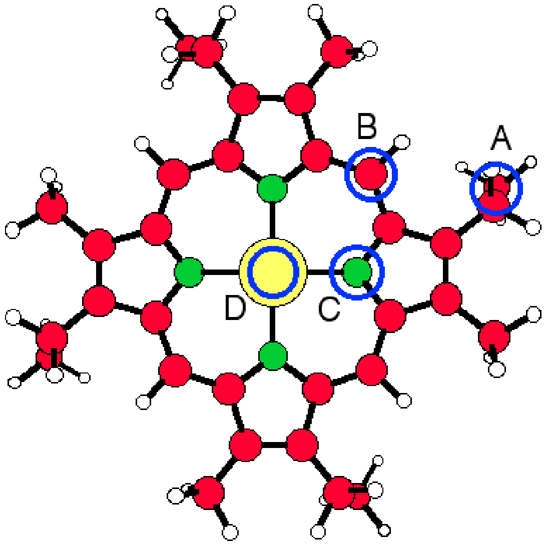

Figure 4.1: The Zn(II)-etioporphyrin I molecule. Carbon atoms are red, nitrogen atoms are green, the zinc atom is yellow, and hydrogen atoms are white. The four blue circles labeled A, B, C, and D denote four possible positions for the substrate electrode below the molecule (into the page), that are considered. In each case, the closest atom in the substrate electrode (atomic orbital $|b\rangle$ in Fig. 3.3) is 2.5 Å below the nearest atom of the molecule.

4.3 Electronic structure of the system

In order to obtain model results, various electronic parameters must first be determined.

For simplicity, the tip and substrate electrodes are represented by Cu *s* orbitals, with zero-bias site energies $\varepsilon_{0,\mathrm{tip}} = \varepsilon_{0,\mathrm{substrate}} = -11.4$ eV.[44] In the model, the 'extended molecule' atoms *a* and *b* are actually to be thought of as electrode atoms as well (see Fig. 3.3; therefore, $\varepsilon_a = \varepsilon_b = -11.4$ eV as well. The electrode hopping amplitude β is chosen to be -5.0 eV, corresponding to a reasonable band width of 20 eV through the formula $E = 2\beta cos(kd)$. (This formula is introduced in Sec. 2.2). The connection terms to the 'extended molecule' electrode atoms are the same: $\beta_{-1,a} = \beta_{1,b} = \beta = -5.0$ eV).

This leaves the 'extended molecule' coefficients $c_{a,j}$ and $c_{b,j}$ to be determined, as well as the 'extended molecule' orbital energies ε_j and the zero-bias Fermi energy of the electrodes. To calculate these quantities, there are a number of approaches that could be used, including density functional theory (DFT) and the extended Hückel approach (EH).

DFT is a formally more sophisticated *ab initio* (first principles) approach than semi-empirical EH. With *ab initio* ground state DFT, the difficult many-body problem of interacting electrons in a static external potential is reduced to a problem of non-interacting electrons in an effective potential. The effective Kohn-Sham (KS) potential includes the external potential and the effects of the Coulomb interactions between the electrons. The electron density is determined by minimizing the energy functional E[n] for the system, where n is the electron density.

Problems occur when attempts are made at using DFT to predict transport properties of molecular wires. For instance, while DFT does a good job of predicting the electron density for the systems, it is not designed to accurately predict unoccupied orbital energies, or the energy offset between the molecular energy levels and the Fermi energy of metal or semiconductor electrodes commonly used to contact molecules, necessary requirements for modelling transport. References [45, 55] describe some of the problems, particularly for the weak coupling regime, in detail.

Since the weak coupling regime is the regime of interest for this thesis, DFT is not an appropriate approach to use. I discovered this first by calculating the overlap matrix of atomic orbitals for the Zn-etioporphyrin ‘extended molecule’, using DFT[59] to generate Kohn-Sham orbitals and converting to a basis of real atomic orbitals. It was noticed that in DFT-based calculations the electrode atomic orbitals, at large distances (5 Å) from the molecule, had artificially high overlap matrix elements with atomic orbitals in the molecule (overlaps on the order of several tenths). This compares very poorly with what is obtained using EH, and likely occurs due to the inadequacy of the basis sets normally used with DFT[59] in this regime.

Instead, the semi-empirical extended Hückel approach (described in Sec. 3.3.3) is adopted, in order to calculate the necessary coefficients and orbital energies. This approach has proven to be remarkably successful for its simplicity, often generating approximately correct molecular orbital energy level structures and molecular orbital eigenvectors in a linear combination of atomic orbitals (LCAO) basis. EH is an ideal approach to use as a starting point to study previously unexplained experimental phenomena,[60, 61, 62, 63] particularly when part of the problem is that the system itself is not well-understood, as is the case here.[11]

orbital	energy
$HOMO-2$	-11.9 eV
$HOMO-1$	-11.8 eV
$HOMO$	-11.5 eV
$LUMO$	-10.0 eV

Table 4.1: The electronic structure of Zn(II)-etioporphyrin I, calculated using extended Hückel theory.[44]

The relevant molecular orbital energies calculated using EH are given in Table 4.1.

The Fermi level of a metallic electrode in contact with a molecule at zero applied bias is usually located between molecular HOMO and LUMO levels. However, establishing the precise position of the Fermi energy of the electrodes relative to the HOMO and LUMO is in general a difficult problem in molecular electronics, with different theoretical approaches yielding differing results.[64, 65, 66]

Within the present model, two possible zero-bias Fermi energy positions are considered for the electrodes: In the *LUMO-mediated transmission* subsection (Sec. 4.4), the Fermi energy is taken to be -10.4 eV. This value is predicted by an EH cluster calculation for a Cu electrode, where larger and larger Cu clusters are analyzed until there is a convergence in Fermi energies. Thus, at $V_{bias} = 1.0$ V, the Fermi energy window will include the LUMO but not the HOMO. In the *HOMO-mediated transmission* subsection (Sec. 4.5), the Fermi energy is taken to be -11.4 eV. In this case, at $V_{bias} = 1.0$ V, the Fermi energy window will include the HOMO, HOMO-1, and HOMO-2, but not the LUMO.

Here, the molecular levels are assumed not to shift with bias, unlike in other chapters of this thesis. This is acceptable, because only one bias value is considered ($V_{bias} = 1.0$ V), so that any collective shift of orbital energies with bias may be expressed instead as a difference in the zero-bias Fermi energy of the electrodes, whose value is not known accurately and is treated as an adjustable parameter here.

4.4 LUMO-mediated transmission

First considered is the case of electron transmission through the molecule at LUMO energies. For this, V_{bias} is set to be 1.0 V, with $E_F = -10.4$ eV at zero bias. The substrate electrode is now positioned to simulate various possible locations of dominant molecule-substrate coupling. Four different positions for the substrate electrode are analyzed, as shown by the blue circles in Fig. 4.1: directly below one of the outer ethyl groups of the molecule (A), below an inner carbon atom of the molecule (B), below a nitrogen atom (C), and below the zinc center of the molecule (D). The orbital representing the substrate electrode, in each case, is centered 2.5 Å below the nearest atom in the molecule. [It is assumed here that the ethyl groups of the molecule point towards the substrate. In Sec. 4.6, an alternative possibility, that the ethyl groups point *away* from the substrate, is considered.] Constant-height STM current maps for these substrate electrode positions are simulated by moving the tip electrode across the molecule in steps of 0.25 Å, calculating the electric current at each step, thus creating a 16 X 16 Å electric current map. The tip electrode in all cases is located 2.5 Å above the plane of the molecule.

Fig. 4.2(a)-4.2(d) show the simulated current maps obtained in each case, calculated using Eq. 2.3 and Eq. 3.9, the blue circle indicating the position of the substrate electrode. Each map has unique features not seen in the other maps, that arise due to differences in the details of the molecule-substrate coupling. In Fig. 4.2(a), with the substrate electrode positioned below an outer ethyl group as shown in Fig. 4.1 (position A), a delocalized current map is obtained. This means that for many different locations of the STM tip above the molecule, there is moderately strong electron transmission through the molecule. This is due to mediation of electron flow through the molecule by delocalized molecular orbitals, as will be discussed later in this section. A *localized* region of enhanced transmission also exists, where the tip electrode is directly above the same ethyl group that is coupled to the substrate electrode.

In Fig. 4.2(b), a somewhat similar current map is obtained, with the substrate electrode positioned below an inner carbon atom (see Fig. 4.1, position B). In this configuration, however, the current map has two-fold symmetry and there is no apparent single localized region of enhanced transmission. Furthermore, the lobes of high transmission in Fig. 4.2(b) are 1-2 orders of magnitude stronger than the corresponding lobes in Fig. 4.2(a), as will be discussed below.

In the case when the substrate electrode is directly below a nitrogen atom (see Fig. 4.1, position C), a distinct current map is obtained, shown in Fig. 4.2(c). The lobe with the highest current in this figure is 1-2 orders of magnitude weaker than lobes seen in

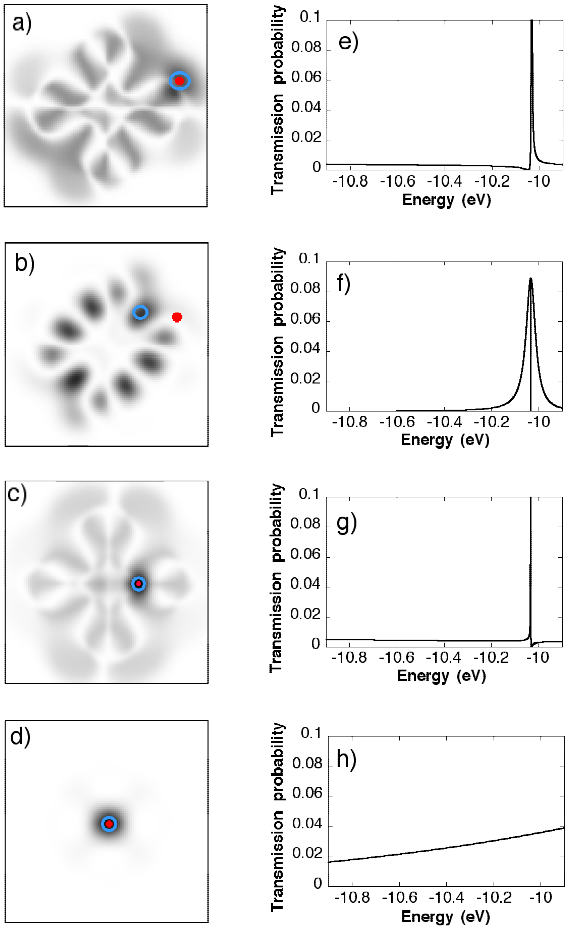

Figure 4.2: Calculated current maps and transmission at LUMO energies. (a)-(d) 16 X 16 Å constant-height current maps, for four different substrate electrode positions. Darker regions represent tip electrode positions that give higher current flow through the molecule. The blue circles represent the position of the substrate electrode below the molecule in each case, the closest atom of the electrode being 2.5 Å below the nearest atom of the molecule. These positions correspond to the blue circles in Fig. 4.1: (a) circle A, (b) circle B, (c) circle C, (d) circle D. The relative strengths of currents in the darkest regions of (a), (b), (c), and (d) are: 1 (a) : 40 (b) : 1 (c) : 6 (d). [Note that if the substrate electrodes were instead positioned equal distances below the *plane* of the molecule, the substrate electrode position in Fig. 4.2a would produce the strongest current, as discussed in Sec. 4.6.] The red dots represent tip electrode positions for the corresponding T(E) curves shown in (e)-(h), respectively. (e) Transmission vs. energy for tip and substrate electrodes directly above and below an outer ethyl group. (f) T(E) for the tip electrode above the same ethyl group but the substrate electrode below an inner corner carbon atom. (g) T(E) for tip and substrate electrodes above and below a nitrogen atom. (h) T(E) for tip and substrate electrodes above and below the central zinc atom. In all cases, the tip electrode is 2.5 Å above the plane of the molecule.

Fig. 4.2(b). In this case, a localized region of enhanced transmission exists where the tip electrode is above the same nitrogen atom that is coupled to the substrate electrode.

Fig. 4.2(d) shows a very different current map. In this case, the substrate electrode is positioned directly below the central zinc atom of the molecule (Fig. 4.1, position D), and transmission is found to occur primarily when the tip electrode is above the center of the molecule.

In order to help understand the differences between these maps, the characteristics of the LUMO were investigated. The LUMO is a doubly degenerate π-like orbital with two-fold symmetry. (See Appendix B for a 3-dimensional representation of the LUMO orbitals.) Analyzing the LUMO as a linear combination of atomic orbitals, it is found that contributions to the LUMO come primarily from atomic orbitals in the core porphyrin structure, with low contributions from the ethyl groups and the central zinc atom. Particularly high contributions come from two of the four inner corner carbon atoms (the atom above substrate electrode B and the corresponding atom 180 degrees away, in Fig. 4.1, or the equivalent atoms under rotation of 90 degrees for the other degenerate LUMO orbital). Therefore, in the case of Fig. 4.2(b), there is a strong coupling between the substrate electrode and one of the two degenerate LUMOs of the molecule, whereas in the case of Fig. 4.2(a), with the substrate electrode below the ethyl group, there is only a weak substrate-LUMO coupling. This explains why the current map of Fig. 4.2(b) is much stronger than Fig. 4.2(a).

Regarding the similar appearance of the current maps in the two cases, LUMO-mediated transmission is expected to occur, in both cases, when the tip electrode has significant coupling to the LUMO. The delocalized current maps of Fig. 4.2(a) and Fig. 4.2(b) in fact correspond well to areas of high atomic orbital contributions to the LUMO, with the low-transmission nodes occuring in regions of the molecule where the amplitude of the LUMO is close to zero.

The differences between the current maps may be better understood by studying the electron transmission probability T(E) for appropriate tip electrode positions in each case. Fig. 4.2(e)-4.2(h)) shows T(E) for the corresponding placement of the *tip electrode as labelled by the red dots in Fig. 4.2(a)-4.2(d)*.

In Fig. 4.2(e), T(E) is shown for the localized region of enhanced transmission in Fig. 4.2(a). There is a transmission resonance associated with the LUMO (at -10 eV), together with an antiresonance (ie. zero transmission) that occurs at a slightly lower energy. The antiresonance, along with antiresonances seen in subsequent figures (with the exception of the antiresonance in Fig. 4.2(f)), arises due to interference between electron propagation through a weakly coupled orbital (in this case the LUMO) and propagation through other orbitals of different energies. This can be seen mathematically through Eq. (3.9) and Eq. (3.10). Transmission drops to 0 when $A = 0$. This occurs when all the terms $W_{1,j}(\frac{1}{E-\varepsilon_j})W_{j,-1}$ for the different orbitals sum to 0. If an orbital is weakly coupled to the electrodes, its contribution to A is small unless the electron energy is close to the energy of the orbital. When the electron energy does approach this orbital energy, the contribution to A will increase and, if its sign is opposite, cancel the other orbitals' contributions. Thus, these types of antiresonances are always seen on only one side of a transmission peak of a weakly coupled orbital.

Returning to Fig. 4.2(e), we see that, although transmission via the LUMO contributes some of the electric current, a significant contribution comes from the background. It was found that this background transmission is composed primarily of the high energy transmission tails of molecular orbitals localized on the ethyl groups. When the tip electrode is coupled to the same ethyl group as the substrate electrode, transmission via these ethyl-composed molecular orbitals is strong and has a significant tail extending to the relevant range of energies near the LUMO.

Fig. 4.2(f) shows T(E) for the same tip electrode position as Fig. 4.2(e), but with the substrate electrode positioned below an inner carbon atom, as in Fig. 4.2(b). Since the substrate electrode is *not* in this case significantly coupled to the ethyl group, the ethyl-based transmission background is negligible, and the region of locally enhanced transmission seen in Fig. 4.2(a) is not seen in Fig. 4.2(b). It should also be noted that the transmission peak in Fig. 4.2(f) is wider than in Fig. 4.2(e), due to hybridization of the LUMO with the strongly coupled substrate electrode. This broadening is a similar effect to that presented and discussed in Sec. 2.5.1 for the simple two-atom molecule. The antiresonance seen at the center of the peak is due to the degeneracy of the LUMO. In this case, one of the LUMO orbitals is strongly coupled to the substrate electrode, with the other being only weakly coupled. The weakly coupled orbital causes electron backscattering to occur, resulting in an antiresonance at the LUMO energy.

In Fig. 4.2(g), the substrate electrode is directly below a nitrogen atom and the tip electrode directly above. In this case, the transmission peak corresponding to the LUMO is

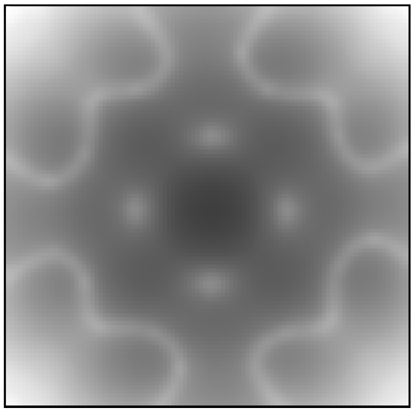

Figure 4.3: The same 16 X 16 Å current map shown in Fig. 4.2(d), with transmission plotted on a log scale. Additional delocalized features can be seen.

very narrow, and current flow comes primarily from background transmission. This background transmission corresponds mainly to the high energy transmission tails of molecular orbitals that have strong contributions from the nitrogen atoms. The current map seen in Fig. 4.2(c) is the result of contributions from these various low-energy orbitals, and from the HOMO-1 and HOMO-2, which will be analyzed in greater detail in Sec. 4.5. Transmission through the LUMO is quenched because the substrate electrode is coupled to a region of the molecule where the amplitude of the LUMO is close to zero. Thus, the overall current map is weak compared to Fig. 4.2(b).

In Fig. 4.2(h), the substrate electrode is directly below the center of the molecule and the tip electrode directly above. For this case, the transmission curve contains no LUMO-related transmission peak, since the LUMO is an antisymmetric orbital and has a node at the center of the molecule. Instead, a transmission background is seen that rises smoothly with energy. This transmission corresponds to the tail of a higher-energy π-like orbital composed primarily of zinc, with additional, less-significant contributions from other atoms. The current map of Fig. 4.2(d), plotted on a log scale, is shown in Fig. 4.3, and reveals additional structure of this orbital. Transmission through this orbital has delocalized features not evident in Fig. 4.2(d), such as nodes of low transmission when the tip electrode is above a nitrogen atom, as well as regions of higher transmission when the tip electrode is above the outer sections of the molecule. In Fig. 4.2(h), the electrodes are both coupled strongly to this orbital, so the orbital hybridizes with the electrodes and creates a transmission peak with a very long tail. Compared to this tail, transmission via the LUMO (which has very low zinc content) is negligible.

4.5 HOMO-mediated transmission

Next, electron transmission at energies close to the HOMO is considered. For the purposes of analyzing HOMO-mediated transmission, the electrodes are considered to have a zero-bias Fermi energy of -11.4 eV, which is closer to the HOMO than the LUMO. V_{bias} is again set to 1.0 V, and the same four cases of substrate electrode position are considered as for transmission at LUMO energies.

The HOMO of Zn-etioporphyrin is a non-degenerate π-like orbital with 4-fold symmetry and an energy of -11.5 eV. (See Appendix B for a 3-dimensional representation of the HOMO.) The primary atomic contributions to this orbital are from carbon atoms in the 4 pyrrole-like rings, with weak contributions from the ethyl groups and negligible contributions from all of the other inner atoms. In the energy window under consideration (-10.9 eV to -11.9 eV), there exists another π-like orbital (HOMO-1), also 4-fold symmetric and with an energy of -11.8 eV. Unlike the HOMO, this orbital has large contributions from the inner corner carbon atoms (see Fig. 4.1, above position B, and symmetric equivalents). It also has significant contributions from the nitrogen atoms, as well as non-negligible contributions from the zinc center and the 4 ethyl groups. In this energy range, there is also a σ-like orbital (HOMO-2) at an energy of -11.9 eV, with strong contributions from the nitrogen atoms.

Current maps for this energy range are shown in Fig. 4.4(a)-4.4(d), corresponding to the same substrate electrode positions as in Fig. 4.2(a)-4.2(d). In the case where the substrate electrode is directly below an ethyl group (Fig. 4.4(a)), a complex current map is obtained. In particular, low-transmission nodes exist every 45 degrees.

To understand the source of these nodes, T(E) is shown (see Fig. 4.4(e)) for two different tip electrode positions that are very close to each other, one being directly on a node (the red dot in Fig. 4.4(a)) and the other a small distance away but in a region of higher transmission (the black dot). Note that T(E) is shown, in this case only, in the narrower en-

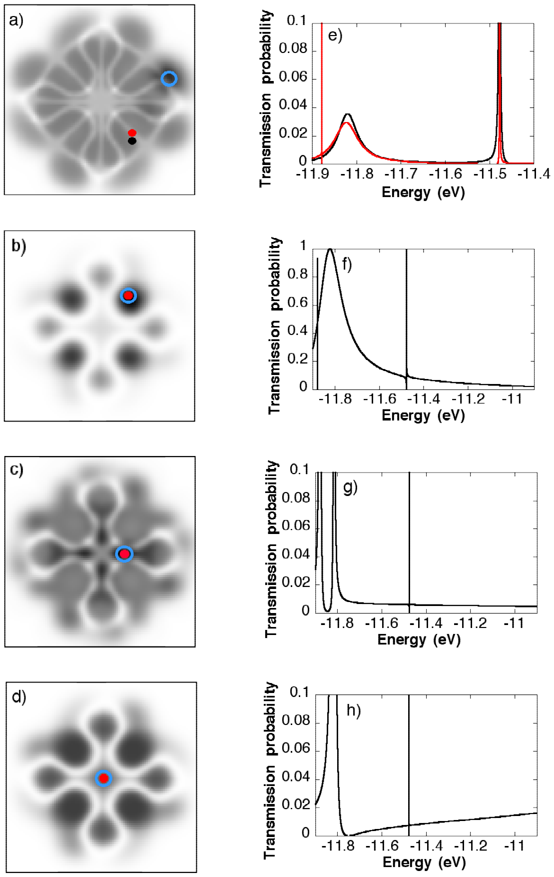

Figure 4.4: Current maps and transmission at HOMO energies. (a)-(d) 16 X 16 Å constant-height current maps, for four different substrate electrode positions. As in Fig. 4.2, the blue circles represent the position of the substrate electrode below the molecule. Again, they correspond to the blue circles in Fig. 4.1: (a) circle A, (b) circle B, (c) circle C, (d) circle D. The relative strengths of currents in the darkest regions of (a), (b), (c), and (d) are: 1 (a) : 20 (b) : 1 (c) : 4 (d). The red dots represent the tip electrode positions for the corresponding T(E) curves shown in (e)-(h), respectively. An additional black dot just below the red dot in (a) represents a different tip electrode position, yielding a second T(E) curve in (e). (e) T(E) for the substrate electrode directly below an outer ethyl group, and the tip electrode on a low transmission node [red curve, red dot in (a)], or close to this node [black curve, black dot in (a)]. The narrow transmission peak near -11.9 eV exists for both curves (the black curve is under the red curve). Note that the energy scale is different from the scale for (f)-(h). (f) T(E) for the tip and substrate electrodes above and below an inner corner carbon atom. (g) T(E) for tip and substrate electrodes above and below a nitrogen atom. (h) T(E) for tip and substrate electrodes above and below the central zinc atom. In all cases, each electrode is 2.5 Å away from the nearest atom in the molecule.

ergy range of -11.9 eV to -11.4 eV. (No transmission peaks are present in the energy range from -11.4 eV to -10.9 eV.) We see that transmission through the HOMO (near -11.5 eV) is extremely quenched (the transmission peak narrows) when the tip electrode is above the node, but transmission through the HOMO-1 is relatively unaffected. (The very narrow -11.88 eV transmission peak corresponding to the σ-like HOMO-2 orbital has a negligible effect on overall current flow.) This quenching of transmission through the HOMO occurs because the tip electrode is closest to a region of the molecule where the HOMO's amplitude is nearly zero. These regions occur every 45 degrees, as shown by the nodes. The other (curved) low-transmission nodes that are seen in Fig. 4.4(a) are caused by the HOMO-1, as will become clear through analysis of Fig. 4.4(b). Since both the HOMO and HOMO-1 are coupled non-negligibly to the substrate electrode in Fig. 4.4(a), we see a current map that is affected by both of these orbitals.

In the case (Fig. 4.4(b)) when the substrate electrode is below an inner corner carbon atom (Fig. 4.1, position B), a current map that is significantly different from Fig. 4.4(a) is obtained. The low-transmission nodes every 45 degrees are not seen, and there are strong transmission peaks when the tip electrode is above one of the 4 inner corner carbon atoms. In Fig. 4.4(f), T(E) is shown for the case when the tip electrode and substrate electrode are directly above and below the same corner carbon atom. The HOMO-1 is clearly the dominant pathway for transmission through the molecule, with the HOMO and HOMO-2 producing only narrow additional transmission peaks. This is understandable, since the corner carbon atom which is closest to both the tip and substrate electrodes has a negligible contribution to the HOMO, but a large contribution to the HOMO-1. Hence, the current map seen in Fig. 4.4(b) is primarily due to (HOMO-1)-mediated transmission through the molecule. The curved low transmission nodes correspond to regions of the molecule where the amplitude of the HOMO-1 is close to 0. Similar curved low-transmission nodes are also seen in Fig. 4.4(a), illustrating that the HOMO-1 is also the source of these nodes.

In the case when the substrate electrode is below a nitrogen atom, another unique current map is obtained. In Fig. 4.4(g), T(E) is shown for the case when the tip electrode and substrate electrode are above and below the same nitrogen atom. Two transmission peaks of similar strength are seen, corresponding to the HOMO-1 and HOMO-2, as well as a very weak peak corresponding to the HOMO. This is understandable, since both the HOMO-1 and HOMO-2 have considerable nitrogen contributions, and the HOMO does not. Hence, the current map seen in Fig. 4.4(c) is due to both the HOMO-1 and HOMO-2, resulting in a unique current map.

Lastly, when the substrate electrode is below the center of the molecule (Fig. 4.4(d)), a current map looking quite similar to Fig. 4.4(b) is obtained. Unlike in the case of LUMO energies, the current map for HOMO energies is not dominated by transmission through the low-energy tail of a zinc-dominated orbital. Rather, transmission appears to be mediated mainly by the HOMO-1 orbital. This is because the HOMO-1, unlike the HOMO or LUMO, has non-negliglble contributions from the center zinc atom, that is strongly coupled to the substrate electrode in this case. In Fig. 4.4(h), T(E) is shown for the case of the tip electrode and substrate electrode being directly above and below the center of the molecule. We see a main transmission peak corresponding to the HOMO-1, as well as a background due to the tail of the higher-energy zinc-dominated orbital. This results in stronger transmission when the tip is above the center of the molecule than if the substrate electrode is only strongly coupled to the HOMO-1 and not any higher-energy zinc-dominated orbital, as occurs in Fig. 4.4(b).

All of the unique features seen in each of these four cases, for both HOMO and LUMO energy ranges, *directly arise from differences in the details of the molecule-substrate coupling* in each case. While an individual substrate electrode positioned below the molecule is an incomplete representation for the molecule-substrate interaction, this representation illustrates the importance of understanding the detailed nature of the molecule-substrate interaction when analyzing and modelling STM topographs of single molecules on substrates. Nevertheless, specific experimental results can indeed be shown to be consistent with results of the model presented, as will be discussed next.

4.6 Comparison with experiment

The model results are now compared with experimental STM data for the system of Zn(II)-etioporphyrin I adsorbed on inhomogeneous alumina covering a NiAl(110) substrate, reproduced in this thesis in Fig. 4.5.[11] These experimental results generally show four lobes above the Zn-etioporphyrin molecule, where placement of the STM tip results in high transmission. Experimentally, the relative transmission through each of the lobes is found to depend strongly on which individual molecule is being probed, due to the complex

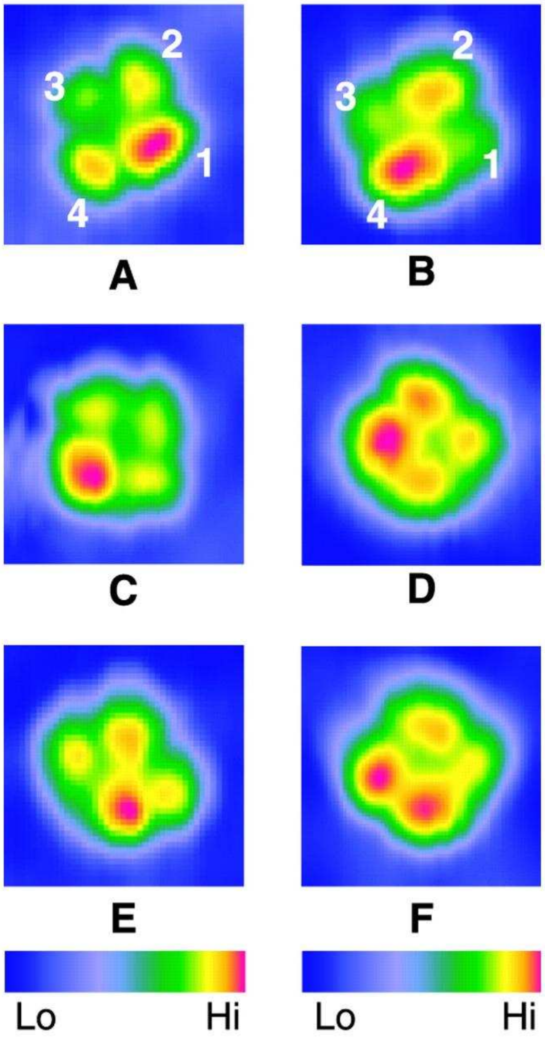

Figure 4.5: Reproduced from Qiu *et al*. (Ref. [11]). Experimental constant-current STM topographs of Zn-etioporphyrin molecules on Al_2O_3/NiAl(110). All image sizes are 32 by 32 Å. $V_{bias} = 1.0$ V and $I = 0.1$ nA. The saddle topograph shown in (B) is the most common one (approximately 30% of the molecules).

nature of the alumina-NiAl(110) substrate. Often, one or two lobes are found to have much higher transmission than the rest.

These asymmetries were originally attributed[11] to conformational differences between molecules. That is, Zn-etioporphyrin may have a number of possible geometrical configurations on the substrate. This possibility was investigated by relaxing the geometry of the molecule (as explained in Sec. 4.2) from various different geometrical starting points, with the aim of finding different stable configurations of the molecule. However, only the one stable configuration presented in this thesis was found.

Another theoretical investigation of conformational differences claims there to be two different geometrical configurations of the molecule.[67] However, the two molecular conformations are both two-fold symmetric and produce only two-fold symmetric maps. These can not explain all the various asymmetric STM topographs that are obtained experimentally. Thus, a different explanation is needed for the images of lower symmetry seen on the alumina.

An alternate explanation for the various different STM images obtained for individual molecules will now be presented. In the experiments, the molecules were likely more strongly coupled to the substrate than to the STM tip, since the molecules were adsorbed on the substrate, and the experiments were performed at a relatively low tunneling current of 0.1 nA. The STM images were obtained at positive substrate bias, therefore we may infer that the lobes represent regions of strong transmission around *LUMO energies*. The experimental results are consistent with the two-electrode model results for the situation shown in Fig. 4.2(a) (at LUMO energies, with the substrate electrode placed below one of the out-of-plane ethyl groups of the molecule), as will be explained below.

To more realistically model what one might see in an STM experiment with finite lateral resolution, the resolution of Fig. 4.2(a) should be reduced: Fig. 4.6 shows the same current map as Fig. 4.2(a), but in convolution with a gaussian weighting function of width 6Å. We see that two distinct high transmission lobes emerge, one much stronger than the other, about 11Å apart. Experimentally, the most common image seen by Qiu et al. (shown in Fig. 4.5(B)) is, after an appropriate rotation, remarkably similar to Fig. 4.6, *also containing two dominant asymmetric lobes, located* 11Å *apart*.

The other less-common STM images observed experimentally can also be explained qualitatively with this model. In an experimental situation, the underlying metal substrate may be coupled to *all four* ethyl groups at significantly differing strengths depending on the detailed local arrangement and strengths of the most conductive spots of the alumina film in the vicinity of the molecule. The result would resemble a superposition of Fig. 4.6 and current maps derived from Fig. 4.6 by rotation through 90, 180, and 270 degrees,

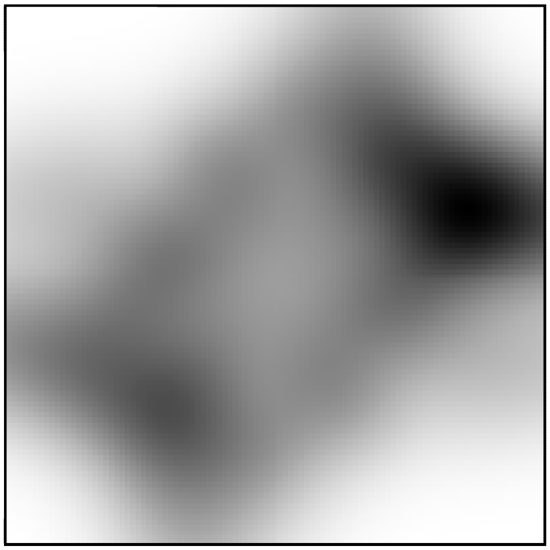

Figure 4.6: The 16 X 16 Å current map shown in Fig. 4.2(a), in convolution with a Gaussian weighting function of width 6 Å. This is done in order to more realistically simulate what one might expect to see in a real STM experiment. Two distinct asymmetric lobes are visible, and the calculated map is similar to the most common STM image observed experimentally by Qiu *et al.*,[11]) shown in Fig. 4.5(B).

with weights depending on the relative strength of the coupling of the substrate to each of the ethyl groups.[68] In this analysis, other substrate electrode positions that are the same distance from the plane of the molecule (about 4Å) but not below an ethyl group have also been considered. It was found that other substrate electrode positions yielded much weaker current flow through the molecule. Thus, these positions can be neglected in a first approximation, and current flow can be assumed to be dominated by pathways through the four substrate electrode positions below the ethyl groups. All of the different current map results obtained experimentally can be reproduced in this way reasonably well, given the simplicity of the model and the fact that the model results are for constant-height calculations whereas experimentally, constant-current STM images are obtained.

One final consideration is that in an experimental situation, the out-of-plane ethyl groups of the Zn-etioporphyrin molecule may possibly point *away* from the substrate, contrary to what has been assumed thus far. Thus, this case is now considered. Fig. 4.7 shows current

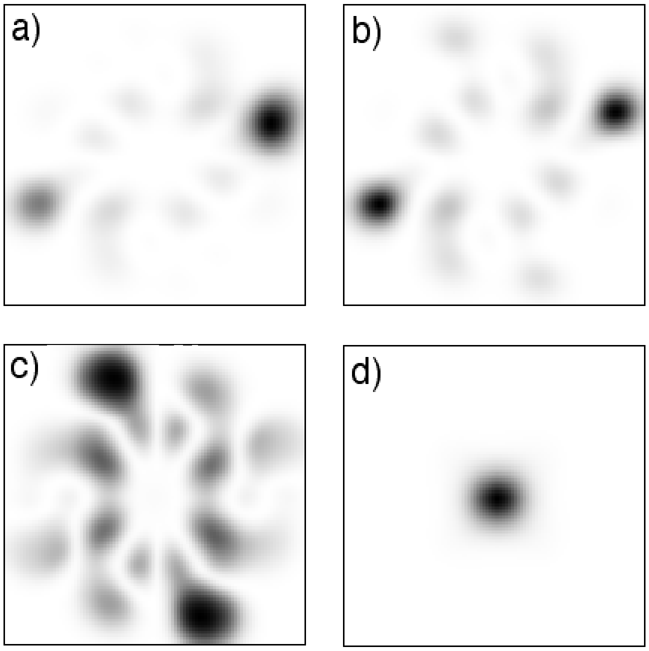

Figure 4.7: Transmission at LUMO energies, assuming ethyl groups point *away* from the substrate electrode. (a)-(d) 16X 16 Å current maps for the four different substrate electrode positions shown in Fig. 4.1: (a) circle A, (b) circle B, (c) circle C, (d) circle D. The substrate electrode is in all cases 2.5 Å below the plane of the molecule, and the tip electrode is 4.0 Å above the plane of the molecule.

maps that correspond to the four substrate electrode positions shown in Fig. 4.1, assuming the ethyl groups point *away* from the substrate electrode. The substrate electrode is positioned 2.5 Å below the plane of the molecule, and the tip electrode scans the molecule at a constant height of 4Å above the plane. In the case of Fig. 4.7(a), two asymmetric lobes corresponding to the out-of-plane ethyl groups dominate the map, one about double the strength of the other. In Fig. 4.7(b,c), two symmetric ethyl-based lobes dominate the maps, with strengths similar to the strength of the weaker lobe of Fig. 4.7(a). In Fig. 4.7(d), however, current flows primarily through the center of the molecule, again with a strength similar to that of the weaker lobe of 4.7(a). Thus, we see that most substrate electrode positions (other than below the center of the molecule) produce current maps with high-transmission lobes corresponding to the locations of the ethyl groups, with the strongest current map, obtained when the substrate probe is below an ethyl group, producing asymmetric lobes. Therefore, with the assumption that the ethyl groups of the molecule point away from the substrate, the different current map results obtained experimentally, showing four asymmetric lobes, can clearly still be reproduced within the model.

4.7 Conclusions

In this chapter, results were presented from the theoretical model of scanning tunneling microscopy in which a molecule is contacted with two local electrodes, one representing the STM tip and the other the substrate. The system analyzed is an intriguing, experimentally accessible system consisting of STM/Zn-etioporphyrin/Al_2O_3/NiAl(110), in which conclusive evidence of molecular electroluminescence has also been obtained.

The ‘two local electrodes’ approach to scanning tunneling microscopy that was presented is the simplest model of STM of large molecules separated from conducting substrates by thin insulating films, where the dominant conducting pathway through the insulating film is localized to a region smaller than the molecule. The model is well suited to this kind of system, because the molecule/substrate junction geometry is poorly understood and likely varies depending on the individual molecule being probed. By implementing the model for this system, the interplay between the tip/molecule interaction and the molecule/substrate interaction may be studied, and a better understanding of the molecular system may be obtained.

In recent experiments on the Zn-etioporphyrin system,[11] very different topographic maps were obtained for molecules at different locations on the substrate. The model has shown that differences in the details of the molecule-substrate interaction due to the non-uniform transmission of electrons through the alumina layer can account for the differences in topographic maps of these molecules. The model results presented in this thesis suggest that the out-of-plane ethyl groups of the molecule may be the location of dominant molecule-electrode coupling, and different-looking STM topographs may be the result of differing coupling strengths of the ethyl groups to the substrate.

In Chapters 5 and 6, the focus shifts to molecular electroluminescence. Building on the conclusions of this chapter (as well as those of Chapter 2), and again using a ‘local electrode’ approach, the aim will be to gain a better understanding of molecular electroluminescence, by studying the relationship between electroluminescence data and traditional STM current-voltage measurements in a single coherent framework.

Chapter 5

A local-electrode approach to single molecule electroluminescence and scanning tunneling microscopy

5.1 Introduction

In the past 15 years, molecular electronics has become a field of intense interest for fundamental research with potential applications in the creation of nanoscopic devices. At the same time, great progress has been made in the creation of nanoscale photonic devices such as those based on photonic band-gap materials.

The scanning tunneling microscope is proving immensely useful in bridging the gap between these two fields. Systems with a STM tip over a metallic or semiconducting surface are known to give off light due to the decay of plasmons. Enhanced photon emission has been observed when molecules are placed inside the tip-substrate junction. Recently, it has become clear that electric-current flow through a molecule may indeed cause the molecule to luminesce [11, 12] due to molecular-orbital electronic transitions, as discussed in Chapter 1. This phenomenon, bridging the areas of photonics and molecular electronics, is a promising step toward an emerging field of single-molecule photonics.

It has been predicted[13] (as discussed in Sec. 2.5.2) and confirmed experimentally[12] that the *relative* coupling strengths of the molecule to the electron source and drain greatly affect molecular electroluminescence. If the coupling strengths are highly asymmetric, photon emission is severely quenched. Thus, in STM/molecule/substrate experiments where the tip-molecule coupling is normally weak, a thin insulating ‘spacer’ layer between the molecule and metallic substrate can enhance photon emission by reducing the strength of the molecule-substrate coupling, making it comparable with the tip-molecule coupling.

As shown in Chapters 3 and 4, in order to theoretically model systems such as these, where there is a thin insulating spacer layer that has a complex atomic structure and a local geometry under the molecule that is not measured experimentally but transmits electrons nonuniformly, a local-electrode approach has proved useful.[58] It has been shown, for the system of STM/Zn-etioporphyrin/Al_2O_3/NiAl(110), that the location-dependent STM images of the molecules can be explained in terms of different locations of dominant molecule-substrate coupling. In Sec. 4.6 of this thesis, evidence was presented that the out-of-plane ethyl groups of the molecule may be the locations of dominant molecule-substrate coupling, and that the *strength* of the coupling between each ethyl group of the molecule and the substrate depends on the location of these groups on the substrate.[58] Thus, these couplings differ from molecule to molecule adsorbed on the substrate.

This chapter extends the theoretical approaches described in Chapters 2 and 3 in order to provide a coherent framework for understanding single molecule electroluminescence in the context of traditional scanning tunneling microscopy. A general ‘multiple local electrodes’ approach is presented. In Chapter 6, results using this framework will be presented for Zn-etioporphyrin, with four substrate electrodes representing the coupling of the four ethyl groups of the molecule to the substrate.[69]

5.2 A ‘multiple local electrodes’ approach to modelling

The model presented in this chapter is a generalization of the simpler models presented in Chapter 2 and Chapter 3 of this thesis. In the present model,[69] the tip and substrate are represented by a tip electrode (probe) and substrate electrodes (contacts) each modeled as one-dimensional tight-binding chains. Unlike in Chapters 2 and 3 where the formalism only allows single substrate electrodes, in the formalism presented here an arbitrary number of substrate contacts are allowed.

The electronic model Hamiltonian can again be divided into three parts, $H = H_{electrodes} +$

$H_{molecule} + W$, where W is the interaction Hamiltonian between the electrodes and the molecule. Generalizing the Hamiltonian of Sec. 3.3.1 to allow multiple substrate contacts, the Hamiltonian for the electrodes is given by

$$\begin{aligned} H_{\text{electrodes}} = & \sum_{n=-\infty}^{-1} \varepsilon|n\rangle\langle n| + \beta(|n\rangle\langle n-1| + |n-1\rangle\langle n|) \\ & + \sum_{i=1}^{m}\sum_{n=1}^{\infty} \varepsilon|n,i\rangle\langle n,i| + \beta(|n,i\rangle\langle n+1,i| + |n+1,i\rangle\langle n,i|), \end{aligned} \tag{5.1}$$

where ε are the site energies for the electrodes,[70] β is the hopping amplitude between nearest-neighbour electrode atoms, and $|n\rangle$ and $|n,i\rangle$ represent orbitals at site n of the tip probe and site n of the ith substrate contact, respectively. The electrochemical potentials of the tip and substrate electrodes are again taken to be $\mu_T = E_F = eV_{bias}/2$ and $\mu_S = E_F - eV_{bias}/2$.

The Hamiltonian of the molecule may be expressed as

$$H_{\text{molecule}} = \sum_j \varepsilon_j |\phi_j\rangle\langle\phi_j|, \tag{5.2}$$

where ε_j is the energy of the jth molecular orbital ($|\phi_j\rangle$). However, the model presented in this chapter is more sophisticated than the model presented in Chapter 3: in order to realistically model electroluminescence, it is necessary that molecular-orbital energies are allowed to shift in response to applied bias voltage. This is because, rather than generating only STM topographs at a single STM tip bias voltage, this model aims to explore the relationship of electroluminescence to current-voltage characteristics, a relationship that depends substantially on the detailed bias-dependent energetics of the molecule. The treatment of the effect of bias voltage on orbital energies is described in Sec. 6.3.

Generalizing Eq. 3.3 to multiple substrate contacts, the interaction Hamiltonian between the electrodes and molecule is given by

$$W = \sum_j (W_{-1,j}|-1\rangle\langle\phi_j| + W_{j,-1}|\phi_j\rangle\langle -1| + \sum_{i=1}^{m}[W_{j,(1,i)}|\phi_j\rangle\langle 1,i| + W_{(1,i),j}|1,i\rangle\langle\phi_j|]), \tag{5.3}$$

where $W_{-1,j}$, $W_{j,-1}$, $W_{j,(1,i)}$, and $W_{(1,i),j}$ are the hopping amplitude matrix elements between the electrodes and the various various molecular orbitals $|\phi_j\rangle$.

Similarly to Eq. 3.4, wave functions for electrons incoming from the tip probe are of the form

$$|\psi\rangle = \sum_{n=-\infty}^{-1} (e^{iknd} + re^{-iknd})|n\rangle + \sum_{i=1}^{m}\sum_{n=1}^{\infty} t_i e^{iknd}|n,i\rangle + \sum_j c_j|\phi_j\rangle \tag{5.4}$$

where d is the lattice spacing, t_i are the transmission amplitudes into the different substrate contacts, and r is the reflection amplitude back into the tip probe.

In order to solve the system, a similar approach to the Lippmann-Schwinger formalism described in Sec. 3.3.1 is used. This time however, since there are multiple substrate contacts involved, the transmission probability does not take on as simple a form as seen in Eq. 3.9. As before, the Green function for the decoupled system, $G_0(E)$, may be separated into the decoupled components: the tip probe, substrate contacts, and the molecule. For each electrode,

$$G_0^{\text{electrode}} = \sum_k \frac{|\phi_0(k)\rangle\langle\phi_0(k)|}{E - [\varepsilon + 2\beta cos(kd)]}. \tag{5.5}$$

$G_0^{\text{electrode}}$ may also be expressed in an atomic-orbital basis

$$G_0^{\text{electrode}} = \sum_{n=1}^{\infty}\sum_{m=1}^{\infty} (G_0^{\text{electrode}})_{n,m}|n\rangle\langle m|, \tag{5.6}$$

The matrix elements $(G_0^{\text{electrode}})_{n,m}$ (where n and m represent atomic sites on the electrodes) are known analytically.[42] For the molecule, the Green function is as before:

$$G_0^M = \sum_j \frac{|\phi_j\rangle\langle\phi_j|}{E - \varepsilon_j} = \sum_j (G_0^M)_j|\phi_j\rangle\langle\phi_j|. \tag{5.7}$$

For an electron incoming from the tip probe, this yields the following set of linear equations for the coefficients of $|\psi\rangle$:[42]

$$\psi_{-1} = (\phi_0)_{-1} + (G_0^{\text{electrode}})_{-1,-1}\sum_j W_{-1,j}c_j \tag{5.8}$$

$$\psi_{1,i} = (G_0^{\text{electrode}})_{1,1}\sum_j W_{(1,i),j}c_j \tag{5.9}$$

$$c_j = (G_0^M)_j(W_{j,-1}\psi_{-1} + W_{j,(1,i)}\psi_{1,i}) \tag{5.10}$$

where $\psi_{-1} = \langle -1|\psi\rangle$, $\psi_{1,i} = \langle 1,i|\psi\rangle$, and $(\phi_0)_{-1} = \langle -1|\phi_0\rangle$. The transmission probability for an electron incoming from the tip probe into one of the substrate contacts i is given by $T = \sum_{i=1}^{m} \frac{v'}{v}|t_i|^2$.[70] Tip-probe electrons between μ_T and μ_S in energy contribute to the electric current through the molecule. Using the Landauer theory,[18, 19] the electric current is obtained:

$$I(V) = \frac{2e}{h}\int_{\mu_S}^{\mu_T} dE\,T(E,V_{\text{bias}}). \tag{5.11}$$

The dependence of T on V_{bias} is due to shifting molecular-orbital energies (described in Sec. 6.3).

5.3 Calculating the molecular charge

In order to realistically model photon emission and electric current as a function of bias voltage, it is necessary to consider the effects of bias voltage on molecular-orbital energies. As discussed for a general molecular wire system in Sec. 2.4, when a bias voltage is applied, the energies of the molecular orbitals will be affected. For an STM system, under an applied bias an electric field is created between the tip and substrate, which may result in some charging of the molecule. If this occurs, the charging causes an electrostatic shift of the molecular energy levels that in turn severely limits the actual charging that takes place.[21] Generalizing the minimal charging approximation presented in Sec. 2.4, the shift of the molecular levels in response to the applied bias will be approximated here by adjusting ε_j for each molecular orbital so as to maintain the net charge that the molecule has at zero bias.

The net electronic charge is calculated by summing over all occupied electron states (including spin) incoming from each electrode. This sum is converted into an integral, and an expression for the charge is obtained:

$$Q = \frac{1}{2\pi}\Big(\int^{\mu_T}\sum_j \frac{|c_j(E,V_{\text{bias}})|^2}{-\beta sin(kd)}dE + \sum_{\text{contacts}}\int^{\mu_S}\sum_j \frac{|c_j(E,V_{bias})|^2}{-\beta sin(kd)}dE\Big), \tag{5.12}$$

where the molecular-orbital energies ε_j (and therefore c_j which are defined in Eq. 5.4) change with V_{bias} in such a way that Q is kept constant. In this way, the minimal charging approximation first described and presented for the simple case of a two-orbital molecule in

Sec. 2.4 may be implemented for a more complex molecule: the dependence of the molecular energy levels on the applied bias is calculated by a self-consistent procedure based on the assumption that the net charge on the molecule does not change significantly as the bias applied between the STM tip and substrate is varied in the range of bias voltages being considered. This assumption is known to be appropriate for molecules weakly coupled to the electrodes, for example in the Coulomb blockade regime. In Sec. 6.3, two different approaches for implementing this approximation are outlined, in treating the bias-dependent molecular orbital energies for the Zn-etioporphyrin molecule.

5.4 Photon emission

Photon emission from the molecule can be understood in terms of allowed electronic transitions from a molecular orbital to one with lower energy. As outlined in Sec. 2.3, to calculate emission spectra, the expression for the spontaneous emission rate of a system emitting photons into empty space, derived using Fermi's Golden Rule, may be used (see Eq. 2.9).

Unlike in Chapter 2, where photon emission is calculated for the idealized case of a two-orbital molecule, here photon emission is calculated for a system involving a real molecule with multiple molecular orbitals. In order to do this, emission is considered only from the molecule itself. The rate given by Eq. 2.9 is therefore approximated by

$$R(k_i, \omega) = \frac{4e^2\omega^3}{3\hbar c^3} \Big| \sum_{j,j'} |c_{j',f}|^2 |c_{j,i}|^2 |\langle \phi_{j'} | \mathbf{x} | \phi_j \rangle|^2, \tag{5.13}$$

where i and f label initial and final states. The relevant transition dipole moments $\langle \phi_{j'} | \mathbf{x} | \phi_j \rangle$ are calculated by performing an extended Hückel dipole analysis of the molecular orbitals.[72] For the Zn-etioporphyrin molecule, this results in some transitions being more likely than others, and still other transitions forbidden. This will be discussed more specifically in Sec. 6.5.1.

To calculate the emission rate as a function of photon energy, the procedure presented in Sec. 2.3 is generalized. All electron states of the system incoming from both the tip probe and *each of the substrate contacts* must be considered. Each electron state consists

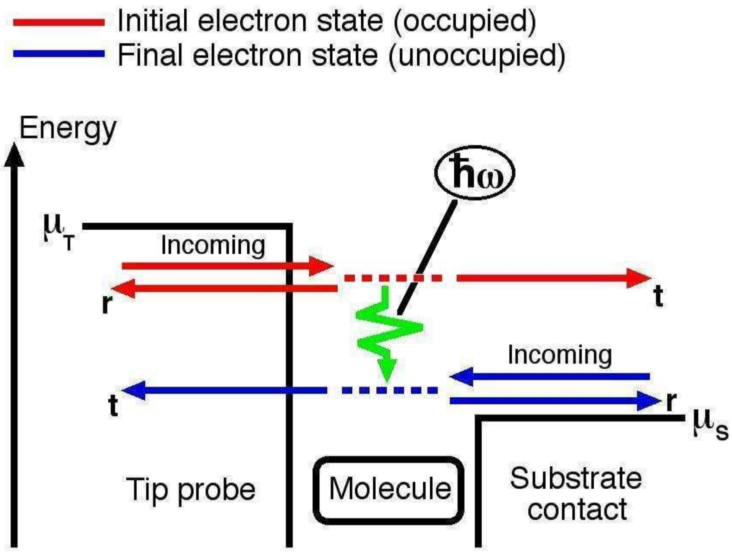

Figure 5.1: A schematic energy level diagram of a molecular wire transition in a system consisting of STM tip, molecule, and substrate.

of an incoming wave, transmitted wave, reflected wave, and an amplitude on the molecule. See Fig. 5.1 for a schematic illustration. The positive bias case ($\mu_T > \mu_S$) is assumed here.

Since the temperature is assumed to be 0 K, all states with incoming waves from a given electrode are occupied up to the electrochemical potential of that electrode. Similar to the discussion in Sec. 2.3 for photon emission from a generic molecular wire, for a transition to occur in this model, ψ_f must be an unoccupied state, and it must be lower in energy than ψ_i. Thus, when a final (delocalized) state for a transition is considered, it must be a state incoming from one of the substrate contacts, and be above the common electrochemical potential of the drain contacts.

Again, an expression for the photon emission spectrum (for a given bias voltage) is obtained, this time for multiple substrate contacts:

$$f(\omega) = \frac{1}{2\pi} \sum_{contacts} \int_{\mu_S+\hbar\omega}^{\mu_T} \frac{R(k_i,\omega)}{-\beta sin(k_i d)} dE_i. \tag{5.14}$$

The local-electrode approach to single molecule electroluminescence that is presented here, bringing together traditional STM I-V characteristics with photon emission results in a single coherent framework for the first time,[69] is implemented in Chapter 6, for the Zn-etioporphyrin molecule. A remarkable connection with experiment is achieved, in the process giving us a much better understanding of the important physics involved in such systems.

Chapter 6

Investigating the STM electroluminescence of Zn-etioporphyrin

6.1 Introduction

Building on the results of Chapters 2 and 4 of this thesis, in this culminating chapter the local-electrode theoretical framework presented in Chapter 5 is used to study, in a single coherent framework, both electroluminescence and I-V characteristics observed in the experimental system of STM/Zn-etioporphyrin/Al_2O_3/NiAl(110).

From the comparisons of STM image model results with experimental data presented in Sec. 4.6, it is likely that the regions of dominant molecule-substrate coupling are the four ethyl groups of the molecule. Therefore, in this chapter, one local STM tip probe is positioned above the molecule and four local substrate contacts positioned below the four ethyl groups of the molecule. Results for different degrees of coupling are presented and compared with experiment. It was found[69] that this model can coherently explain a wealth of previously unexplained experimental results.

There are a number of challenges dealt with in this chapter. The most fundamental challenge encountered is in how the model should treat the effect of bias voltage on the energies of the molecular orbitals, in a realistic physical way. Two different approaches to this are presented in Sec. 6.3. In Sec. 6.4, a subtle technical challenge involving the degeneracy of the LUMO is worked through and dealt with. Results are presented in Sec. 6.5

for three different substrate contact configurations representing three different categories of molecule-substrate coupling. Finally, in Sec. 6.6, the results are summarized, and a remarkable multitude of experimental observations are explained.

6.2 Electronic structure of Zn-etioporphyrin at zero bias

The electronic energy-level structure of Zn-etioporphyrin is shown in Table 4.1. In STM experiments on Zn-etioporphyrin,[11] the appearance of a low-bias dI/dV peak for some positions of the molecule above the substrate implies a Fermi level that is close to either the HOMO or LUMO. Since these are STM experiments, it is likely that the low-bias peak corresponds to an orbital entering the Fermi energy window by crossing μ_T (the electrochemical potential of the STM tip) rather than μ_S, due to the weaker coupling of the orbital to the tip than to the substrate. Since these experiments were performed at positive bias (electron flow from tip to substrate), it is therefore likely that the Fermi level is close to the LUMO and not to the HOMO.

The precise location of the Fermi level of the electrodes below the LUMO energy is likely to depend on the local geometry of the Zn-etioporphyrin/Al_2O_3/NiAl(110) interface: A work function study[71] of Al_2O_3 on NiAl(110) has found that the formation of an ultrathin Al_2O_3 layer on NiAl(110) decreases the work function of the substrate by about 0.8 eV, with a strong dependence on the oxide layer structure and thickness. It is therefore reasonable to assume that, for the experiments by Qiu, et al.,[11] different locations on the Al_2O_3/NiAl(110) substrate have different local work functions, with differences on the order of a few tenths of an eV. Due to these differences, variations in the common zero-bias Fermi energy of the tip and substrate (relative to the vacuum and also to the energies of the molecular orbitals) are likely to occur. For a qualitatively reasonable analysis of this system, a zero-bias Fermi level of -10.1 eV is chosen. This reasoning is justified more explicitly in Sec. 6.5.3 (Dependence on the zero-bias Fermi level), where results for this Fermi level are compared with results obtained assuming a zero-bias Fermi level of -10.3 eV.

6.3 Molecular orbital energy-level dependences

In order to realistically model a system such as the experimental system of STM tip/Zn-etioporphyrin/Al_2O_3/NiAl(110), the effects of bias voltage on molecular-orbital energies must be considered. As discussed in Sec. 5.3, a ‘minimal charging assumption’ may be implemented as a realistic constraint on the energies of the molecular orbitals, so that the molecule maintains the net charge that it has at zero bias.

There is still, however, the question of the detailed dependences of the individual molecular orbitals. That is, in what ways do the energies of each of the individual molecular orbitals change such that the molecule remains at its zero-bias charge? Two approaches to answering this question are studied in the remainder of this section:

6.3.1 Approach A

One approach to treating the bias dependence of molecular-orbital energies ε_j (which will be called Approach A) is to assume an *equal bias dependence for the shifts in energy of each molecular orbital*. This simple approach to charging was found to yield physically reasonable behaviour of the molecular-orbital energy levels with bias. However, by itself, it is insufficient to explain many of the experimentally observed STM I-V characteristics and photon-emission results for Zn-etioporphyrin on Al_2O_3/NiAl(110).

The reason for this may be due to Zn-etioporphyrin having a *twofold-degenerate LUMO* that is likely to lose its degeneracy when the molecule is placed on a region of the complex surface where the molecule-substrate interaction is not fourfold symmetric. See Fig. 6.1 for a rough picture of the regions of significance for each LUMO. (See Appendix B for a 3-dimensional representation of each LUMO.) It is likely that, for cases of non-fourfold symmetric molecule-substrate coupling, a splitting in the zero-bias electronic structure of the LUMO occurs. After including such a substrate-dependent splitting, this approach yields interesting results that are consistent with the experimental data.

6.3.2 Approach B

Another approach (Approach B) is to consider the bias dependence of the different orbital energies in a slightly more complex way. Since Zn-etioporphyrin is a planar molecule and

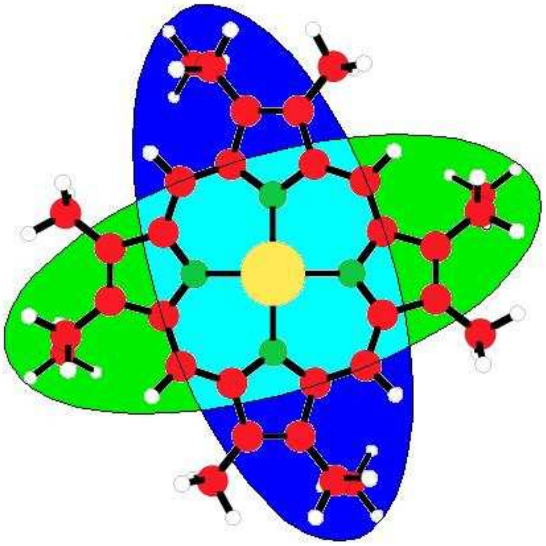

Figure 6.1: A broad sketch of each degenerate LUMO of Zn-etioporphyrin. The dominant region of one degenerate LUMO is shown in green, and the dominant region of the other LUMO is shown in blue. In the middle of the molecule, both LUMOs are significant. See Appendix B for a 3-dimensional representation of each LUMO.

all of the relevant orbitals except for the LUMO have fourfold symmetry, the electric field from the STM tip affects each of the fourfold-symmetric orbitals similarly, and we adjust their energies by equal amounts of α. The LUMO, however, consists of two degenerate orbitals with twofold symmetry. Depending on the position of the STM tip above the molecule as bias voltage is applied, this may result in a stronger electric-field effect on the energy of one of the LUMO orbitals and a weaker effect on the other orbital: see Fig. 6.2 for a rough schematic diagram showing lines of equipotential in a tip/metal system. Different parts of the molecule will ‘feel’ the potential differently.

Therefore, for cases where the tip probe is positioned above a region of the molecule with a high amplitude for one LUMO and a low amplitude for the other, instead of adjusting the LUMO energies by equal amounts of α, the LUMO energies are adjusted by amounts of γ_1 ($> \alpha$) and γ_2 ($< \alpha$), respectively. These quantities all change with V_{bias} such that the total molecular charge Q remains constant.

These quantities depend on the electrostatic geometry of the system. Therefore, for all

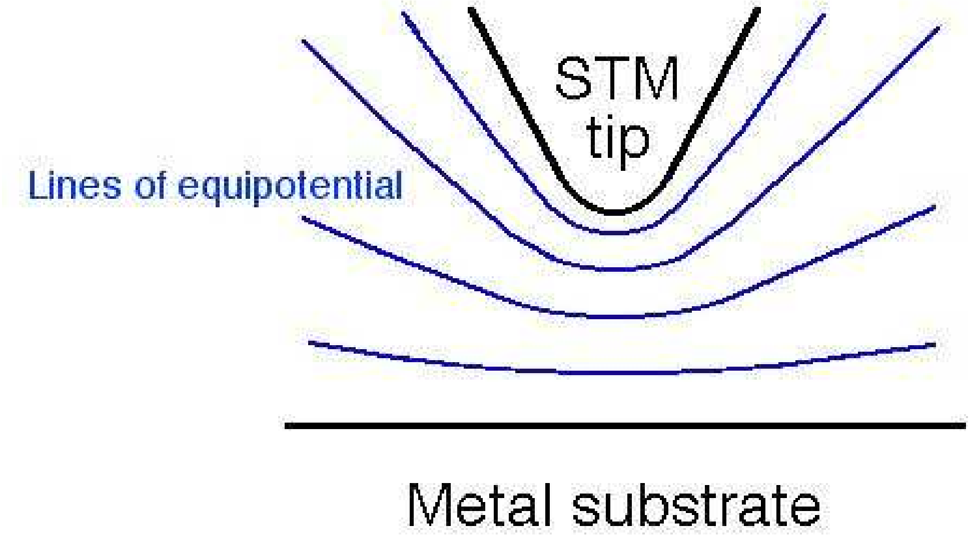

Figure 6.2: A rough schematic diagram showing the lines of equipotential for a system composed of an STM tip and metallic substrate. Notice that different regions of a horizontally-placed molecule placed between the STM tip and the metal substrate will be affected by the potential differently.

values of V_{bias}, the ratios $\alpha : \gamma_1 : \gamma_2$ are kept the same. This is consistent with the linearity of electrostatics: In an electrostatic system, Laplace's equation $\nabla^2\phi = 0$, remains satisfied if the potential throughout the system changes by a numerical factor b: $\nabla^2(b\phi) = 0$.

With this phenomenological approach to charging, unlike in Approach A, no zero-bias splitting of the LUMO degeneracy is assumed.

It is likely, to some extent, that a combination of both approaches would most accurately describe the experimental system. However, it is unknown which approach *more closely* reflects the experimental reality. In the Results section of this chapter (Sec. 6.5), both results obtained using Approach A, and results obtained with Approach B are presented, and are compared to each other and to experiment.

6.4 The molecular orbital energy shifting problem

To shift the energies of the molecular orbitals, and particularly the degenerate LUMOs of the isolated molecule, presents a technical problem, because of the use of the *extended molecule* for calculations (see Sec. 3.3.2). One can not simply shift the energies of the 'molecular orbitals' that are calculated within the extended molecular framwework. These orbitals include one atom from each electrode in addition to the molecular components, and are thus not physical molecular orbitals but rather mathematical constructions to help in the ease of calculations.

To shift the energies of the *actual* molecule in a physically reasonable way, the following procedure is followed:

Let $|m\rangle$ represent a molecular orbital of the actual isolated molecule (not including extended molecule's electrode atoms). This molecule will be referred to throughout as the *isolated molecule* as opposed to the *extended molecule*. $|m\rangle$ may be represented as a linear combination of atomic orbitals inside the isolated molecule,

$$|m\rangle = \sum_i c_{m,i}|i\rangle. \tag{6.1}$$

Here $|i\rangle$ represents an atomic orbital of the isolated molecule. The coefficients $c_{m,i}$ may be found by solving the Hamiltonian matrix problem for the isolated molecule:

$$\langle m|H_{\text{iso}}|m\rangle = E_m, \tag{6.2}$$

where the atomic orbital coefficients $H_{\text{iso}}(i,i') = \langle i|H_{\text{iso}}|i'\rangle$ of the Hamiltonian are known. One may readily solve this matrix problem for the eigenvectors $|m\rangle$ as well as the eigenvalues E_m (molecular orbital energies) using Fortran, by calling the appropriate LAPACK routine. In this case, the routine DSYGV was called.

Having obtained the isolated molecular orbital energies, they may now be shifted: $E_m \rightarrow E'_m$ according to the prescriptions for Approach A and Approach B described in Sec. 6.3.

Now, the *extended molecule* Hamiltonian is re-constructed, taking into account the shifted isolated molecular orbital energies. To do this, the Hamiltonian is split into two parts: $H = H_{iso} + H_{ext}$, where H_{ext} includes all the terms not included in H_{iso}. The Hamiltonian matrix elements may then be written as

$$\langle i|H|i'\rangle = \langle i|H_{iso}|i'\rangle \tag{6.3}$$

when both $|i\rangle$ and $|i'$ are atomic orbitals inside the isolated molecule; otherwise,

$$\langle i|H|i'\rangle = \langle i|H_{ext}|i'\rangle. \tag{6.4}$$

The term $\langle i|H_{iso}|i'\rangle$ in Eq. 6.3 is calculated using the newly shifted *molecular* orbital energies $E_{m'}$:

$$\langle i|H_{iso}|i'\rangle = \sum_m \langle i|m\rangle E'_m \langle m|i'\rangle, \tag{6.5}$$

where, applying Eq. 6.1, $\langle i|m\rangle$ may be written as

$$\langle i|m\rangle = \sum_{i'} c_{m,i'} \langle i|i'\rangle = \sum_{i'} c_{m,i'} S_{i,i'}. \tag{6.6}$$

Here $S_{i,i'}$ is the overlap term between atomic orbitals $|i\rangle$ and $|i'\rangle$.

Matrix elements for the extended part of the Hamiltonian, $\langle i|H_{ext}|i'\rangle$ of Eq. 6.4, must be further defined, depending on whether *both* or *only one* of the atomic orbitals in the matrix is outside the isolated molecular region. For the case of both atomic orbitals being outside the isolated molecular region, the matrix elements are the same as originally. (They are unaffected by energy shifts inside the molecule.) Therefore, $\langle i|H_{ext}|i'\rangle = \langle i|H|i'\rangle$, where H is the original Hamiltonian. For the case where one atomic orbital, $|i\rangle$, is inside the isolated molecular region and one, $|i'\rangle$, is outside, the Hamiltonian matrix element may be approximately determined through applying the Wolfsberg-Helmholz equation (see Eq. 3.12):

$$H_{i,i'} = \frac{1.75 S_{i,i'}}{2} (\langle i|H_{iso}|i\rangle + \langle i'|H|i'\rangle), \tag{6.7}$$

where $\langle i|H_{iso}|i\rangle$ is calculated as in Eq. 6.5.

Knowing all of the matrix elements of the shifted Hamiltonian, the total molecular charge at a given bias is computed (see Sec. 5.3). If the charge is computed to be lower than the zero-bias charge, the orbitals are shifted downward in energy, and the calculation is performed again. If the total charge is computed to be higher than the zero-bias charge,

Orbital	HOMO-2	HOMO-1	HOMO	LUMO1	LUMO2	LUMO+1
HOMO-2	-	0	0	0	0	0
HOMO-1		-	0	0.799	0.799	0
HOMO			-	0.872	0.872	0
LUMO1				-	0	0.511
LUMO2					-	0.511
LUMO+1						-

Table 6.1: Transition dipole moments between relevant molecular orbitals of the molecule Zn(II)-etioporphyrin I.

the orbitals are shifted upwards in energy. This procedure is continued until the charge on the molecule falls within an acceptable threshold close to the zero-bias charge. In this way, the energies of the molecular orbitals at a given bias are determined self-consistently under the assumption of minimal charging of the molecule.

6.5 Results

Results are presented for the Zn(II)-etioporphyrin I molecule, coupled to a tip probe and four substrate contacts that are represented for simplicity by Cu *s* orbitals. The same geometrical structure is used as is calculated for Chapter 4 (see Appendix A).

6.5.1 Molecular orbital transition dipole moments

In order to calculate molecular electroluminescence, it is necessary to first calculate the transition dipole moments (oscillator strengths) for the relevant orbitals, $\langle\phi_{j'}|\mathbf{x}|\phi_j\rangle$ (see Eq. 5.13). This calculation is performed with the help of the ICON-EDiT program[72], that calculates oscillator strengths for molecular orbitals in an extended Hückel framework. Table 6.1 shows the transition dipole moments for the relevant orbitals.

6.5.2 Strong fourfold-symmetric molecule-substrate coupling

The first case considered is a case where there is strong electronic molecule-substrate coupling and where the molecule-substrate interaction is fourfold symmetric. By ‘strong cou-

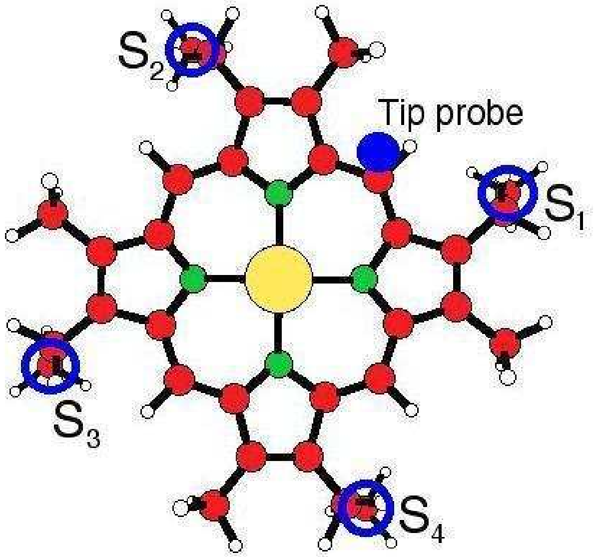

Figure 6.3: The Zn(II)-etioporphyrin I molecule showing substrate contacts S_1, S_2, S_3, and S_4 (open blue circles, into the page) and the tip probe (blue dot, out of page). Carbon atoms are red, nitrogen atoms are green, the zinc atom is yellow, and hydrogen atoms are white.

pling' what is meant is that the Hamiltonian matrix elements $W_{\mathrm{electrode},j}$ between the relevant molecular orbitals and substrate contacts are about an order of magnitude greater than between the molecular orbitals and tip probe.

In Sec. 4.6, it was shown that the out-of-plane ethyl groups of Zn-etioporphyrin are likely locations of dominant molecule-substrate coupling.[58] Therefore, four local substrate contacts (S1-S4) are positioned below the ethyl groups of the molecule, as shown in Fig. 6.3.[73] For Approach A (described in Sec. 6.3.1, in this case it is assumed that there is *no splitting* of the LUMO degeneracy. *This is consistent with the fourfold symmetry of the molecule-substrate coupling in this case.* The tip probe is positioned (see Fig. 6.3) above the molecule in a lateral region that has been shown to be part of the observed high-transmission lobe pattern for the STM tip above Zn-etioporphyrin.[11, 58]

For this position of the tip probe (and any position corresponding to an experimentally observed high-transmission lobe) the tip probe has a stronger *electrostatic* coupling to one of the degenerate twofold symmetric LUMOs than to the other, and an intermediate coupling to all other relevant orbitals. [The difference between electrostatic and electronic coupling should be noted: *Electrostatic coupling* refers to the change in the electrostatic potential that an electron in a molecular orbital feels due to the applied bias voltage, whereas *electronic coupling* refers to the Hamiltonian matrix element $W_{\text{electrode},j}$ between an electrode and a molecular orbital. In the rest of this chapter, these terms will be frequently used.] Therefore, for Approach B (discussed in Sec. 6.3.2), in order to model the shift of molecular orbital energies due to electrostatic effects in a phenomenological, qualitatively reasonable way, the ratio $\alpha : \gamma_1 : \gamma_2$ (discussed in Sec. 6.3.2) is assumed to be 3:4:2. Here, γ_1 corresponds to the orbital shift of the LUMO orbital that has stronger electrostatic coupling, and γ_2 to the orbital that has weaker electrostatic coupling to the tip.

Results presented throughout this chapter are not sensitive to the precise values chosen for this ratio: Changing the ratio $\alpha : \gamma_1 : \gamma_2$ affects the energies of the relevant molecular orbitals when a bias voltage is applied, but does not qualitatively change the model results as long as the condition $\gamma_2 < \alpha < \gamma_1$ is met. For a ratio $\alpha : \gamma_1 : \gamma_2$ set to 9:10:8 instead of 3:4:2 (corresponding to smaller differences in the electrostatic effects on each orbital), all of the qualitative features described in Sec. 6.5 remain the same.

Approach A

For this strong substrate coupling case, with Approach A (discussed in Sec. 6.3.1), photon emission is computed to be very weak. (In Sec. 6.5.3 and Sec. 6.5.4, cases will be presented where the photon yield is more than an order of magnitude greater.) This weak emission result is consistent with the quenching of emission due to asymmetric coupling of the molecule to the tip and substrate predicted for the general case of current-carrying molecular wires[13] and observed experimentally[10], as discussed in Sec. 2.5.2 of this thesis. The quenching of photon emission due to asymmetry of the electronic coupling can be understood physically as follows: Looking back to Fig.5.1, in a highly asymmetric system where the tip-molecule coupling is much weaker than the molecule-substrate coupling, electrons incoming from the tip have relatively low amplitudes for entering the molecule, and high amplitudes for exiting into the substrate. There is therefore a low amplitude $c_{j,i}$ (see Eq. 5.13) for an electron in its initial state to be on a molecular orbital (even if the orbital is inside the Fermi energy window and close in energy to the energy of the electron), resulting in a low photon emission rate.

A further possible consideration is the molecular orbital amplitude $c_{j,f}$ of an electron in its final state. If no allowed molecular orbitals are available to receive transitions (ie. inside the Fermi energy window of the system), $c_{j,f}$ will be small for all possible final states and emission will be further quenched. As will be shown later in this section, for the strong fourfold-symmetric coupling situation we consider here this is in fact the case.

Results for the strong fourfold-symmetric coupling case are shown in Fig. 6.4. Fig. 6.4a shows the electric current, for Approach A, as a function of bias voltage, with the red curve showing dI/dV. Fig. 6.4c shows how the molecular orbital energies shift with bias voltage, with dashed lines μ_T and μ_S representing the electrochemical potentials of the tip and substrate electrodes respectively. Fig. 6.4b and Fig. 6.4d are results for Approach B, discussed later in this section. Photon emission is not included in Fig. 6.4, as it is found to be extremely weak.

The calculated current-voltage (I-V) curve for this case can be understood by studying how the molecular orbital energies shift with bias voltage (see Fig. 6.4c): At zero bias, the energy of the LUMO (assumed to be degenerate in this case) is slightly above μ_S and μ_T, while the HOMO is much further below. At low bias, the tip electrochemical potential μ_T rises with increasing bias towards the LUMO, causing the LUMO to become partially (slightly) occupied. This causes an electrostatic shift of the molecular orbital energies (discussed in Sec. 6.3): The LUMO and HOMO track μ_T, so that the net charge on the molecule is maintained.

An approximately linear I-V curve at low bias is seen in Fig. 6.4a, with electron flow being mediated by the tails of the HOMO and LUMO. There is a slight low-bias dI/dV feature due to μ_T approaching the LUMO energy. At about 1.3 V, the slope of the I-V curve begins to increase, resulting in a peak in dI/dV. The reason for this I-V behaviour is as follows: Electrons entering the molecule from the tip, which are inside the Fermi energy window between μ_T and μ_S, contribute to the net current. As μ_S approaches the HOMO energy, the high-energy tail of the HOMO mediates electron flow from tip to substrate, increasing the net current. It is important to also remember that the molecule-substrate contact couplings are strong compared to the tip-molecule coupling in this case, so the substrate has a much stronger effect on orbital occupations than the tip, and the high-energy tail of the HOMO begins to depopulate when the HOMO is still significantly below μ_S. The orbital energies are affected slightly, with the LUMO shifting slightly lower relative to μ_T

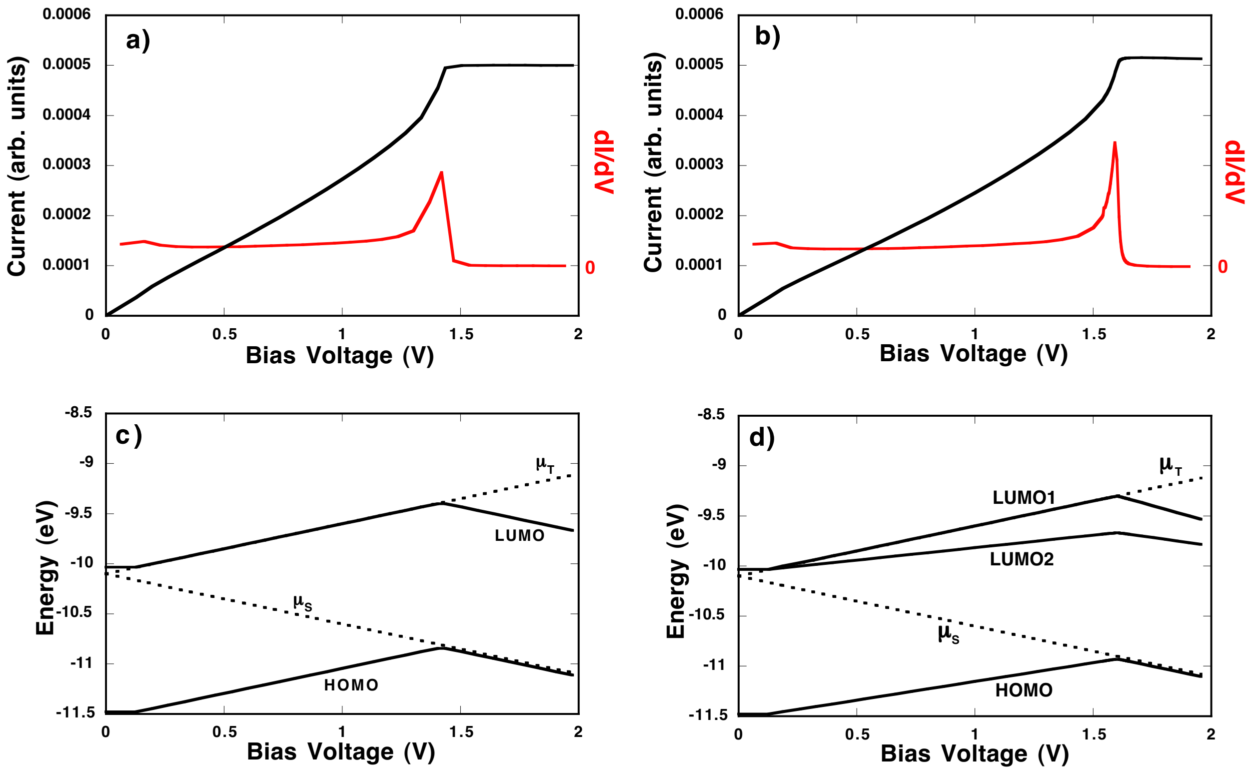

Figure 6.4: Strong fourfold-symmetric coupling between molecule and substrate: Electric current and molecular orbital energies as functions of bias voltage. (a) Approach A, I vs. V_{bias}. Red lines represent dI/dV. (b) Approach B, I vs. V_{bias}. (c) Approach A, molecular orbital energies (dashed lines represent tip and substrate electrochemical potentials). (d) Approach B, molecular orbital energies.

(but not visibly in Fig. 6.4c), such that the net charge on the molecule is maintained. The slight downward shift of the LUMO energy further increases the slope of the I-V curve. Here, electric current is very sensitive to such a shift, due to the LUMO's energy being very close to μ_T.

At about 1.4 V, the LUMO fully enters the Fermi energy window, in the process becoming only slightly occupied due to the much weaker coupling of the molecule to the tip (electron source electrode) than to the substrate (drain). At this point both the HOMO and LUMO orbital energies shift downwards, in such a way that the charge on the molecule remains constant (ie. the HOMO energy follows μ_S). The I-V curve flattens, since no orbitals are entering or approaching the energy window between tip and substrate Fermi energies to

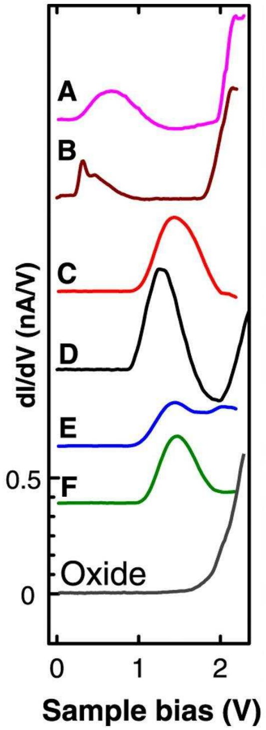

Figure 6.5: From Qiu *et al.* (Ref. [11]). Reprinted with permission from AAAS. Experimental dI/dV curves for Zn-etioporphyrin/Al_2O_3/NiAl(110) obtained with the STM for molecules at different locations on the substrate. (A-F) dI/dV curves representative of the various molecular images observed. The curve seen in B was most commonly observed (30% of the time). Molecular electroluminescence was observed for cases A and B but not for C-F.

mediate transmission.

The HOMO energy remains below μ_S, resulting in quenched photon emission, since there are only weak molecular orbital tails available to receive transitions from the LUMO, that are inside the Fermi energy window of the system.

This result is now compared with experimental results obtained by Qiu et al.[11] for the STM/Zn-etioporphyrin/Al_2O_3/NiAl(110) system. In these experiments, depending on the location of the molecule on the substrate, the molecule either luminesced or did not, with different dI/dV curves obtained for luminescent and non-luminescent cases. See Fig. 6.5 for the reproduced experimental curves. Here, curve A and curve B are representative of molecules that were found to luminesce. *Molecules with current-voltage curves C-F did not exhibit observable luminescence.* Experimentally, molecules that did not luminesce were found to have only one dI/dV peak, usually at around 1.4 V. This is in good qualitative agreement with the model result presented here, using Approach A, which shows only one significant dI/dV peak that occurs at 1.4 V in Fig. 6.4a, and very weak photon emission, that is likely not experimentally detectable.

Approach B

For the case of strong fourfold-symmetric molecule-substrate coupling, Approach B (discussed in Sec. 6.3.2) yields I-V results shown in Fig. 6.4b that are qualitatively similar to those in Fig. 6.4a that were obtained using Approach A. Photon emission is also computed to be very weak, for the same reasons as with Approach A.

With Approach B, the LUMO with the weaker electrostatic coupling to the tip (which will be referred to as LUMO2) enters the Fermi energy window at low bias (see Fig. 6.4d), but contributes very little to the electric current (see Fig. 6.4b), due to the very weak LUMO2-tip probe electronic coupling. The LUMO2 remains almost completely unoccupied because of the asymmetry of the LUMO2-tip and LUMO2-substrate couplings. As μ_T approaches the energy of the *more strongly* electrostatically and electronically coupled LUMO (LUMO1), however, the LUMO1 becomes partially (slightly) occupied and shifts in energy, following μ_T, so that the net charge on the molecule is maintained. The result is again an approximately linear I-V curve, with electron flow being mediated by the tails of the HOMO and the LUMO1.

At about 1.5 V, the HOMO begins to become partially (slightly) unoccupied, similarly to Approach A, and the slope of the I-V curve increases. The LUMO1 shifts slightly lower relative to μ_T, such that the net charge on the molecule is maintained. This further increases the slope of the I-V curve. At 1.6 V, the LUMO1 fully enters the Fermi energy window, in the process becoming only slightly occupied due to the asymmetry of the coupling. As with Approach A, the orbital energies then shift downwards, in such a way that the charge on the molecule remains constant. The HOMO energy remains below μ_S, resulting in quenched photon emission, and the I-V curve flattens.

For this case of strong molecule-substrate coupling using Approach B, there is found to be only one significant dI/dV peak (at 1.6 V) and very weak photon emission. As for Approach A, this compares well with the experimental non-luminescent cases (see Fig. 6.5C-F), where one dI/dV peak is observed (at about 1.4 V).

6.5.3 Localized strong coupling

Next, we consider the case where there is strong electronic coupling between the molecule and only *one* of the four substrate contacts. It was found,[58] as shown in Sec. 4.6, that this type of electrode configuration is a likely possibility for the common experimental case of Fig.2B in the article by Qiu et al.[11] Significant molecular electroluminesce was observed for this experimental case.

The electrode configuration that is considered is similar to Sec. 6.5.2 (see Fig. 6.3); however, in this case the substrate contacts S_1, S_2 and S_3 are moderately coupled to the molecule (coupling less than an order of magnitude greater than the coupling to the tip probe), and S_4 is strongly coupled.[74] The tip probe is positioned in the same lateral region as for Sec. 6.5.2, and again with greater electrostatic coupling to one LUMO (LUMO1) relative to the other LUMO (LUMO2). It should also be noted that, due to the geometries of the two LUMO orbitals shown in Fig. 6.1 (see Appendix B), the strongly coupled substrate contact is electronically strongly coupled to only one of the LUMOs (LUMO2, in this case) and not the other (LUMO1).

Approach A

With Approach A, since the molecule-substrate interaction is in this case not fourfold-symmetric, there is a splitting in the zero-bias degeneracy of the LUMO.[75]

For this case, significant photon emission is computed to occur. Fig. 6.6a shows the calculated emission spectrum at high bias ($V_{bias} = 1.94$ V). The spectrum corresponds to HOMO-LUMO1 (1.94 eV peak) and HOMO-LUMO2 (1.44 eV peak) transitions. The calculated I-V curve for this case, shown in Fig. 6.6c, has a low-bias dI/dV peak and a high-bias dI/dV peak.

To understand the calculated photon emission spectra and I-V curves for this case, it is necessary to pay close attention to the details of the coupling of the various molecular orbitals to the electrodes. Looking at Fig.6.6e, at low bias the LUMO2 enters the Fermi energy window, remaining almost completely unoccupied due to the strongly asymmetric

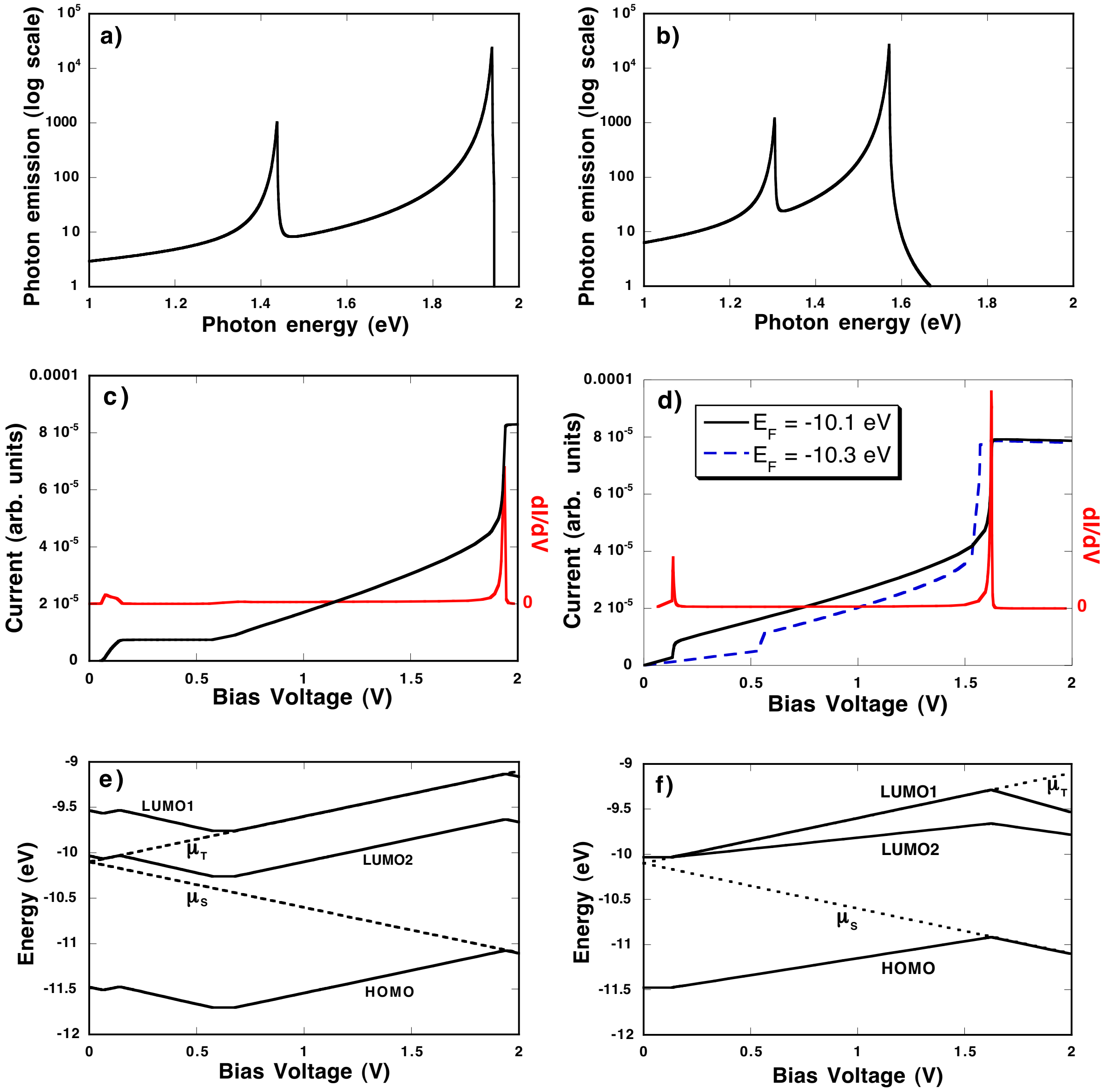

Figure 6.6: Localized strong coupling: photon emission, electric current, and molecular orbital energies as functions of bias voltage. (a) Approach A, photon emission vs. V_{bias}. (b) Approach B, photon emission vs. V_{bias}. (c) Approach A, I vs V_{bias}. Red lines represent dI/dV. (d) Approach B, I vs. V_{bias}. Dashed line represents $E_F = -10.3$ eV. (e) Approach A, molecular orbital energies. (f) Approach B, molecular orbital energies.

coupling of the LUMO2 to the tip and substrate. In this case, however, the LUMO2 contribution to the electric current is not negligible. Current flow mediated by the LUMO2 is not drowned out by current flow mediated through the tails of the LUMO1 or the HOMO, since in this case the electronic coupling of the substrate is strongest to the LUMO2. This creates the low-bias dI/dV peak seen in Fig. 6.6c.

The LUMO2 energy follows μ_T up to 0.2 V (see Fig. 6.6e). In this case, the substrate contacts have a large influence on the occupation of the LUMO2 even though the LUMO2 is well above μ_S, because the coupling between the substrate and LUMO2 is much stronger than between the tip and LUMO2. Thus, from 0.2 V to 0.6 V the LUMO2 tracks μ_S and the I-V curve (Fig. 6.6c) is flat. At 0.6 V, the LUMO1 approaches μ_T and begins to populate. In response, the energies of the orbitals rise such that no charging takes place. The tip probe has a large influence on the occupation of the LUMO1, because the coupling between the tip/substrate and LUMO1 is not highly asymmetric. From 0.6 V to 1.9 V, The LUMO1 and the tail of the HOMO are the dominant sources of rising current.

The HOMO reaches μ_S at $V_{bias} = 1.9$ V, causing an electrostatic shift in energy of the orbitals downwards, so that the LUMO1 enters the Fermi energy window and populates significantly. The HOMO reaches μ_S and depopulates by an equal amount. There is a resulting sharp increase in current, as both the HOMO and LUMO1 mediate electron transmission from tip to substrate.

Close inspection of Fig. 6.6e and Fig. 6.4c shows that, in this case, the HOMO energy comes up to μ_S (within the resolution of the figure) whereas for the case of Sec. 6.5.2 (Approach A), the HOMO energy only *approaches* μ_S. Hence, the depopulation of the HOMO is much greater in this case than in Sec. 6.5.2. Greater depopulation of the HOMO occurs, along with greater population of the LUMO1 as it enters the Fermi energy window, due to the lack of strong coupling asymmetry between the LUMO1 and the tip/substrate electrodes in this case. In this way, the zero-bias charge is maintained. Therefore, above 1.9 V, HOMO-mediated electronic states are available to receive transitions from LUMO1 and LUMO2-mediated states, resulting in photon emission. Since there is a stronger coupling asymmetry between the LUMO2 and the tip/substrate electrodes than between the LUMO1 and those electrodes, LUMO2-HOMO photon emission is weaker than LUMO1-HOMO emission (see Fig. 6.6a), as explained in Sec. 6.5.2(Approach A).

The onset of photon emission in this case occurs as the HOMO becomes partially un-

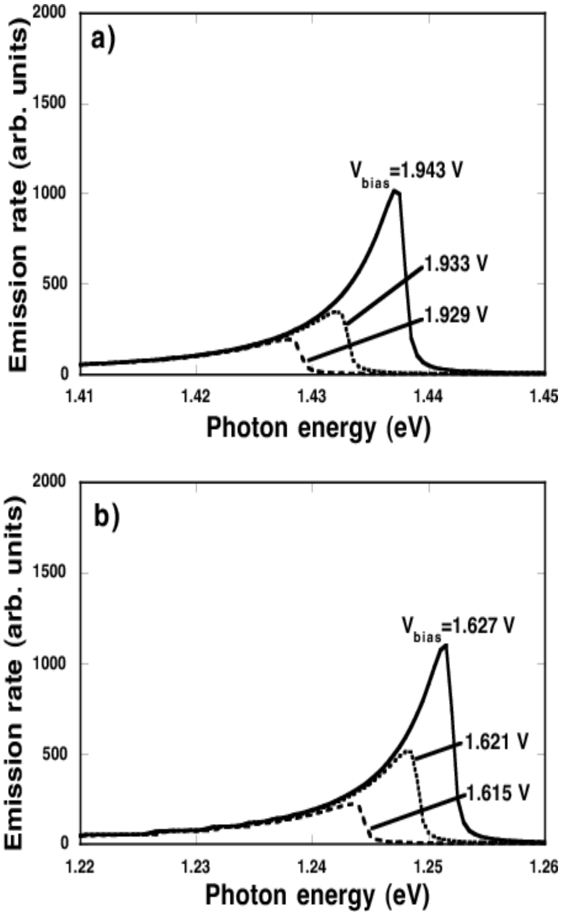

Figure 6.7: Localized strong coupling: Onset of photon emission at the HOMO-LUMO2 emission peak. (a) Approach A, emission rate vs. photon energy for three different values of V_{bias} around the onset voltage. (b) Approach B, emission rate vs. photon energy.

occupied, at about 1.9 V. Fig. 6.7a shows the onset of photon emission, at the spectrum peak corresponding to HOMO-LUMO2 transitions. Notice that the peak photon energy ($\approx$ 1.43-1.44 eV) is significantly less than the Fermi gap energy $\mu_T - \mu_S$ ($\approx$ 1.93-1.94 eV). This is because the LUMO2 is deep inside the Fermi energy window at the onset voltage (see Fig. 6.6c). The calculated photon emission peak due to HOMO-LUMO1 transitions has the same onset voltage as the HOMO-LUMO2 emission peak. For this transition, however, photon energy is peaked close to the Fermi gap energy (1.9 eV) because the LUMO1 and HOMO have energies close to μ_T and μ_S respectively at the onset voltage.

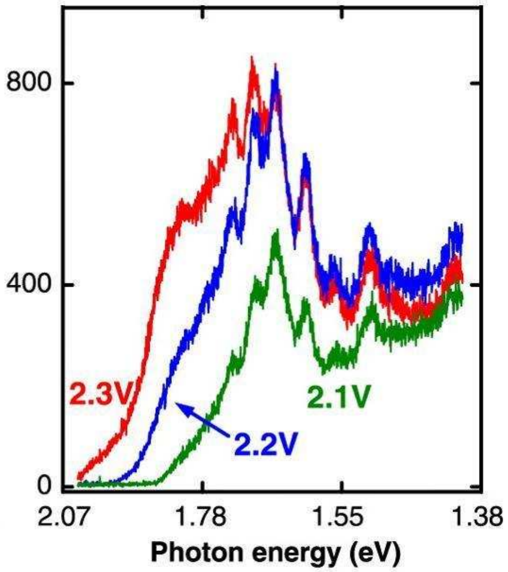

Figure 6.8: From Qiu *et al.* Reprinted with permission frm AAAS. Experimental photon emission spectra for molecules corresponding to B in Fig. 6.5 for various bias voltages around the onset voltage.

Comparing results for this luminescent case to experiment, the similarities are striking. Experimentally, molecules that luminesced commonly had a small dI/dV peak at 0.2 V and a larger peak at around 2.0 V (see Fig. 6.5A,B). This is in excellent qualitative agreement with Fig.6.6c, where a small dI/dV peak is seen at 0.2 V and a larger peak at about 1.9 V. Furthermore, experimental results[11] (reproduced here in Fig. 6.8) show the onset of photon emission occurring most commonly at about 2.2 V, but with a photon energy peak in the spectrum about 0.5 eV below the corresponding Fermi gap energy of 2.2 eV. This is in good agreement with Fig. 6.7, where at onset an emission peak (corresponding to the HOMO-LUMO2 transition) is found significantly below the Fermi gap energy. Also, we see very similar behaviour of the emission spectra tails: The high-energy tail has a sharp cutoff, while the low-energy tail does not. As bias voltage increases, the high-energy cutoff shifts upwards in energy by a similar amount. In the model results presented in this chapter, this behaviour is also seen, because the Fermi energy of the substrate provides a sharp energy cutoff below which there are no available final states for a transition. This cutoff reduces the extent of the high-energy tails of the photon spectrum. There is no such cutoff reducing the extent of the low-energy photon tails.

Notice also that, experimentally, there is a shift in the position of the high-bias dI/dV peak, depending on whether photon emission is observed: In Fig. 6.5 a peak is observed at 1.4 V for non-luminescent cases (C-F), and around 2.0 V for luminescent cases (A,B). The same sort of bias peak shift is seen theoretically with Approach A: 1.4 V for Sec. 6.5.2 (weak emission case) and 1.9 V for Sec.6.5.3 (strong emission case). In this way, Fig. 6.4a is similar to Fig. 6.5C-F, while Fig. 6.6c is similar to Fig. 6.4A,B.

The model further predicts a stronger HOMO-LUMO1 emission peak (the 1.94 eV peak in Fig. 6.6a) with the same onset voltage as the experimentally observed HOMO-LUMO2 emission peak, but with a higher peak photon energy, close to the Fermi gap energy $= eV_{bias}$. The experimental photon spectra in Ref. [11] do not extend to the photon energy range in which this emission peak is predicted to occur (2.2 eV photon energy for the experimental onset voltage of 2.2 V). An experimental study testing this prediction of the model (that a second, high energy, photon peak should occur) would be intriguing.

Approach B

With Approach B, as with Approach A, significant photon emission is computed to occur in this case of localized strong molecule-substrate coupling. Fig. 6.6b shows the emission spectrum at high bias ($V_{bias} = 1.94$ V). The spectrum corresponds to HOMO-LUMO1 (1.57 eV peak) and HOMO-LUMO2 (1.30 eV peak) transitions. The I-V curve for this case, shown in Fig. 6.6d, has a low-bias dI/dV peak and a high-bias dI/dV peak.

Looking at Fig.6.6f, at low bias the LUMO2 enters the Fermi energy window. It remains almost completely unoccupied due to the strongly asymmetric coupling of the LUMO2 to the tip and substrate, but as with Approach A it still contributes to the electric current. This results in the low-bias dI/dV peak seen in Fig. 6.6d. At 0.2 V the energy of the LUMO1 reaches μ_T. This causes an electrostatic shift in the energy levels upwards, as shown in Fig. 6.6f. From 0.2 V to 1.6 V, the LUMO1 and the tail of the HOMO are the dominant sources of rising current. The HOMO reaches μ_S at 1.6 V, causing an electrostatic shift in energy of the orbitals downwards, so that the LUMO1 enters the Fermi energy window and populates significantly. Similarly to Approach A, the HOMO reaches μ_S and depopulates by an equal amount, resulting in a sharp increase in current.

For the same reasons as were explained for Approach A, for Approach B at 1.6 V HOMO-mediated electronic states are available to receive transitions from LUMO1 and LUMO2-mediated states, resulting in photon emission. As with Approach A, LUMO2-HOMO photon emission is weaker than LUMO1-HOMO emission (see Fig. 6.6b). Fig. 6.7b shows the onset of photon emission, around $V_{bias} = 1.6$ V, at the spectrum peak corresponding to HOMO-LUMO2 transitions. As with Approach A, the photon peak energy is significantly less than the Fermi gap energy.

Qualitatively, I-V and photon emission results for Approach B are similar to results for Approach A, and compare similarly well to experiment. There is one exception: With Approach B, there is no shift in the position of the high-bias dI/dV peak depending on whether or not photon emission is observed: A peak is predicted at 1.6 V for both luminescent and non-luminescent cases, due to the very similar molecular orbital energetics for luminescent (Fig. 6.6f) and non-luminescent (Fig. 6.4d) cases. Experimentally, there is a shift in the position of the dI/dV peak: around 1.4 V for the non-luminescent case and 2.0 V for the luminescent case (see Fig. 6.5)). A similar shift is found theoretically with Approach A, due to the fact that the HOMO-LUMO1 energy difference in the luminescent case (Fig. 6.6e) is greater than the HOMO-LUMO energy difference in the non-luminescent case (Fig. 6.4c).

The physical reason for this difference between Approach A and Approach B is that in Approach A the molecule-substrate coupling splits the LUMO degeneracy in the luminescent case but not in the non-luminescent case and this difference in electronic structure results in the different bias voltages at which the high bias peak in dI/dV occurs. By contrast, in Approach B the LUMO degeneracy is lifted in both the luminescent and non-luminescent cases, so that the electronic structure of the molecule and the bias voltage at which the high bias peak in dI/dV occurs is similar in the two cases.

Dependence on the zero-bias Fermi level

Experimentally, different dI/dV curves are observed depending on the location of the molecule on the substrate (see Fig. 6.5)[11]. Even among those molecules that luminesced (A and B), there are differences in dI/dV. It should be noted that, in the model results presented here thus far, a zero-bias Fermi level of -10.1 eV was chosen, and that variations in the Fermi level relative to the molecular levels at zero bias are likely, depending on the location of the molecule on the surface, due to local work function variations (discussed in Sec. 6.2).

The dashed line in Fig. 6.6d shows an I-V curve (using Approach B) for an *alternate zero-bias value* of E_F: -10.3 eV instead of -10.1 eV. Here, the low-bias dI/dV peak is at 0.5 eV, corresponding more closely to Fig. 6.5A than Fig. 6.5B. It is possible that the experimental differences in low-bias dI/dV peak locations in Fig. 6.5A and Fig. 6.5B are due to different zero-bias Fermi levels caused by local work function variations on the surface. Other than the change in the low-bias dI/dV peak location, small changes in the Fermi level yield qualitatively similar I-V and photon emission results. Therefore, for the rest of this chapter, a Fermi level of -10.1 eV is assumed.

6.5.4 Weak fourfold-symmetric molecule-substrate coupling

The final case considered is weak molecule-substrate coupling, where the molecule-substrate interaction is fourfold-symmetric, along with stronger tip-molecule coupling than in the previous cases. In this case, the electronic molecule-substrate coupling is of the same order of magnitude as the tip-molecule coupling.[76] This situation may be achieved experimentally by increasing the thickness of the oxide layer between the molecule and metal substrate by a modest amount, or by decreasing the tip-molecule distance. For the model in this case, both the molecule-substrate distance is increased and the tip-molecule distance decreased.

Approach A

As in Sec. 6.5.2(Approach A), there is assumed to be no splitting of the LUMO degeneracy. For this case, much more efficient photon emission is predicted to occur, with a photon yield two orders of magnitude higher than for Sec. 6.5.3. Fig. 6.9a shows the emission spectrum at high bias ($V_{bias} = 1.95$ V). The peak in the spectrum corresponds to the HOMO-LUMO transition. Fig. 6.9c shows the I-V curve for this case. There is a high-bias dI/dV peak (at 1.45 V) and no low-bias peak. Looking at Fig. 6.9e, the molecular orbital energetics are similar to those for Sec. 6.5.2(Approach A) (shown in Fig. 6.4c). Since no orbitals enter the Fermi energy window at low bias, there is no low-bias dI/dV peak. In this case, the I-V curve is quite flat up to about 1.4 V. At 1.4 V, the LUMO fully enters the Fermi energy window, becoming partially occupied. The HOMO depopulates by an equal amount, and the orbitals electrostatically shift downwards in energy with μ_S.

Since the tip has a much stronger effect on the LUMO occupation in this case than in

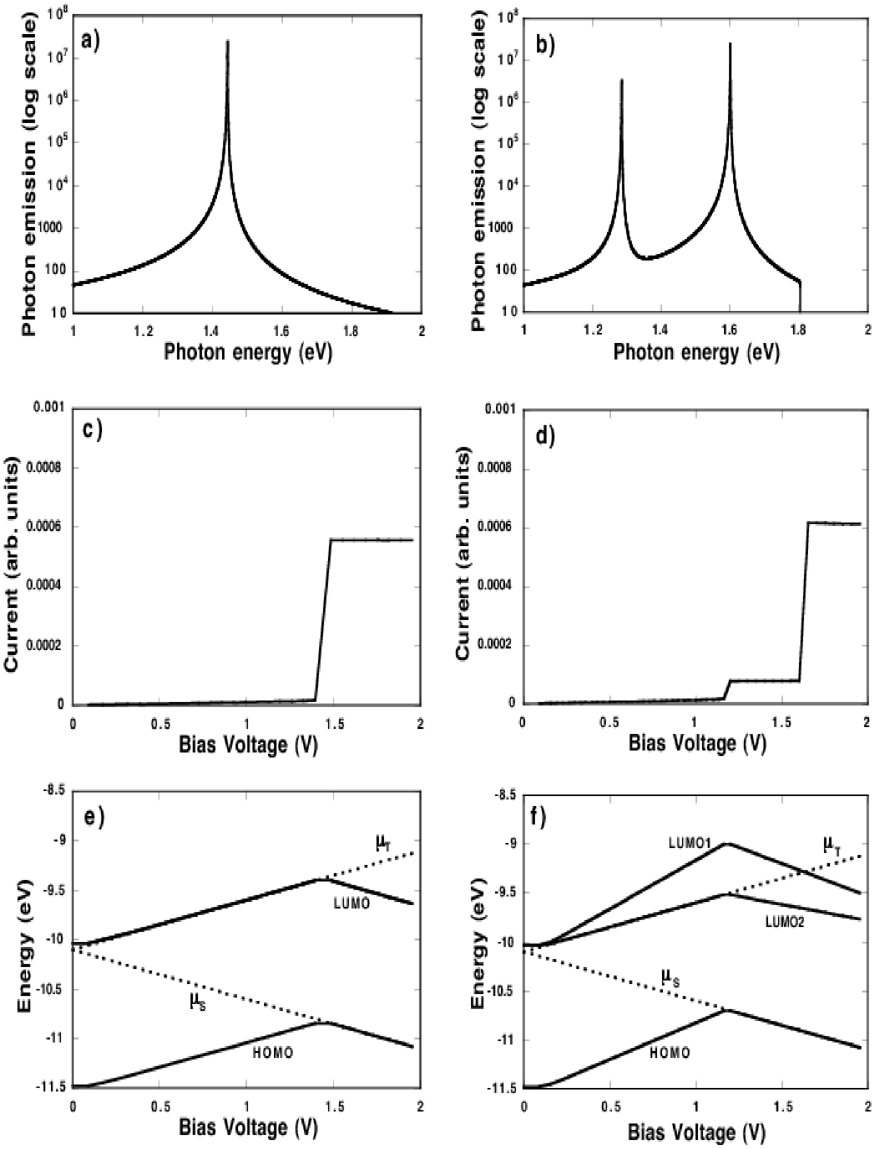

Figure 6.9: Weak fourfold-symmetric molecule-substrate coupling: photon emission, electric current, and molecular orbital energies as functions of bias voltage. (a) Approach A, photon emission vs. V_{bias}. (b) Approach B, photon emission vs. V_{bias}. (c) Approach A, I vs. V_{bias}. (d) Approach B, I vs. V_{bias}. (e) Approach A, molecular orbital energies. (f) Approach B, molecular orbital energies.

Sec. 6.5.2 and Sec. 6.5.3, the degree of partial population of the LUMO, and partial depopulation of the HOMO, is much greater. This results in much greater quantum efficiency for photon emission. Unlike in Sec. 6.5.3, the initial onset voltage for photon emission due to HOMO-LUMO transitions matches the HOMO-LUMO emission peak energy.

Approach B

As with Approach A, with Approach B very strong photon emission is predicted to occur. Fig. 6.9b shows the emission spectrum at high bias ($V_{bias} = 1.80$ V). Here, there are *two* peaks in the spectrum, corresponding to HOMO-LUMO1 and HOMO-LUMO2 transitions. Fig. 6.9d shows the I-V curve for this case. There are two high-bias dI/dV peaks (at 1.2 V and 1.6 V) and no low-bias peak.

These results can be understood by studying the behaviour of the molecular orbitals with applied bias voltage (see Fig. 6.9f). At low bias, the Fermi energy window approaches the LUMO1 and LUMO2. Unlike the other cases (Sec.6.5.2 and Sec. 6.5.3), in this case the LUMO2 coupling to tip and substrate is not strongly asymmetric, and electron states from the tip have a significant effect on the charge of the orbital; therefore, the LUMO2 electrostatically shifts in energy with μ_T so that the zero-bias charge on the molecule is maintained. Since no orbitals enter the Fermi energy window at low bias, there is no low-bias dI/dV peak. At 1.2 V, the HOMO energy reaches μ_S, and the HOMO begins to depopulate. This causes an electrostatic shift in orbital energy downwards, and the LUMO2 enters the Fermi energy window, creating a dI/dV peak at 1.2 V. At 1.6 V, the LUMO1 enters the Fermi energy window, resulting in another dI/dV peak. (This increase in current is greater than the increase at 1.2 V, because the LUMO1 has stronger electronic coupling than the LUMO2 to the tip probe.) The HOMO depopulates significantly further, with the LUMO1 populating by an equal amount. (The resulting electrostatic deviation in orbital energies is too small to be visible in Fig. 6.9f because the occupation of the HOMO is very sensitive to any deviation in energy away from μ_S.)

As with Approach A, the result is higher quantum efficiency for photon emission. Unlike in Sec.6.5.3(Approach B), the initial onset voltage for photon emission due to HOMO-LUMO2 transitions corresponds to the HOMO-LUMO2 emission peak energy. The HOMO-LUMO2 emission peak increases further once the onset voltage corresponding to the HOMO-LUMO1 emission peak is reached (due to the further depopulation of the

HOMO).

A signature of this relatively efficient photon emission regime, found with both Approach A and Approach B, is the *lack* of a low-bias dI/dV peak. This regime has yet to be realized in STM experiments; however, it is predicted that greatly enhanced quantum efficiency could be achieved by further weakening the coupling of the molecule to the metallic substrate, or by bringing the STM tip closer to the molecule. While in the model presented here, both the molecule-substrate distance is increased and the tip-molecule distance is decreased, it may be more experimentally feasible to increase the thickness of the oxide layer without bringing the tip closer to the molecule. This would cause a reduced current through the molecule. For such an experimental situation, the relevant luminescence observation is not the absolute photon emission intensity, but the quantum efficiency, or *photon yield* (the number of photons given off per electron passing through the molecule). This is predicted to be greatly enhanced.

6.5.5 Discussion of Results

Both Approach A and Approach B yield results consistent with experiment. For the case where the molecule is strongly coupled to the substrate, very weak photon emission, along with only a single high-bias dI/dV peak, is found with both approaches. Experimentally, all molecules that did not luminesce had a single high-bias dI/dV peak signature and no low bias dI/dV peak.

For the case where only a localized region of the molecule is strongly coupled to the substrate, both approaches yield much stronger photon emission than the first case. This is because, for a HOMO-LUMO transition, the relevant coupling asymmetry (between the tip-LUMO and the HOMO-substrate) is greatly reduced. Two emission peaks were found, the lower-energy peak being significantly lower in energy eV at onset than the energy corresponding to the onset voltage V. As well, in this case both a low-bias and high-bias dI/dV peak are found. This is consistent with experiment: In the experimental case where both low-bias and high-bias dI/dV peaks are observed, photon emission is also observed. Furthermore, there is additional evidence based on modelling of the molecular STM images[58] (presented in Sec. 4.6) that this experimental case corresponds to a localized region of strong coupling of the molecule to the substrate.

One qualitative feature observed experimentally and found theoretically with Approach A is not found with Approach B: Experimentally, there is a shift in the position of the high-bias dI/dV peak, depending on whether or not photon emission is observed. This shift is predicted with Approach A but not with Approach B.

There is additional experimental evidence in support of Approach A in the form of an observed zero-bias splitting in the LUMO degeneracy of a similar molecule (magnesium porphine) above the same Al_2O_3/NiAl(110) substrate.[77] It should be noted that for this experiment, only MgP molecules with two-lobe STM images were chosen for detailed study, so the *substrate-dependence* of the zero-bias splitting is unknown.

There is, however, a possible physical justification for Approach B. When a bias voltage is applied, the STM tip will electrostatically affect different molecular orbitals differently. The extent of these different effects is unknown. A simple electrostatic calculation, treating the tip/substrate as a point charge and a mirror image charge, suggests small differences (typically on the order of 100ths of an eV) in the average potential energy for the LUMO1 and LUMO2 orbitals. Thus, while the assumptions for Approach B may indeed be qualitatively correct, the degree to which the orbital energies of the LUMO1 and LUMO2 behave differently with bias is unknown and may be small.

For the case of very weak molecule-substrate coupling, much higher quantum efficiencies for photon emission are predicted to occur. This regime has not yet been realized experimentally, and would be an intriguing avenue for further research.

6.6 Conclusions

The local-electrode framework presented in the last two chapters coherently explains a multitude of experimental observations[11] not previously theoretically studied,[69] for the STM/Zn-etioporphyrin/Al_2O_3/NiAl(110) system. The following is a summary of these observations, with explanations based on model results:

(i) The observed molecular-based photon emission is due to transitions between the molecular LUMO, whose degeneracy has been split by molecule-substrate and/or molecule-STM tip interactions, and the molecular HOMO.

(ii) For some cases, low-bias dI/dV peaks are observed experimentally (see Fig. 6.5A,B). The model explains these as being due to a splitting of the LUMO degeneracy, with the lower-energy LUMO entering the Fermi energy window at low bias (see Sec. 6.5.3).

(iii) For some cases, no low-bias dI/dV peak is experimentally observed (see Fig. 6.5C-F). It is found that this occurs because the molecule is too strongly coupled to the substrate, with the LUMO either not entering the Fermi energy window at low bias (Approach A, see Sec. 6.5.2(Approach A)), or a splitting of the LUMO degeneracy and one of the LUMOs entering the window but contributing negligibly to the current due to very weak coupling of this LUMO to the tip (Approach B, see Sec. 6.5.2(Approach B)).

(iv) For cases with no low-bias peak, no photon emission is experimentally observed. This is explained by the model as being due to strongly asymmetric tip/molecule and molecule/substrate couplings. In these cases, when a bias is applied, the HOMO stays almost fully occupied and the LUMO almost completely unoccupied (see Sec. 6.5.2(Approach A,B)).

(v) There is an experimentally observed difference in the position of the high-bias dI/dV peak, between cases where photon emission is and is not observed (see Fig. 6.5). This is explained with Approach A by a breaking of the LUMO degeneracy only in the luminescent case (see Sec. 6.5.2(Approach A) and Sec. 6.5.3(Approach A)).

(vi) The experimental peak photon energy is about 0.5 eV below eV_{bias} at emission onset (see Fig. 6.8). This is explained by the model as being due to splitting of the LUMO degeneracy, with the lower-energy LUMO being well inside the Fermi energy window as the energy of the HOMO approaches the window. See Sec. 6.5.3(Approach A,B).

(vii) The high-energy photon emission spectra tails are steeper than the low-energy tails (see Fig 6.8). This is explained as being due to the substrate Fermi energy providing a sharp energy cutoff below which there are no available states to receive a transition (see Sec. 6.5.3(Approach A,B)).

(viii) There are significant differences in experimentally observed positions of dI/dV peaks (see Fig 6.5) depending on the position of the molecule on the substrate. These differences are consistent with differing local zero-bias Fermi levels, due to local variations in the work function of the oxide-coated metal substrate (see Sec. 6.5.3(Dependence on the zero-bias Fermi level)).

The model predicts that an additional photon emission peak should occur at a higher photon energy (close to the bias voltage at emission onset) than has been studied to date experimentally, for the case of molecular-based photon emission presented in Sec. 6.5.3. Experiments testing this prediction would be of interest.

It is also predicted that greatly enhanced quantum efficiency of photon emission could be achieved by further weakening the coupling of the molecule to the metallic substrate, or if possible by bringing the STM tip closer to the molecule (see Sec. 6.5.4).

Studying the STM/Zn-etioporphyrin/Al_2O_3/NiAl(110) system using the local-electrode theoretical framework presented in the last two chapters has yielded a coherent explanation of a large body of experimental results for this system. Using this framework, a much greater understanding may be gained of single molecule electroluminescence. This is an important step towards the development of the emerging field of single-molecule photonics. I hope that this work inspires further experimental and theoretical research in this promising new field.

While the present theory relies heavily on phenomenology, it has allowed the construction of energy level diagrams of the evolution of the molecular HOMO and LUMO orbitals and of the electrochemical potentials of the electrodes as a function of applied bias that are physically reasonable and are consistent with *both* the experimentally observed current-voltage characteristics *and* the experimental electroluminescence data. Thus the implementation of this model on an experimental system can also be viewed as a quantitative interpretation of the experimental data that is unique in that it satisfies more demanding experimental constraints than previous attempts to model experimental molecular electronic data that have focussed on experimental current-voltage characteristics alone. Therefore, as well as contributing to a better understanding of single-molecule photonics the present work provides much needed benchmarks for the development of accurate first principles theories of the evolution of the electronic structure of molecular nanowires under bias that do not yet exist at this time.

Chapter 7

Summary and Outlook

This thesis has helped to ‘shine a light’ on molecular electronics and photonics, by investigating theoretically the electroluminescence and scanning tunneling microscopy of single molecules in a unique way: not only through theorizing on the physics of the experimental phenomena, but, as an essential part of the investigation, by examining the nature of the experimental system itself. Among the important theoretical contributions of this thesis are the development of a local electrode framework to describe electron behavior in certain STM-molecule-substrate systems, an illustrative example of how this framework may be utilized to better understand the underlying experimental systems, and ultimately the achievement of a coherent unified explanation of a large body of electroluminescence and conductance data in an experimental system of current interest.

The work in this thesis was carried out very much with an eye not on precisely modelling an *a priori* known system, but rather from a starting point where most things were unknown. The first step to understanding the phenomenon of molecular electroluminescence in a system with many unknowns was to understand the general phenomenon using as simple a model as could be conceived that retained the important physics. This model formed the basis of my Master’s thesis and was outlined in Chapter 2. From this beginning came a somewhat more sophisticated two-electrode approach to the scanning tunneling microscopy of single molecules. This approach was found to successfully account for various different STM images observed for the Zn-etioporphyrin molecule, and as well provided evidence for the likely nature of the molecule-substrate coupling for the system. From this point, the model was enhanced again, into a local electrode approach with which both single molecule electrical conductance and electroluminescence could be studied in a coherent framework. Finally, this model was applied to the same experimental system of STM/Zn-etioporphyrin/Al_2O_3/NiAl(110), and a wealth of previously unexplained observations were explained using the framework of local electrodes.

The various models presented in this thesis were all relatively simple out of necessity (due to a lack of knowledge of the precise geometry of the system), consisting of tight binding chains of atomic orbitals for electrodes and a molecular orbital framework that uses extended Hückel theory. The result is a real advance in our understanding of the specific Zn-etioporphyrin experimental system, as well as a greater physical intuition for the behaviour of single molecule systems in general. Theoretical techniques with a high degree of sophistication are often automatically assumed to be superior, and capable of greater physical insight. It is a hope of mine that this thesis has demonstrated that sometimes the opposite may be true.

Variants of the local electrode approach outlined in this thesis will likely be used in future theoretical models, not only for experimental systems with irregular ‘spacer’ layers as are analyzed here, but as well for systems intentionally designed with the idea of ‘local electrodes’ in mind. As experimental techniques continue to advance, single molecule systems with a known composition of local electrodes will become increasingly accessible to experimentation. Advances in nanoelectronic and nanophotonic devices may take the form of single molecule switches, transistors, other electronic and photonic circuitry, and circuitry utilizing the interplay of electrons and photons. Building on the work of this thesis, and comparisons to further experimental advances, theoretical models of local electrodes will become much more sophisticated. By including both electrons and photons in a coherent theoretical framework, the fields of single molecule electronics and photonics are set for many intriguing discoveries.

Molecular electronics is a field with a lot of potential for new technologies, and the emergence of photonics adds a whole new dimension for applications and understanding. However, some of the biggest technological jumps are occurring in nanoscopic systems where we still do not really understand the details of what is going on, with one prominent example today being the field of nanoscale biotechnology. Technology can progress, to a certain point, beyond physical understanding using ‘trial and error’ techniques in achieving desired effects. The past has shown us, however, that when technology surpasses understanding there may be unintended consequences.

With this thesis, we begin to understand the basics of single molecule electroluminescence. Moving forward from this point, we will hopefully see further vigorous experimentation inspired by this work, involving molecular electroluminescence on both systems with more well-understood molecule-surface interactions, and systems that may not be well-understood but are within theoretical reach. On the theoretical side, there is near limitless room for improved techniques, as well as the development of new approaches to studying electrons and photons together in a nanoscale system.

Regardless of potential applications and technological advancement, I hope that this thesis moves us in the direction of increasing our basic understanding of the nanoscale world.

Chapter 8

Appendices

8.1 Appendix A

As discussed in Sec. 4.2, the geometrical structure of Zn(II)-etioporphyrin I was obtained[59] by relaxing an approximate structure of the molecule into the geometry that has the lowest total energy. Table 8.1 shows the 'relaxed' geometry of the molecule, in Cartesian coordinates.

Element	X	Y	Z
Zn	0.000000	0.000000	0.000000
N	2.061348	0.000000	-0.003388
C	1.115364	2.884249	0.000701
C	2.889468	1.111123	-0.002251
C	0.697170	4.284513	0.002650
C	4.289785	0.685821	-0.000279
C	2.443502	2.439207	0.002554
C	1.632512	5.458822	0.002632
C	5.478538	1.607806	-0.038673
C	5.854234	2.050617	-1.472201
H	3.209543	3.209476	0.010088
H	2.250299	5.482045	-0.905397
H	2.316148	5.429495	0.861513
H	1.084235	6.405051	0.049687
H	6.344926	1.113025	0.418987
H	5.283275	2.498735	0.573334
H	5.017506	2.567211	-1.956715
H	6.715931	2.730174	-1.458090
H	6.111513	1.183341	-2.091606

Table 8.1: Geometrical structure of Zn(II)-etioporphyrin I obtained by an energy minimization scheme based on density functional theory[59]. The molecule has fourfold-symmetry. This table shows atomic coordinates (in Angstroms) for one of the four quadrants of the molecule. The other quadrants are obtained by rotation of the coordinates by 90, 180, and 270 degrees about the Z axis.

8.2 Appendix B

The electronic structure of the HOMO (highest occupied molecular orbital) and the two degenerate LUMOs (lowest unoccupied molecular orbitals) is shown in Fig. 8.1, Fig. 8.2 and Fig. 8.3.[78] LUMO1 refers to the lowest unoccupied molecular orbital having stronger electrostatic coupling to the STM tip in Chapter 6, and LUMO2 refers to the orbital with weaker electrostatic coupling to the tip. In each figure, the molecule is in the same orientation as in Fig. 4.1.

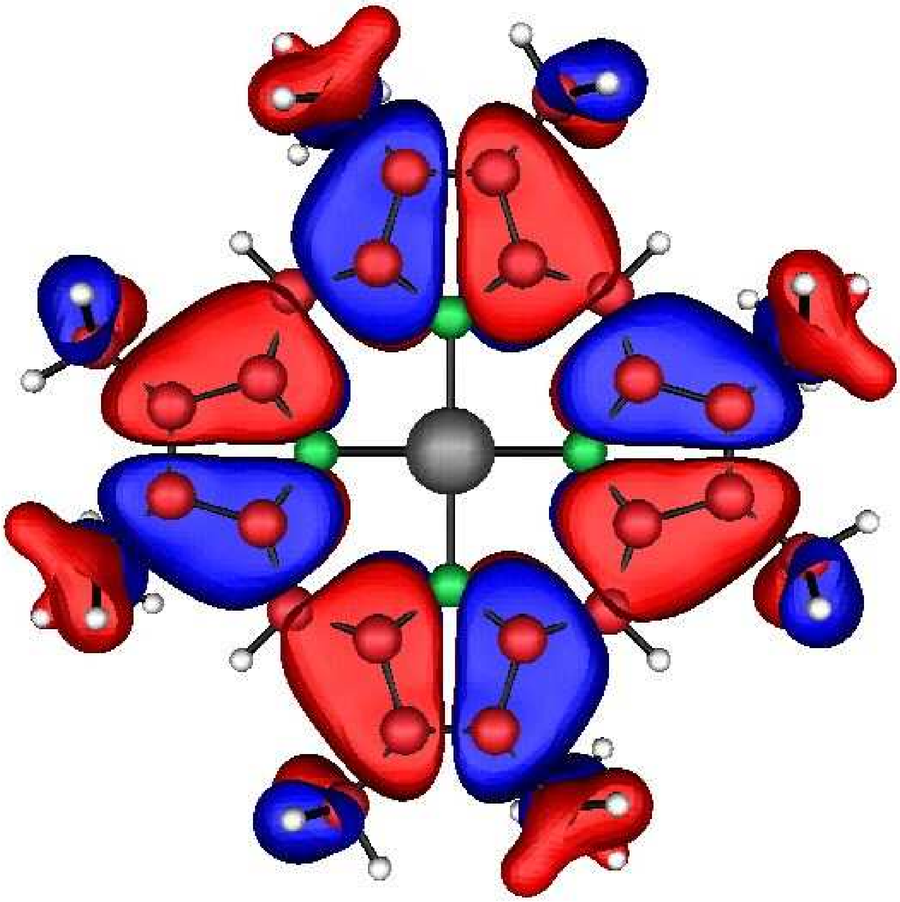

Figure 8.1: A 3-dimensional representation of the electronic structure of the HOMO of Zn-etioporphyrin. Red regions indicate positive amplitudes, blue regions indicate negative amplitudes. C, H, N and Zn atoms are coloured red, white, green and grey, respectively.

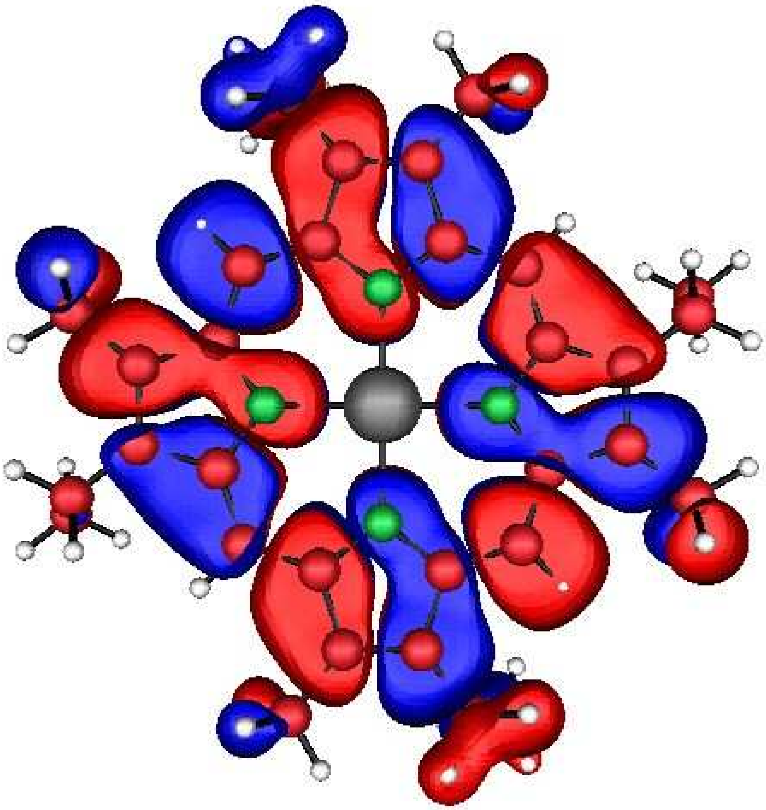

Figure 8.2: A 3-dimensional representation of the electronic structure of the LUMO1 of Zn-etioporphyrin. Red regions indicate positive amplitudes, blue regions indicate negative amplitudes. C, H, N and Zn atoms are coloured red, white, green and grey, respectively.

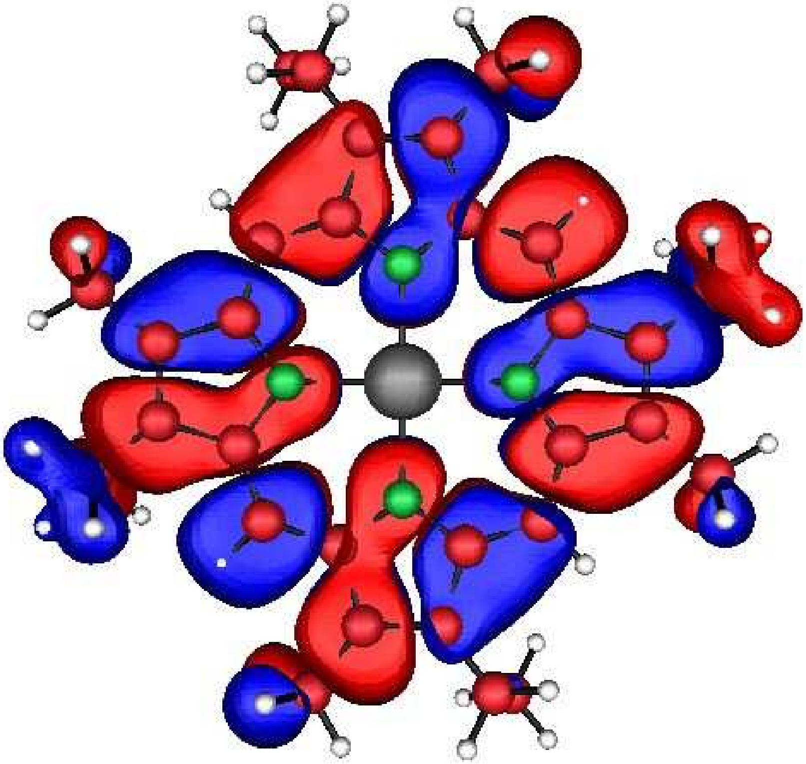

Figure 8.3: A 3-dimensional representation of the electronic structure of the LUMO2 of Zn-etioporphyrin. Red regions indicate positive amplitudes, blue regions indicate negative amplitudes. C, H, N and Zn atoms are coloured red, white, green and grey, respectively.

Bibliography

[1] I. I. Smolyaninov and M. S. Khaikin, Phys. Lett. A **149**, 410 (1990).

[2] R. Berndt, R. Gaisch, J. Gimzewski, B. Reihl, R. Schlittler, W. Schneider, and M. Tschudy, Science **262**, 1425 (1993).

[3] E. Flaxer, O. Sneh, and O. Cheshnovsky, Science **262**, 2012 (1993).

[4] G. E. Poirier, Phys. Rev. Lett. **86**, 83 (2001).

[5] F. Touhari, E. J. A. Stoffels, J. W. Gerristsen, H. V. Kempen, and P. Callant, Appl. Phys. Lett **79**, 527 (2001).

[6] K. Sakamoto, K. Meguro, R. Arafune, M. Satoh, Y. Uehara, and S. Ushioda, Surf. Sci. **502-503**, 149 (2002).

[7] J. H. Coombs, J. K. Gimzewski, B. Reihl, J. K. Sass, R. R. Schlittler, Jour. Microscopy **152**, 325 (1988).

[8] R. Berndt, J. K. Gimzewski, and P. Johansson, Phys. Rev. Lett. **67**, 3796 (1991).

[9] W. L. Barnes, J. Mod. Opt. **45**, 661 (1998).

[10] G. Hoffmann, L. Libioulle, and R. Berndt, Phys. Rev. B **65**, 212107 (2002), and references therein.

[11] X. H. Qiu, G. V. Nazin, and W. Ho, Science **299**, 542 (2003).

[12] Z.-C. Dong, X.-L. Guo, A. S. Trifonov, P. S. Dorozhkin, K. Miki, K. Kimura, S. Yokoyama, and S. Mashiko, Phys. Rev. Lett. **92**, 86801 (2004).

[13] J. Buker and G. Kirczenow, Phys. Rev. B **66**, 245306 (2002).

[14] D. L. Abraham, A. Veider, C. Schönenberger, H. P. Meier, D. J. Arent, and S. F. Alvarado, Appl. Phys. Lett. **56**, 1564 (1990).

[15] A. Downes and M. E. Welland, Phys. Rev. Lett. **81**, 1857 (1998).

[16] P. Johansson, R. Monreal, and P. Apell, Phys. Rev. B **42**, 9210 (1990).

[17] R. Berndt and J. K. Gimzewski, *Photon Emission from C60 in a Nanoscopic Cavity*, Proceedings of the NATO Advanced Research Workshop: "Scanning Probe Microscopies and Molecular Materials" 1994.

[18] R. Landauer, IBM J. Res. Dev. **1**, 223 (1957), R. Landauer, Phys. Lett. **85A**, 91 (1981).

[19] S. Datta, *Quantum Transport: Atom to Transistor* (Cambridge University Press, New York, 2005).

[20] L. E. Ballentine, *Quantum Mechanics: A Modern Development* (World Scientific, Singapore, 1998), Chap. 19.

[21] E. Emberly and G. Kirczenow, Phys. Rev. B **64**, 125318 (2001).

[22] P. Damle, A. W. Ghosh, and S. Datta, Jour. Chem. Phys **281**, 171 (2002).

[23] J. Buker, *Photon Emission From Molecular Wires.* Master's Thesis, Simon Fraser University (2003).

[24] J. Bardeen, Phys. Rev. Lett. **6**, 57 (1961).

[25] J. Tersoff and D. R. Hamann, Phys. Rev. Lett. **50**, 1998 (1983).

[26] P. Sautet and C. Joachim, Phys. Rev. B **38**, 12238 (1988).

[27] G. Doyen, E. Koetter, J. P. Vigneron and M. Scheffler, Appl. Phys. A **51**, 281 (1990).

[28] W. Sacks and C. Noguera, Phys. Rev. B **43**, 11612 (1991).

[29] M. Tsukada, K. Kobayashi, N. Isshiki and H. Kageshima, Surf. Sci. Rep. **13**, 265 (1991).

[30] J. P. Vigneron, I. Derycke, P. Lambin, T. Laloyaux, A. A. Lucas, L. Libioulle and A. Ronda, Ultramicroscopy, **42**, 250 (1992).

[31] V. M. Kenkre, F. Biscarini and C. Bustamante, Phys. Rev. B **51**, 11074 (1995).

[32] A. J. Fisher and P. E. Blöchl, Phys. Rev. Lett. **70**, 3263 (1993).

[33] F. Biscarini, C. Bustamante and V. M. Kenkre, Phys. Rev. B **51**, 11089 (1995).

[34] P. Sautet and M. L. Bocquet, Phys. Rev. B **53**, 4910 (1996).

[35] P. Sautet, Chem. Rev. **97** 1097 (1997).

[36] M. Schunack, F. Rosei, Y. Naitoh, P. Jiang, A. Gourdon, E. Laegsgaard, I. Stensgaard, C. Joachim and F. Besenbacher, J. Chem. Phys. **117**, 6259 (2002).

[37] J. Repp, G. Meyer, S. M. Stojkovic, A. Gourdon and C. Joachim, Phys. Rev. Lett **94**, 26803 (2005).

[38] STM images of thin (5 Å) pristine alumina films on NiAl(111) surfaces exhibit regular arrays of bright spots[39] that signal locations where the film is the most conductive. The most conductive locations are spaced 15-45 Å apart depending on the bias voltage applied between the STM tip and substrate.[39] Thin alumina films on NiAl(110) surfaces have similar small, relatively conductive regions[40] Thus, it is reasonable to suppose that for such systems the alumina film behaves as a *nonuniform* tunnel barrier between a molecule on its surface and a metal substrate beneath it, and that electrons are transmitted between the molecule and substrate primarily at the more conductive spots of the alumina film.

[39] T. Maroutian, S. Degen, C. Becker, K. Wandelt, and R. Berndt, Phys. Rev. B **68**, 155414 (2003).

[40] G. Kresse, M. Schmid, E. Napetschnig, M. Shishkin, L. Köhler and P. Varga, Science **308**, 1440 (2005).

[41] L. E. Ballentine, *Quantum Mechanics: A Modern Development* (World Scientific, Singapore, 1998), Chap. 16.

[42] E. Emberly and G. Kirczenow, Phys Rev. Lett. **81**, 5205 (1998); J. Phys.: Condens. Matter **11**, 6911 (1999).

[43] M. Wolfsberg and L. J. Helmholz, Jour. Chem. Phys **20**, 837 (1952).

[44] The implementation used was that of G. A. Landrum and W. V. Glassy, YAeHMOP project, http://yaehmop.sourceforge.net

[45] G. Kirczenow, "Molecular Nanowires and their Properties as Electrical Conductors" Chapter 4 (pp.77-130) in "The Oxford Handbook of Nanoscience and Technology: Volume I," edited by A. V. Narlikar and Y. Y. Fu, Oxford University Press, U.K. (2009), in press.

[46] P. Delaney and J. C. Greer, Phys. Rev. Lett. **93**, 036805 (2004).

[47] N. Sai, M. Zwolak, G. Vignale and M. Di Ventra, Phys. Rev. Lett. **94**, 186810 (2005).

[48] C. Toher, A. Filippetti, S. Sanvito and K. Burke, Phys. Rev. Lett. **95**, 146402 (2005).

[49] P. Darancet, A. Ferretti, D. Mayou and V. Olevano, Phys. Rev. B **75**, 075102 (2007).

[50] F. Evers and K. Burke, *Nanoand Molecular Electronics Handbook* p. 24-1 (Ed. S. E. Lyshevski) Taylor & Francis, Boca Raton, (2007).

[51] S. H. Ke, H. U. Baranger and W. T. Yang, J. Chem. Phys. **126**, 201102 (2007).

[52] C. D. Pemmaraju, T. Archer, D. Sanchez-Portal and S. Sanvito, Phys. Rev. B **75**, 045101 (2007).

[53] E. Prodan and R. Car, Phys. Rev. B **76**, 115102 (2007).

[54] S. Y. Quek, J. B. Neaton, M. S. Hybertsen, E. Kaxiras and S. G. Louie, Phys. Rev. Lett. **98** 066807 (2007).

[55] M. Koentopp, C. Chang, K. Burke, and R. Car, J. Phys.: Condens. Matter **20**, 083203 (2008).

[56] K. S. Thygesen and A. Rubio, J. Chem. Phys. **126**, 091101 (2007); Phys. Rev. B **77**, 115333 (2008).

[57] S. I. Grossman, *Linear Algebra*, chap. 5, Saunders College Publishing, 4th edn. (1991).

[58] J. Buker and G. Kirczenow, Phys. Rev. B **72**, 205338 (2005).

[59] The B3PW91 functional and Lanl2DZ basis set were used for this calculation. M. J. Frisch *et al.*, GAUSSIAN 98, Gaussian, Inc., Pittsburgh, PA, (1998).

[60] S. Datta, W. Tian, S. Hong, R. Reifenberger, J. I. Henderson, and C. P. Kubiak, Phys. Rev. Lett. **79**, 2530 (1997).

[61] E. G. Emberly and G. Kirczenow, Phys. Rev. B **64**, 235412 (2001).

[62] J. G. Kushmerick, D. B. Holt, J. C. Yang, J. Naciri, M. H. Moore, and R. Shashidhar, Phys. Rev. Lett. **89**, 086802 (2002).

[63] D. M. Cardamone and G. Kirczenow, Phys. Rev. B **77**, 165403 (2008).

[64] E. G. Emberly and G. Kirczenow, Phys. Rev. B **58**, 10911 (1998).

[65] M. Di Ventra, S. T. Pantelides, and N. D. Lang, Phys. Rev. Lett. **84**, 979 (2000).

[66] P. S. Damle, A. W. Ghosh, and S. Datta, Phys. Rev. B **64**, 201403(R) (2001).

[67] X. H. Qiu, G. V. Nazin, and W. Ho, Phys. Rev. Lett. **93**, 196806 (2004).

[68] Here it is assumed for simplicity that processes injecting electrons into different ethyl groups are mutually incoherent.

[69] J. Buker and G. Kirczenow, Phys. Rev. B. **78**, 125107 (2008).

[70] For numerical convenience in the calculations necessary for this level of modelling, the site energies ε and hopping amplitudes β in Eq. 5.1 are chosen to be the same for all of the ideal one-dimensional tight-binding electrodes, and to be independent of the applied bias voltage. Hence in Eq. 5.11 $T = \sum_{i=1}^{m} \frac{v'}{v} |t_i|^2 = \sum_{i=1}^{m} |\psi_{1,i}|^2$ since the velocities of the incoming electron (v) and the (elastically scattered) transmitted electron (v') are equal. However, the transmission probability T will depend on the applied bias voltage V_{bias} due to the dependence of the molecular orbital energies on the bias that is calculated as described in Sec. 6.2.

[71] W. Song and M. Yoshitake, Applied Surface Science **251**, 14 (2005).

[72] The implementation used, for the Zn-etioporphyrin molecule, was that of G. Calzaferri, R. Rytz, and M. Brändle, ICON-EDiT, http://iacrs1.unibe.ch/program/iconedit.html

[73] In order to simulate strong molecule-substrate coupling on a uniform oxide surface, each substrate contact in this case is positioned 4.0 Å below the plane of the molecule (2.5Åfrom the nearest atom of the molecule). The tip probe is positioned 4.1 Å above the molecule. See Fig.6.3.

[74] Here, the substrate contact S_4 is positioned 4.0 Å below the plane of the molecule, with the other three substrate contacts positioned 4.5 Åbelow the plane. The tip probe is positioned 4.5 Å above the molecule.

[75] Since the LUMO2 is strongly coupled to the substrate (similar to Sec. 6.4.2: Strong fourfold-symmetric molecule-substrate coupling), it is assumed that the splitting of degeneracy primarily changes the LUMO1 energy: $\varepsilon_{LUMO1} = \varepsilon_{LUMO} + 0.5$ eV, $\varepsilon_{LUMO2} = \varepsilon_{LUMO}$.

[76] Here, the substrate contacts are positioned 4.5 Å below the plane of the molecule (3.0 Å from the nearest atom of the molecule) and the tip probe is positioned 4.0 Å above the molecule. The lateral electrode positions are the same as for the other cases (see Fig. 6.3).

[77] S. W. Wu, N. Ogawa, and W. Ho, Science **312**, 1362 (2006).

[78] B. M. Bode and M. S. Gordon. *MacMolPlt: a graphical user interface for GAMESS.* J. Mol. Graph. Model., 16(3):133–138, June 1998.